

A NEW STATIONARY DIGITAL BREAST TOMOSYNTHESIS SYSTEM:
IMPLEMENTATION AND CHARACTERIZATION

Jabari Calliste

A dissertation submitted to the faculty at the University of North Carolina at Chapel Hill in
partial fulfillment of the requirements for the degree of Doctor of Philosophy in the
Department of Applied Physical Sciences.

Chapel Hill
2016

Approved by:

Cherie Kuzmiak

David Lalush

Yueh Z. Lee

Jianping Lu

Otto Zhou

© 2016
Jabari Calliste
ALL RIGHTS RESERVED

ABSTRACT

Jabari Calliste: A new generation stationary digital breast tomosynthesis system: Implementation and characterization
(Under the direction of Otto Zhou)

Digital breast tomosynthesis systems (DBT) utilize a single thermionic x-ray source that moves around the breast in a fixed angular span. As a result, all current DBT system requires the mechanical motion of the x-ray source during the scan, limiting image quality either due to the focal spot blurring or a long scan time. This causes an unfavorable reduction in the in-plane resolution compared to 2D mammography.

Our research group developed and demonstrated a first generation stationary digital breast tomosynthesis (s-DBT) system that uses a linear carbon nanotube (CNT) x-ray source array. Since the stationary sources are not subject to focal spot blurring, and images can be acquired rapidly, the in-plane system resolution is improved. Additionally, image acquisition time is independent of angular span since there is no motion, allowing for large angular spans, and increased depth resolution. The improved resolution of the first generation s-DBT system over continuous motion (CM) DBT has been demonstrated with image evaluation phantoms and a human specimen study. The first generation s-DBT is currently undergoing clinical trials at the University of North Carolina Cancer Hospital.

Limitations associated with the first generation system, such as limited tube flux, and limited x-ray energy, placed limitations on our clinical trials and future clinical implementation. Also, the limited angular span could be improved for increased depth resolution, as there is no

cost on patient imaging time. The goal of this thesis work was to design construct and characterize a second generation s-DBT system, capable of faster image acquisition times, and higher depth resolution than our first generation system.

The second generation s-DBT system was built using a newly designed distributed CNT x-ray source array. The system was then characterized and compared to the first generation system and two commercially available DBT systems. Using physical measurements that are used in medical imaging, the system showed significant improvement in resolution over the first generation system and both commercially available systems, coupled with equal or faster image acquisition times. A separate study investigating the feasibility of contrast enhanced (CE) imaging was conducted, where the system showed capability in both temporal subtraction (TS) and dual energy (DE) imaging.

ACKNOWLEDGEMENTS

I would like to thank both my advisors, Dr. Otto Zhou and Dr. Jianping Lu, for their leadership, guidance and encouragement throughout my graduate studies. Being able to work with them on research that translates to useful applications today has truly motivated me. It was an absolute pleasure working with you. I also highly appreciate the rest of the members in my committee, Dr. Cherie Kuzmiak, Dr. David Lalush, and Dr. Yueh Z. Lee for their direction, and supervision. Dr. Lee, thanks you for your assistance and guidance on the medical side of my research, learning the clinical side of research was a great and beneficial experience. Thank you to the members of my department, namely Dr. Sean Washburn for his advice throughout my time at UNC. I would also like to thank each member of our research group, both past and present, which has helped me through my studies, including: Laurel Burk, Pavel Chtcheprov, Emily Gidcumb, Allison Hartman, Christy Inscoe, Marci Potuzko, Jing Shang, Andrew Tucker, Xin Qian, Gongting Wu, and Lei Zhang.

A special thank you to the industrial collaborators who I worked with during my graduate studies, Hologic Inc., and XinRay Systems Inc, for the cooperation and technical assistance. Dr. Bo Gao, your time and patience when working with me was highly valued, thank you. Special thanks also to the employees of the mammography department at UNC Hospitals, specifically Dr. Kuzmiak, I would not have been able to successfully complete my studies without your help. I am extremely grateful for the opportunity to work alongside you, someone who is highly revered in the mammography field.

Finally, I would like to thank all my friends and family for their continued support throughout this process. To my mother and father, I am unconditionally grateful for all of your love and support you have given me, it's because of you I continued to strive for higher education. To my wife, thank you for being at my side throughout my many years of school, I would not have been able to accomplish this without you.

TABLE OF CONTENTS

LIST OF TABLES.....	xiii
LIST OF FIGURES.....	xv
LIST OF ABBREVIATIONS.....	xxii
CHAPTER 1: Introduction.....	1
1.1 Dissertation Overview.....	1
1.2 Specific Research Aims	2
1.2.1 Development and characterization of the 2G s-DBT system.....	2
1.2.2 Feasibility of CE s-DBT.....	2
CHAPTER 2: Physics of X-ray imaging.....	3
2.1 Discovery of X-rays	3
2.2 Generation of X-rays.....	3
2.2.1 Bremsstrahlung X-rays.....	4
2.2.2 Characteristic X-rays.....	6
2.3 X-ray Interactions in matter	8
2.3.1 Photoelectric Absorption.....	8
2.3.2 Rayleigh Scattering	10
2.3.3 Compton Scattering.....	10

2.3.4	Pair Production	11
2.4	X-ray Attenuation Tissue	11
2.5	Conventional X-ray Tubes	13
2.5.1	Cathode Assembly.....	14
2.5.2	Anode	14
2.5.3	Tube Housing	15
2.5.4	Focal Spot.....	15
2.5.5	Window and Filter.....	16
2.5.6	Heel Effect.....	17
2.6	References	18
CHAPTER 3:	Fundamentals of Mammographic Imaging	19
3.1	Breast Cancer Screening	19
3.2	X-ray Mammography	20
3.2.1	Breast Anatomy and mammographic features of breast cancer	20
3.3	X-ray Mammographic Imaging.....	23
3.3.1	Influences on imaging quality	24
3.3.2	Mammographic equipment	30
3.4	Mammographic modalities.....	32
3.4.1	Screen Film Mammography.....	32
3.4.2	Full Field Digital Mammography	34

3.4.3	Contrast Enhanced Full Field Digital mammography.....	36
3.5	Imaging quality and performance	38
3.6	Digital Tomosynthesis.....	40
3.7	References	43
CHAPTER 4:	Carbon Nanotube X-ray Sources	45
4.1	Carbon Nanotubes	45
4.1.1	Structure of CNTs	45
4.2	Carbon nanotube field emission.....	48
4.2.1	Field Emission Theory	48
4.2.2	CNT X-ray sources.....	49
4.3	CNT X-Ray source applications	51
4.3.1	MRT	52
4.3.2	Micro-CT.....	53
4.3.3	s-DCT	54
4.4	References	56
CHAPTER 5:	Stationary Digital Breast Tomosynthesis.....	58
5.1	Motivation for a stationary digital breast tomosynthesis system	58
5.1.1	Limitations of current DBT systems	58
5.1.2	Proposed solution and advantages of s-DBT	59
5.2	First generation stationary digital breast tomosynthesis system	60

5.2.1	CNT x-ray source array	60
5.2.2	System Description / Assembly and Integration	62
5.2.3	System performance and optimization	64
5.3	Specimen study	72
5.3.1	Evaluation of s-DBT vs 2D	73
5.3.2	CM-DBT	79
5.4	Clinical Trial	84
5.4.1	Purpose	84
5.4.2	Results	86
5.4.3	Discussion	89
5.5	References	91
CHAPTER 6:	A new generation s-DBT system	93
6.1	Motivation	93
6.2	Methods and Materials	96
6.2.1	Digital Breast Tomosynthesis systems	96
1.1.1	GE Senographe SenoClaire DBT system	98
6.3	X-ray output and beam quality	98
6.4	X-ray focal spot size measurement	100
6.5	Geometry Calibration	100
6.6	Image reconstruction	101

6.7	System modulation transfer function	101
6.7.1	Projection images MTF	102
6.7.2	Reconstructed in-focus plane MTF	102
6.8	Phantom imaging.....	102
6.9	Artifact spread function.....	103
6.10	Results	104
6.10.1	CNT x-ray source array characterization	104
6.10.2	Beam quality	106
6.10.3	System geometry calibration.....	107
6.10.4	Radiation dose and system scan time.....	110
6.10.5	System Resolution.....	112
6.10.6	In-plane system resolution	113
6.10.7	In-depth resolution as measured by artifact spread function.....	117
6.11	Discussion.....	119
6.11.1	X-ray tube characterization	119
6.11.2	DBT projection MTF and system MTF	120
6.11.3	Artifact spread function (ASF).....	122
6.12	Conclusion	123
6.13	References	124
CHAPTER 7:	Feasibility of Contrast Enhanced Imaging with s-DBT.....	128

7.1	Motivation for s-DBT Contrast Enhanced Imaging.....	128
7.2	Materials and Methods	130
7.2.1	Temporal Subtraction.....	130
7.2.2	Dual Energy Subtraction	132
7.2.3	Effective Mass Attenuation Coefficient & Effective Absorption Energy Calculations	132
7.2.4	Simulations for x-ray spectral optimization.....	135
7.2.5	Phantom Experiments	137
7.3	Results	140
7.3.1	Simulations.....	140
7.3.2	Phantom Experiments	150
7.3.3	Discussion and Conclusion	160
7.4	References	163
CHAPTER 8:	Summary and Future Direction.....	165

LIST OF TABLES

Table 3. 1 ACR BI-RADS Terms for Breast Density. Adapted from ACR BI-RADS Atlas 5 th Edition ^{8,9}	22
Table 3. 2 Description of the types of malignant masses according to ACR BR-RADS lexicon. Adapted from ACR BI-RADS Atlas 5 th Edition ^{8,9}	22
Table 3.3 . Description of the types of calcification clusters according to ACR BR-RADS lexicon Adapted from ACR BI-RADS Atlas 5 th Edition ^{8,9}	23
Table 3.4 The decision matrix used in the diagnosis of breast cancer.....	38
Table 5.1 The specifications of the first generation system.....	62
Table 5. 2 The calculated results for SdNR, FWHM of the ASF, and MTF. The data is separated into the five groups of confi- gurations. MMOC stands for more mAs on central proje- ctions. LMOC stands for less mAs on central projections. The 29 projection view, and 28° angular span, with an ev- en dose distribution resulted in the highest quality factor value for an exposure of 100 mAs. Reprinted with permi- ssion from Tucker et al., Med. Phys., 40, 031917-8, (2013). Copyright 2013, American Association of Physicists in Medicine.	66
Table 5.3 Sensitivity and specificity values by Reader and Modality. Reprinted from Tucker et al., Acad Radiol. 2014 Dec; 21(12):1547-52.	75
Table 5.4 Calculated values from the McNemar test showing the disagree- ment between imaging modalities for the four readers. Repri- nted from Tucker et al., Acad Radiol. 2014 Dec; 21(12):1547-52.	76
Table 5.5 Results of the two-sided t test on reader preference. Positive values represent a preference for s-DBT compared to 2D mammography. Reprinted from Tucker et al., Acad Radiol. 2014 Dec; 21(12):1547-52.	77
Table 5.6 The radiologist findings of 10 evaluated patients. Reprinted from Jabari Calliste et al. SPIE Med. Imaging Phys. Med. Imaging (2015), p. 941228	88
Table 6.1 x-y-z coordinates, and angular distribution of each focal spot in the linear CNT source array relative to the detector.	109
Table 6.2 Comparison of imaging times between the 1st and 2G s-DBT systems. The 2nd generation system is capable of measuring all compression thicknesses shown in about 4 seconds.	112
Table 6.3. Experimentally measured MTF for the 1st and 2G s-DBT syst- ems in the scanning direction. The 1st generation system is cu-	

rrently configured to operate inly in full resolution mode, ther- efore measurements at pixel size 140 μm were unavailable.....	115
Table 7. 1 Parameters used for sprectra simulation	136

LIST OF FIGURES

Figure 2.1 Illustration of four electron interactions that produce Bremsstrahlung radiation.....	5
Figure 2.2 An illustration of Bremsstrahlung radiation spectrum for an arbitrary peak tube voltage.....	6
Figure 2.3 An illustration of the mechanism of characteristic x-ray production.....	7
Figure 2.4 Illustration of photoelectric absorption interaction in matter.	9
Figure 2.5 Illustration of modern x-ray tube. Major components of the tube include the cathode, anode, and tube housing.....	13
Figure 2.6 An illustration of the effect of the incident focal spot size on the effective focal spot size.....	16
Figure 2.7 Illustration showing the effect of the anode angle on FOV, and the heel effect.....	17
Figure 3.1 Diagram of breast anatomy. The diagram shows the major and surrounding structures of the breast. Image adapted from original © Patrick J Lynch. Reprinted with permission from the copyrighter based on the Creative Commons Attribution from Wikipedia.com.....	21
Figure 3.2 (Left) Schematic diagram showing the effect of focal spot size on resolution. (Right) Schematic diagram illustrating x-ray magnification	25
Figure 3.3 Illustration showing unsharpness in x-ray profile due to the shape of the object.	26
Figure 3.4 Demonstration of the effect of the attenuation coefficient on the contrast of an image. For the same material, there is an increase in attenuation with increasing material thickness, and for higher attenuating objects (darker object).	28
Figure 3.5 Illustration of a mammography unit's key components and orientation. Cathode and anode axis is along the chest wall direction, positioned such that the thicker side of the breast is under the cathode to promote a more uniform x-ray distribution. The figure on the right shows the fall off of intensity due to the heel effect. Adapted from.....	31
Figure 3.6 Schematic diagram of a screen film detector.	34
Figure 3.7 Illustration of the two types of digital detectors, indirect and direct conversion.....	36
Figure 3.8 Example of an arbitrary ROC curve.....	40

Figure 3.9 Schematic diagram of showing the principle of digital breast tomosynthesis.....	41
Figure 4.1 Shows a graphene sheet with chiral vectors depicting the types of CNT structures produced.	46
Figure 4.2 A representation of the three types of SWNT produced from the “rolling” of graphene sheets.....	47
Figure 4.3 Diagram of the field emission effect. The effective barrier is lowered by the electric field so that electrons near the Fermi level can tunnel through the barrier ¹¹	49
Figure 4.4 Diagram of typical CNT source design. The source consist of a CNT cathode, gate mesh, focusing electrodes and an anode. A small voltage is applied across the gate mesh and the cathode, while a large voltage is applied to the anode.	50
Figure 4.5 (a) Image of the desktop MRT system. (b) A histological slice of a mouse brain showing paths of irradiation ^{18,20}	53
Figure 4.6 (a) Image showing the setup of the micro-CT system, the inset image shows the system covered and shielded. (b) A reconstructed slice of micro-CT mouse image gated to its respiration cycle, and (c) gated to cardiac cycle ²²	54
Figure 4.7 (a) Laboratory setup of the bench top s-DCT system. (b) Reconstructed slice of an anthropomorphic phantom images with the s-DCT system ²³	55
Figure 5.1 Effect of patient motion on visibility of microcalcifications. Attribution: © Andrew Smith ⁹	60
Figure 5.2 Photo of s-DBT tube with the key components labelled.	61
Figure 5.3. System geometry of the first generation stationary digital breast tomosynthesis system with the CNT x-ray source array.	63
Figure 5.4 ASF plots for 14° and 28° angular span with equal number of projections and entrance dose. Reprinted with permission from Tucker et al., Med. Phys., 40, 031917-8, (2013). Copyright 2013, American Association of Physicists in Medicine.	67
Figure 5.5 FWHM of the ASF versus increasing angular span of the tomosynthesis acquisition. A decrease in the ASF is observed with increasing angular span. Reprinted with permission from Tucker et al., Med. Phys., 40, 031917-8, (2013). Copyright 2013, American Association of Physicists in Medicine.....	68
Figure 5.6 MTF plots comparing the 70 µm pixel size and the 140 µm pixel size. MTF at 10% was used as the figure of merit. The 70 µm pixel size (5.1 cycles per mm) when compared to the 140 µm	

case (4.2 cycles per mm) was approximately 25% better. Reprinted with permission from Tucker et al., Med. Phys., 40, 031917-8, (2013). Copyright 2013, American Association of Physicists in Medicine.	70
Figure 5.7 Magnified view of the 0.54 mm speck cluster found in the ACR phantom. ASF analysis was completed on all specks in the cluster for each configuration	71
Figure 5.8 Graph comparing the calculated MC area for both imaging modalities. s-DBT resulted in smaller MC areas for each MC measured	81
Figure 5.9 Reconstruction slice of a specimen with a large cluster of MCs using the s-DBT system (Top-Left) and the continuous motion DBT system (Top-Right). MC sharpness is superior in the zoomed in s-DBT reconstruction (Bottom-Left) com- pared to the continuous motion DBT system (Bottom-Right). Reprinted with permission from SPIE. Tucker et al., Increased microcalcification visibility in lumpectomy specimens using a stationary digital breast tomosynthesis system, Proc. of SPIE, 2014.	82
Figure 5.10 Magnified ROIs of 6 MCs. The row above contains the s-DBT reconstruction images, while the row below contains the conti- nuous motion DBT system reconstruction images. Less blur is the x-y plane is visually observed for all 6 MCs. Reprinted with permission from SPIE. Tucker et al., Increased microcalcification visibility in lumpectomy specimens using a stationary digital breast tomosynthesis system, Proc. of SPIE, 2014.....	82
Figure 5.11 Comparison of the FWHM of the ASF for s-DBT and contin- uous motion DBT.s-DBT's wider angular span resulted in nar- rower ASF	83
Figure 5.12 Plot of the ASF for s-DBT and continuous motion DBT for MC number 6. The larger angular coverage of the s-DBT system red- uces out-of-plane reconstruction artifacts. Reprinted with permis- sion from SPIE. Tucker et al., Increased microcalcification visi- bility in lumpectomy specimens using a stationary digital breast tom- osynthesis system, Proc. of SPIE, 2014.....	83
Figure 5.13 (Left) FFDm image of a patient in the MLO view. (Right) Recon- structed slice of the same patient in MLO view. In the s-DT recon- structed slice, a speculated mass is clearly observed while this is not observed in the 2D image. Tumor extension towards the skin is visible only in the s-DBT slice. Reprinted from Jabari Calliste et al. SPIE Med. Imaging Phys. Med. Imaging (2015), p. 941228 ²⁵	86

Figure 5.14 Magnified ROIs with calcification clusters. (I) Zoomed in image of a suspicious mass in (a) a FFDM image and (b) an s-DBT reconstructed slice with the mass in focus, of a patient breast with known lesions. (II, III, IV) Zoomed in images of MC clusters in (a) FFDM image and (b) an s-DBT reconstruction slice with the MC cluster in focus, of a patient breast with known lesions. Reprinted from Jabari Calliste et al. SPIE Med. Imaging Phys. Med. Imaging (2015), p. 941228.....	87
Figure 6.1 Geometry of the 2G s-DBT system (left) front view (right) side view.	97
Figure 6. 2 (Left) s-DBT system with integrated CNT x-ray source array (XinRay Systems LLC, Research Triangle Park, NC) with 21 x-ray sources. (Right) GE SenoClaire system that utilizes 9 projection images over a 25° angular span.	99
Figure 6.3 The cathode current waveform and anode current waveform for a 60 ms pulse width from 8 different CNT sources. The results indicate that with ECS all CNT sources can consistently produce 43 mA cathode current across all sources.	104
Figure 6.4 Focal spot measurement using a pinhole phantom. (Left) A pinhole image acquired at 40 kVp. (Right) Shows the normalized intensity profile of the length of the pinhole image.	105
Figure 6.5 Focal spot size measurement of 21 sources in the source array. The results show a good source-to-source consistency.	106
Figure 6. 6 Experimentally measured, and simulated spectra for 49 keV tube potential.....	107
Figure 6.7 Geometry calibration results. (Left) X coordinates of focal spots in the 2G s-DBT source array using the optimization method. (Right) Shows the error of the coordinates from a straight line.....	108
Figure 6.8 Geometry calibration results. (Left) Y coordinates of the focal spots (Right) show the errors in the angular distribution of sources calculated from the y coordinates.....	109
Figure 6.9 Measure entrance dose rate for Hologic DBT system, Gen 1, and Gen 2 s-DBT system	110
Figure 6.10 (a) A reconstructed in-focus slice of the 50 μm cross wire phantom. The ROI highlighted by the white box illustrates an example of the region used to calculate the MTF. (b) The accompanying LSF of the horizontal tungsten wire and the Gaussian-fitted LSF.....	114

Figure 6.11. Projection MTFs of the two FDA approved devices and both s-DBT systems.....	115
Figure 6.12. MTF measured from the central source projection for different heights above the detector for the Gen 2 s-DBT system (a) scanning direction (b) chest wall direction.....	116
Figure 6.13 The system MTFs of the Selenia dimensions system compared to the 2 nd generation system utilizing the AFVR and FBP reconstruction methods.....	116
Figure 6.14. (Left) ACR phantom imaged using the 2 nd generation DBT system. (Right) Magnified view of 4 th group of Al ₂ O ₃ specks, each of the 6 specks are visible.....	117
Figure 6.15. (Left) A magnified view of the 0.54 mm speck cluster in the ACR phantom used for ASF analysis. Plot of the ASF for a 35° angular span for AFVR and FBP reconstruction methods. Both the raw data and the fitted data are shown. The AFVR reconstruction method resulted in a marginal decrease of the ASF.	118
Figure 6.16 Shows a three slice comparison of one of the 0.54 mm specks in the ACR phantom for both AFVR and FBP reconstruction methods. At each slice depth, the FBP slices look a bit blurrier than the slices from AFVR method.	119
Figure 7.1 Schematic diagram of contrast enhanced imaging.....	131
Figure 7.2 Mass attenuation coefficient as a function of photon energy for iodine and breast tissue	137
Figure 7.3 Pictures of the CIRS BR3D phantom together with the custom made phantom used for contrast enhanced imaging experiments.	138
Figure 7.4 Graph of mean energy against increasing Cu filter thickness for simulated x-ray tube spectra with increasing peak voltages ranging from 45 – 49 kVp.....	141
Figure 7.5. Simulated entrance dose rate for the corresponding tube energy spectra as in Figure 7.4. System geometry use to simulate dose rate were synonymous to the Gen 2 s-DBT system.....	142
Figure 7.6. The simulated effect of increasing Cu filter thickness on a 49 kVp tube spectrum. As Cu filter thickness increases, the photon flux is reduced and the modal energy shifts to the right.	143
Figure 7.7 Simulated effect of increasing Cu thickness on a normalized 49 kVp spectrum. The normalized spectrum shows the reduction in the amount of lower energy photons, resulting in an increase of photons at higher energies, increasing the mean energy value.....	144

Figure 7.8 Simulated calculations of the normalized absorbed dose spectra in iodine for a 49 kVp tube voltage with increasing Cu filter thickness.....	145
Figure 7.9. This graph displays the simulated calculations of the effective absorption energy of iodine, and the effective mass attenuation coefficient of iodine with increasing Cu filter thickness.	147
Figure 7.10. Normalized photon fluence for low energy spectra in DE imaging simulations the simulated calculations of the effective absorption energy of iodine, and the effective mass attenuation coefficient of iodine with increasing Cu filter thickness.	148
Figure 7.11. Simulated calculations of the effective absorption energy of iodine, and the effective mass attenuation coefficient of iodine for the low energy, dual energy spectrum range.	148
Figure 7.12. Simulated calculations of the normalized absorbed dose spectra in iodine for LE, 30 kVp, and HE 49 kVp with 0.25 mm Cu filter. This dual energy spectra pair was used in the phantom experiments.	149
Figure 7.13 Reconstructed iodine signal values against iodine areal density without scatter correction. A linear relationship is observed for all phantom thickness in the plot. The sensitivity of iodine quantification reduces with increasing phantom thickness.....	150
Figure 7.14 (a-c) Non-scatter corrected pre-contrast, post-contrast, and the logarithmic subtraction for the 5 cm CE phantom with areal concentration 2.5 mg/cm ²	151
Figure 7.15 (a-c) PSD corrected pre-contrast, post-contrast, and the logarithmic subtraction for the 5 cm CE phantom with areal concentration 2.5 mg/cm ²	151
Figure 7.16 Line profiles across the iodinated regions for the non-scattered corrected and PSD scatter corrected subtracted projection image for the central source.....	152
Figure 7.17 (a) In-focus reconstructed slice for the (a) non-scatter corrected subtracted image acquisition set, and (b) PSD scatter corrected subtracted image acquisition set. The scatter corrected reconstructed image shows increased contrast compared to the non-scatter corrected.....	153
Figure 7.18 Line profiles across the iodinated regions for the reconstructed in-focus slices of the non-scatter corrected and scatter corrected tomosynthesis acquisitions. Edge effects due to tomosynthesis reconstruction are apparent in the line profiles.....	154
Figure 7.19 Reconstructed iodine signal values against iodine areal density with PSD scatter correction. A linear relationship is observed for all	

phantom thickness in the plot. Though sensitivity is reduced with increasing phantom thickness, there is increased sensitivity compared to the non-scatter corected reconstructions	155
Figure 7.20 (a-c) Non-scatter corrected HE, LE, and the weighted logarithmic subtraction for the 5 cm CE phantom with areal concentration 3.75 mg/cm ² . (d-f) Corresponding PSD scatter corrected images in the same order	156
Figure 7.21 Line profile across iodine regions for DE weighted subtracted projection images shown in Figures 7.22(c) and 7.22(f).	156
Figure 7.22 (a-c) Scatter corrected reconstructed slices containing iodine regions of 3.75 mg/cm ² areal concentration for the 3, 4 and 5cm thick CE phantom.....	157
Figure 7.23 Line profiles across the iodine regions for the DE subtracted reconstructions for phantoms thicknesses of 3, 4 and 5 cm. The line profile shows the slight decrease in signal with increasing phantom thickness.....	158
Figure 7.24 Reconstructed iodine signals for the scatter corrected DE subtractions against iodine concentration.	159
Figure 7.25. Comparison of the reconstructed iodine signals for both TS and DE imaging for different phantom thicknesses against increasing areal concentration. The TS subtraction is significantly more sensitive than DE imaging.....	160

LIST OF ABBREVIATIONS

2D	Two-dimensional
3D	Three-dimensional
ACR	American College of Radiology
ASF	Artifact Spread Function
BI-RADS	Breast Imaging-Reporting and Data System
CC	Craniocaudal
CE	Contrast enhancement
CM	Continuous motion
CNT	Carbon Nanotube
CT	Computed Tomography
Cu	Copper
DBT	Digital Breast Tomosynthesis
DE	Dual energy
DM	Digital mammography
ECS	Electronic Control System
EHS	Environmental Health and Safety
FBP	Filtered Back-Projection

FDA	Food and Drug Administration
FFDM	Full Field Digital Mammography
FFT	Fast Fourier Transform
FOV	Field of View
FWHM	Full Width at Half Maximum
HE	High energy
IRB	Institutional Review Board
I-V	Current-Voltage
keV	kiloelectronvolt
kVp	peak kilovolt
LE	Low energy
MC	Microcalcification
micro-CT	Micro Computed Tomography
MQSA	Mammography Quality Standards Act
mR	milliRoentgen
MRT	Microbeam radiation therapy
MTF	Modulation transfer function
SART	Statistical iterative reconstruction technique

s-DBT	Stationary digital breast tomosynthesis
SdNR	Signal difference to noise ratio
SID	Source to imager (detector) distance
SOD	Source to object distance
SSM	Step-and-shoot motion
TS	Temporal subtraction
UNC	University of North Carolina at Chapel Hill

CHAPTER 1:Introduction

1.1 Dissertation Overview

The primary goal of this dissertation is to develop and characterize a second generation stationary DBT system with higher tube flux, and a wider angular span than the first generation system. The 1G s-DBT system, which is currently being evaluated in a clinical trial, has a limited tube flux, which requires longer imaging times for patients with large or very dense breast. Since s-DBT has shown improved spatial resolution over a continuous motion DBT system, lessening patient imaging time would further improve image resolution. In addition, increasing the system angular span increases the system's depth resolution. As image acquisition times for s-DBT are independent of the angular coverage, an s-DBT system can take advantage of increasing depth resolution without compromise on imaging time.

The secondary goal of this dissertation is to investigate the feasibility of contrast enhanced imaging with s-DBT. CE imaging with current DBT systems are subject to long imaging times due to tube movement. These long imaging times result in registration artifacts between imaging pairs when patient motion is present. Additional, tube motion results may result in subtraction artifacts between image pairs. Coupling CE imaging with an s-DBT system should potentially reduce image acquisition times, as well as eliminate registration artifacts due to tube motion. The viability of CE imaging with the 2G s-DBT system was investigated using a phantom and contrast enhanced medium in evaluating the signal of the subtracted CE images.

1.2 Specific Research Aims

1.2.1 Development and characterization of the 2G s-DBT system

The 2G s-DBT system was constructed by retrofitting a linear CNT x-ray source array to the Hologic Selenia Dimensions DBT system. The CNT x-ray source was electrically integrated to the Hologic system and a customized operating software via LabView was developed for seamless operation. An external collimator was designed and attached to the system prior to system characterization. The system was then evaluated for spatial resolution, and entrance dose rates using common quality control methods.

1.2.2 Feasibility of CE s-DBT

In this specific aim, CE imaging was evaluated using a costumed made phantom that allowed for different concentrations of iodine to be imaged. The two methods of CE imaging, temporal subtraction and dual energy imaging, were evaluated. The subtracted iodine signal was evaluated against iodine concentration to investigate whether the s-DBT system is capable of iodine quantification.

CHAPTER 2:Physics of X-ray imaging

2.1 Discovery of X-rays

Wilhelm Conrad Röntgen, a German physicist discovered x-rays in November of 1895 in his laboratory at the University of Würzburg. Prior to his discovery, physicist had been observing high voltage discharges in vacuum tubes. Röntgen was investigating these phenomena in a Crookes tube operated at high voltages. While experimenting in his darkened laboratory, Röntgen observed that a barium platinocyanide screen, lying several feet from the tube fluoresced. Furthermore, Röntgen observed that even when the tube is covered with solid materials such as paper, cardboard, and wood, such that visible light cannot penetrate, the screen still fluoresced. He soon postulated that the fluorescence was caused by some invisible rays, and after a series of experiments found that these rays could traverse through some materials and stopped by denser materials. He named his newly found, invisible, penetrating rays x-rays, as the letter x denotes the unknown in mathematics. Röntgen quickly realized the potential of the new radiation in medicine when he famously imaged his wife's hand using the tube and a photographic plate. As a result, Röntgen received the first Nobel Prize for Physics in 1901 for his discovery of x-rays. In 1913 William Coolidge improved on the Crooke's tube, producing an electrically heated cathode tube: the prelude to all modern x-ray tubes.

2.2 Generation of X-rays

X-rays beams are classified as electromagnetic radiation. They are generated whenever a stream of fast moving electrons undergo deceleration, which can happen in nature. However, since the discovery of x-rays, scientist have found several ways of generation, with the most

common and widely used is by means of an x-ray tube. The x-ray tube is a device capable of obtaining free electrons, and using high voltage to accelerate them onto a target¹.

As previously mentioned in Section 2.1, W. D. Coolidge invented a new type of x-ray tube which employs the principle of the Edison effect. The Edison effect is the name given to the phenomenon observed by Edison, which was the flow of electrons to a cool metal plate in an evacuated chamber from a heated metal filament (thermionic emission). In a typical x-ray source, electrons discharged from the heated filament are accelerated towards a metal surface target by applying a voltage between the metal filament and the target metal. The accelerated electron stream collides with the target of the x-ray tube, resulting in the kinetic energy of the electrons being converted to heat, light and x-rays². The x-rays are produced by two processes: Bremsstrahlung radiation and characteristic radiation.

2.2.1 Bremsstrahlung X-rays

Bremsstrahlung x-rays are the primary source of x-rays from an x-ray tube³. The accelerated stream of electrons penetrate the anode target material, approaching the strong positive nuclear field of one of its atoms. The strong attraction between the opposite charges causes the electron to deviate from its initial path^{2,3}. The deceleration of the electron results in a loss of kinetic energy which is radiated as an x-ray of equal energy². Accelerated electrons vary in speeds at which they approach the target metal, and how closely they approach the nuclei. As different electrons decelerate differently, the corresponding loss of kinetic energy varies, resulting in x-rays with varying energy². Electrons may have multiple bremsstrahlung interactions in the anode material, resulting in partial energy loss, or in the rare event of collision with the nucleus, total energy lost. This yields emitted photons with a range of energies, equal to

or less than the energy of the incident electron³. Figure 2.1 shows the mechanism of bremsstrahlung radiation.

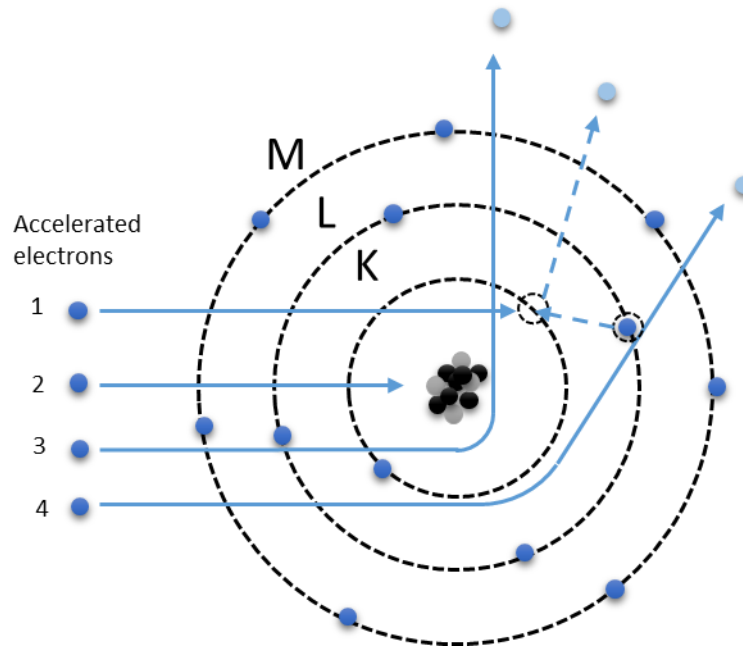


Figure 2.1 Illustration of four electron interactions that produce Bremsstrahlung radiation

The bremsstrahlung spectrum is sometimes referred to as a continuous spectrum, with the highest energy being equal to the potential difference between the anode and cathode. Figure 2.2 shows an example of the distribution of energies from bremsstrahlung radiation. The shape of the graph shows that bremsstrahlung interactions at lower energies occur a lot more frequently than at the highest energy possible, due to rare direct collision with electrons and nuclei. At even lower energies, the generated bremsstrahlung radiation is absorbed by the anode, essentially goes to zero³.

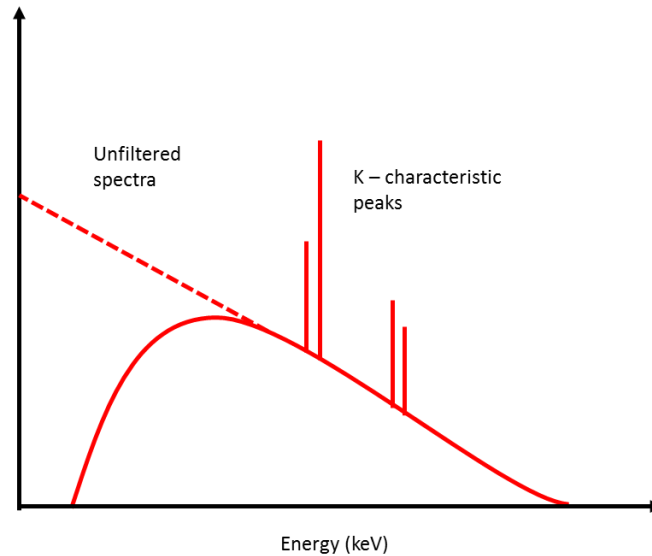


Figure 2.2 An illustration of Bremsstrahlung radiation spectrum for an arbitrary peak tube voltage

2.2.2 Characteristic X-rays

Characteristic radiation is the other process by which x-rays are generated in an x-ray tube. An electron with kinetic energy E_0 may interact with atoms of the anode target by ejecting an inner orbital electron (for example, K or L electron). This creates a vacancy in one of the electron orbital shells, leaving it in an ionized and excited state ^{2,4}. Consequently, the electron hole is instantly filled by an electron from an outer valence shell. This causes energy to be given off in the form of electromagnetic radiation called characteristic radiation ². The emitted electromagnetic radiation is called characteristic radiation because the energies of the photons are equal to the energy differences of the two shells between which the transition occurred, unique to a given element ⁴. The mechanism of characteristic x-ray production is illustrated in Figure 2.3.

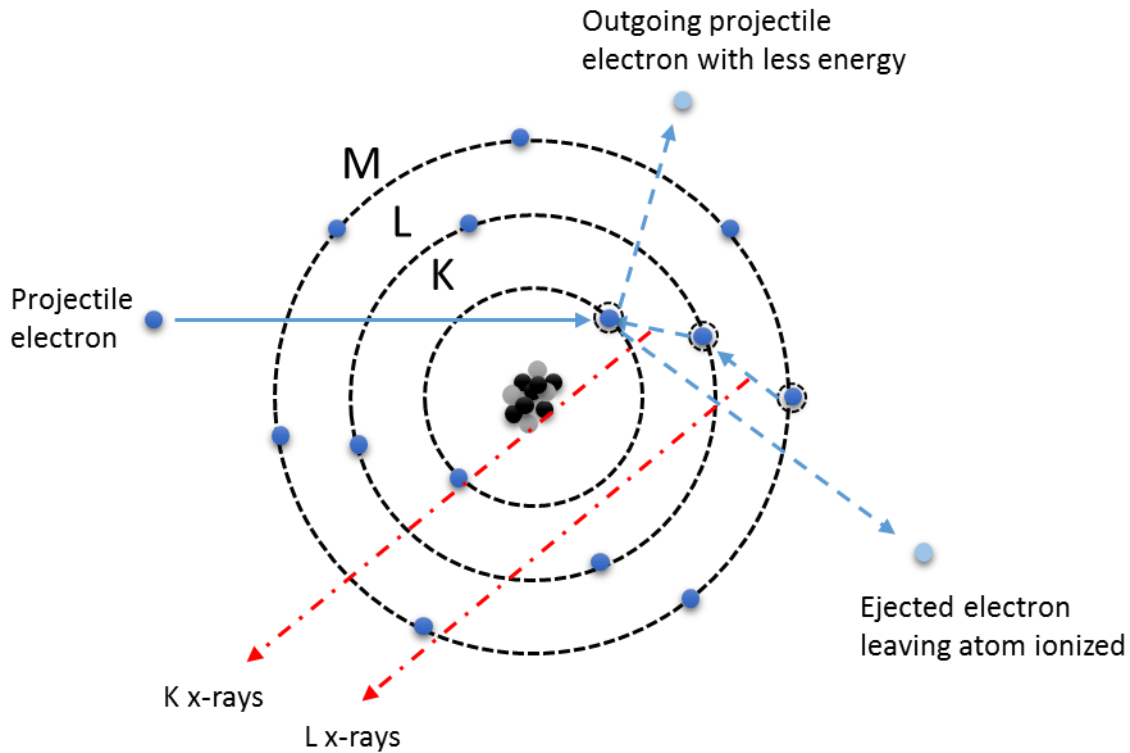


Figure 2.3 An illustration of the mechanism of characteristic x-ray production.

There are several discrete energy peaks that can arise from a number of electron transitions that occur from adjacent and nonadjacent shells in the target atom. In the diagnostic energy range, the K-shell vacancy is responsible for the most dominant characteristic x-rays, as electrons are transferred from the L, M, and N shells. The characteristic x-ray transition is denoted by the shell capturing the electron, and an α or β subscript which indicates whether the transition was from an adjacent or nonadjacent shell. Electron transitions from the L to the K shell are labeled as K_{α} and transitions from the M, N, or O to the K shell are labeled K_{β} . A K_{β} x-ray has higher energy than a K_{α} x-ray. These characteristic peaks are superimposed on the continuous bremsstrahlung spectrum, as show in Figure 2.2.

2.3 X-ray Interactions in matter

Most x-ray photons do not interact with atoms in the body and pass through unaffected. However, some x-ray photons undergo scattering and absorption upon interacting with a body of matter, which reduces the intensity of the x-ray beam. More specifically, there are four ways x-ray photons interact with atoms in their path: photoelectric absorption, Rayleigh scattering, Compton scattering, and pair production. The latter of the four is irrelevant to diagnostic radiology³.

2.3.1 Photoelectric Absorption

Photoelectric absorption occurs when an incident x-ray photon gives up all its energy to an inner orbital electron (usually K or L shell). For this to occur, the photon has to have slightly greater energy than the binding energy of an inner orbital electron. Consequent to the interaction, the electron is then emitted from the atom with kinetic energy equal to that of the photon, minus the binding energy of the electron shell, resulting in a photoelectron. The energy of a photoelectron is expressed in the following equation:

$$E_{\text{kinetic}} = hf_{\text{photon}} - E_{\text{binding}} \quad (2.1)$$

where E_{kinetic} is the kinetic energy of the photoelectron, hf_{photon} is the energy of the incident photon, and E_{binding} is the binding energy of the orbital electron^{3,5}.

The ejected electron leaves a hole in that shell rendering the atom positively ionized and in an excited state. This causes the immediate shift of an electron from a higher energy shell to the vacancy in the lower energy shell, filling the vacancy (Figure 2.4). The energy difference between the two shells is radiated as a photon known as a characteristic x-ray as its energy is specific to the element and shells concerned. This continues to occur as each newly formed hole is subsequently filled by an electron from an outer shell of higher energy, occurring in a

cascading sequence until the atom returns to its normal or ground state. The sum of energies of the characteristic photons in a single photoelectric interaction equals the binding energy of the shell from which the electron was initially expelled. In some instances, a competing process that is dominant in low atomic number elements takes place, known as Auger electron emission. This occurs when the energy released from the cascading electron is absorbed by an electron typically in the same orbital, ejecting the electron. The Auger electron's energy is the difference between the transition energy and the binding energy of the ejected electron⁵.

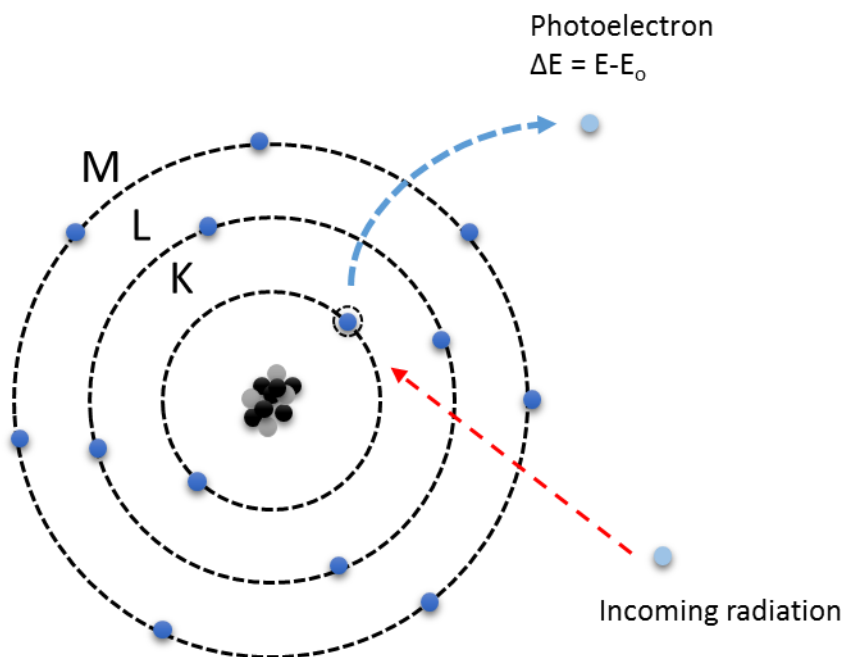


Figure 2.4 Illustration of photoelectric absorption interaction in matter.

The chance of occurrence of the photoelectric interaction is directly proportional to the cube of the atomic number (Z^3) and indirectly to the cube of the photon energy ($1/E^3$). The overall probability is explained as Z^3/E^3 . As a result, the probability of characteristic x-ray emission increases with increasing atomic number, and decreases with increasing energy. This is

significantly important in radiography, as the photoelectric occurrence between tissue, bone and contrast enhanced agents contribute to radiographic contrast⁵.

2.3.2 Rayleigh Scattering

The Rayleigh scattering mechanism involves the elastic or coherent scattering of x-rays by atomic electrons. Low energy x-ray photons may interact with closely bound orbital electrons' electronic fields and are scattered as a result. The x-ray photon is scattered in a forward direction without any change in energy to the incident photon. The probability of Rayleigh scattering is proportional to Z^2/E , and decreases as the photon energy is increased. This scattering occurs with low energy photons well below the range required for clinical radiology.

2.3.3 Compton Scattering

Compton scattering is the inelastic scattering of x-ray photons by an outer orbital electron. When an incident photon of adequate energy interacts with the loosely bound electron, it can displace the electron deflecting the x-ray photon in another direction (scatter photon). The resultant characteristic radiation is negligible in radiology as its energy is extremely low. This phenomenon is known as the Compton Effect and is expressed as:

$$E_{SC} = \frac{E_0}{1 + \frac{E_0}{511 \text{ keV}}(1 - \cos\theta)} \quad (2.2)$$

where E_{SC} is the energy of the scattered photon, E_0 is the energy of the incident photon, and θ is the angle of the scattered photon⁵.

An increase in photon energy decreases the probability of a Compton reaction, however, it increases the energy of the scattered photon and decreases the angle of deflection. This increases the chance of the scattered photon passing through the body reaching the image

receptor, contributing scattered radiation, which is counterproductive in radiology as it contributes form of noise.

2.3.4 Pair Production

This interaction does not occur in clinical radiology as it involves photons exceeding or equal to 1.022 MeV. At this energy, photons have ample energy to overcome nuclear electrostatic forces to be absorbed to then produce a pair of particles of equal mass: positron (positive electron) and electron.

2.4 X-ray Attenuation Tissue

The interaction mechanisms leading to the removal of photons from the x-ray beam discussed in the previous section contribute to varying degrees of attenuation in matter⁵. The attenuation of x-rays is what provides image contrast in medical x-ray imaging. The dominant mode of interaction of x-rays in the region on a body varies with photon energy, and the effective atomic number¹. For simplification, the human body comprises of three types of body tissue: bone, muscle and fat. Also present in the body during imaging is air, present in lung cavities, and sometimes contrast enhancement agents used for the accentuation of x-rays in specific regions⁶. The differential absorption of tissue, air, and contrast agents results in varying intensity of photons being transmitted through the region of the body, detected by the image receptor.

The amount of photons absorbed by each type of material is dependent on its linear attenuation coefficient, and thickness. If we model a polyenergetic x-ray beam as a monoenergetic source, the amount of photon lost (n) that pass through a thin slab (Δx) of homogenous material is expressed as:

$$n = \mu N \Delta x \quad (2.3)$$

where N is the number of incident photons, and μ the constant of proportionality defined as the linear attenuation coefficient^{3,5}. The difference in the number of photons that are transmitted, to the incident photons is

$$\Delta N = N' - N \quad (2.4)$$

$$= -n \quad (2.5)$$

$$= -\mu N \Delta x \quad (2.6)$$

Since the attenuation process is a continuous quantity, the thin slab of material is treated as an infinitesimally small quantity that leads to the differential equation

$$\frac{dN}{N} = -\mu dx \quad (2.7)$$

when solved yields

$$N = N_0 e^{-\mu \Delta x} \quad (2.8)$$

where N_0 is the number of incident photons, N is the number of transmitted photons, and x is the material thickness. X-ray beam intensity is proportional to the number of photons, so this equation can be written in terms of intensity as well,

$$I = I_0 e^{-\mu \Delta x} \quad (2.9)$$

where I_0 is the incident beam intensity, and I is the intensity after passing through the material.

In reality, the x-ray beam is polyenergetic having a spectrum distribution $S_0(E)$. Also, the linear attenuation coefficient depends on the composition of the material, and the spectrum distribution. Therefore the linear attenuation coefficient, $\mu(E)$, should be treated as a function of energy. Taking this into consideration the overall intensity of an x-ray beam is given by

$$I(x) = \int_0^\infty S_0(E') E' e^{\int_0^x -\mu(x'; E') dx'} dE' \quad (2.10)$$

This equation presents a good model for heterogeneous materials, however since μ is acutely mathematically complex, it is usually estimated and the effective energy of the polyenergetic source is used.

2.5 Conventional X-ray Tubes

The most conducive way to controllably generate x-rays is using an x-ray tube. The fundamental design of current x-ray tubes is similar to the Coolidge tube which generated x-rays thermionically. The x-ray tube consist of a cathode and anode assembly, in a glass tube housing that has been evacuated to high vacuum. The cathode is essentially a tungsten filament that emits electrons via thermionic emission. The anode consist of a metal target, and when high voltage is applied between the anode and cathode, electrons are accelerated towards the anode at high velocities. The bombardment of electrons on the target results in both Bremsstrahlung and characteristic radiation. The physics of x-ray production was previously discussed in section 2.21 and 2.22. The resulting x-ray beams emerge through the x-ray window of the tube housing. Figure 2.5 is a schematic representation of a conventional x-ray tube.

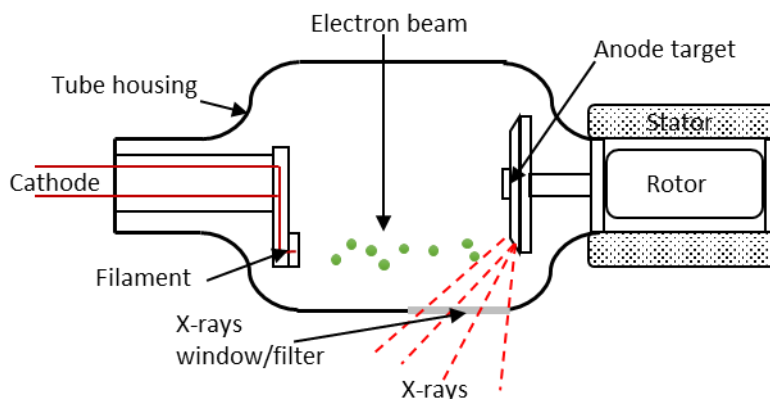


Figure 2.5 Illustration of modern x-ray tube. Major components of the tube include the cathode, anode, and tube housing.

2.5.1 Cathode Assembly

The cathode assembly mainly consist of a filament, supporting wires and a focusing cup. In most x-ray tubes, the filament is made of coiled tungsten wire connected to supporting wires that will supply the electric current. One of these wires is also connected to a high voltage power supply, which provides the high negative potential needed to accelerate the electrons towards the anode. A low voltage (8V to 12V) is applied to the filament which generates enough current to heat the filament and energize electrons. When electrons achieve a higher energy than the work function of the metal, electrons are emitted (thermionic emission). The focusing cup is a negatively charged concave metal cup which houses the filament. When independently supplied with a high negative voltage, it can further narrow the electron beam width to produce a small focal spot distribution on the anode.^{4,5}

2.5.2 Anode

The anode is the origination of x-ray radiation in an x-ray tube. Since more than 99 percent of the electrons' kinetic energy is converted to heat at the anode, the anode must be constructed of materials with high heat capacities, and it must be capable of rapid heat dissipation. In addition, anode construction requires materials of high atomic numbers for efficient of x-ray production. The most common anode target material is tungsten as it has an atomic number of 74, and a melting point of 3370°C making it suitable as a target metal ⁴.

There are two main types of anodes: stationary anode, and rotating anode. Depending on the x-ray unit, one of two main types of anodes are implemented into the system. Small x-ray or low powered units (for example, dental units) use a stationary anode design backed by a metal (usually copper) that has better conduction than tungsten. However for units that require higher x-ray output, the rotation anode is a more efficient design. The basic design of a rotation anode

consist of a tungsten disk, with a precisely beveled edge of the required anode angle. The anode disk inside the x-ray tube housing is connected to a metal rod arranged around bearings so that the anode can rotate freely ³. The metal rod is then connected to the rotors of an induction motor outside of the housing as seen in Figure 2.5. Throughout rotation of the anode, the electron beam bombards a “new spot” so that the heating effect spreads around a large area known as the focal track, located on the beveled face ². An anode’s ability to accumulate, store, and discharge heat limits the power of an x-ray tube. Generally, an increase in the area of the focal track and higher anode rotation rpms allow for better heat dissipation ^{2,3}.

2.5.3 Tube Housing

The cathode assembly and anode are enclosed in a tube usually made of a boro-silicate glass. As mentioned earlier, a high vacuum must be achieved and maintained for the generation of electron beams. As a result, the x-ray tube housing must be capable of withstanding atmospheric pressure while under high vacuum, able to withstand heat generated by the anode, and transparent to the heat radiated from the anode. An x-ray window situated on the tube where the x-rays are directed, which is usually made of thinner material.

2.5.4 Focal Spot

The focal spot is an import component of an x-ray tube. Resolution of an x-ray system is partially determined by focal spot size. The focal spot is actually the area on the anode where the accelerated electrons from the cathode impact the anode, more specifically known as the real focal spot of the electron beam. The area of the projection from the anode out the tube towards the detector plane is known as the effective focal spot size. The bombardment of the anode results in the generation of heat, limiting the energies and time to generate photons as the heat will melt and destroy the anode. Consequently, the design of the focal spot is a compromise

between the requirements of a small focal spot size that produces enough photon flux coupled with prevention of melting the anode. To compensate for heat loading, the electrons are focused on a large area that is tilted relative to the incident beam causing the effective focal spot to be smaller. This is illustrated in Figure 2.6. The size of the effective focal spot is determined by the line of focus principle, giving the length of the effective focal spot size being equal to the real focus spot length times $\sin \theta$ ³.

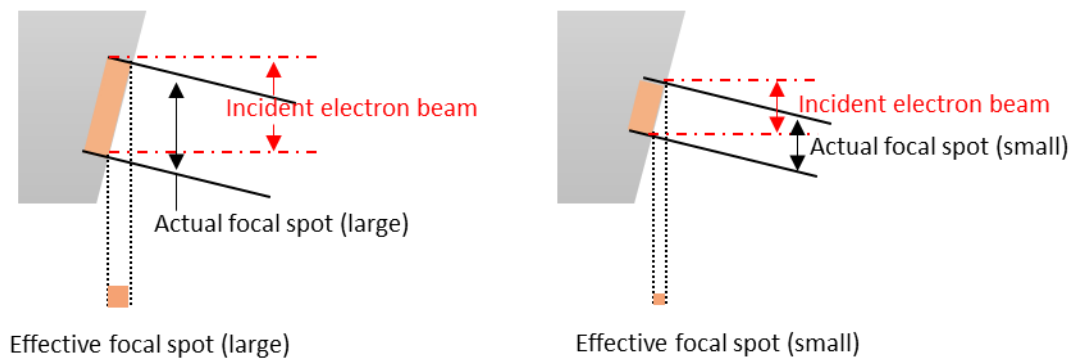


Figure 2.6 An illustration of the effect of the incident focal spot size on the effective focal spot size.

2.5.5 Window and Filter

The material of the x-ray tube window is important as it provides inherent beam filtration. Lower energy spectrum photons play no role in the image formation, and are absorbed by the first few centimeters of tissue contributing to patient dose. The x-ray tube window serves as the initial filter, absorbing low energy photons and improving beam quality. X-ray tube windows are usually thin and made with either glass, beryllium, or aluminum.

Additional filtration is applied to the outside of the window as needed resulting in total filtration. The purpose of additional filtration is to improve the beam quality by further removing

lower-energy photons. Removal of lower-energy photon increases the average energy of the spectrum, therefore giving it greater penetrating power. This is known as beam hardening.

2.5.6 Heel Effect

The Heel Effect gives rise to the non-uniformity of photon intensity across an x-ray beam. It is affected by the anode angle; an increase in anode angle, decreases the heel effect. This effect occurs when x-rays emitted near the anode are attenuated by the anode, reducing the x-ray flux to the image receptor. Consequently, the intensity of an x-ray beam decreases in the direction of the cathode to the anode. This effect is noticeable in clinical radiology as diagnostic tubes use low x-ray energies with steep anode angles. X-ray beams are usually collimated, or using a compensating filter to improve beam uniformity.

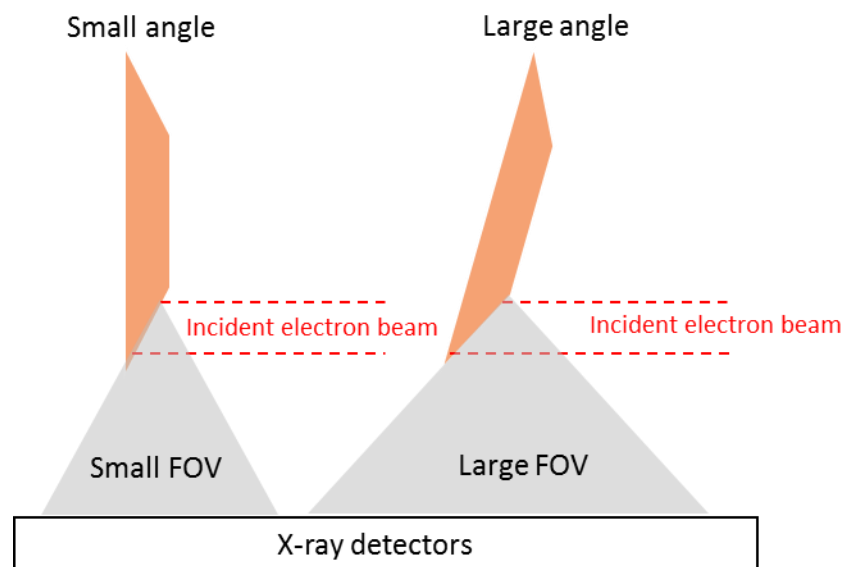


Figure 2.7 Illustration showing the effect of the anode angle on FOV, and the heel effect.

2.6 REFERENCES

- ¹ W.R. Hendee and E.R. Ritenour, *Medical Imaging Physics* (Wiley-Liss, 2002).
- ² J. Selman, *The Fundamentals of Imaging Physics and Radiobiology*, Ninth (Charles C Thomas, Springfield, Illinois, 2000).
- ³ J.L. Prince and J.M. Links, *Medical Imaging Signals and Systems* (Pearson Prentice Hall, Upper Saddle River, New Jersey, 2006).
- ⁴ F.M. Khan, *The Physics of Radiation Therapy* (Lippincott Williams & Wilkins, 2010).
- ⁵ J.T. Bushberg, J.A. Seibert, E.M. Leidholdt, J.M. Boone, and M. Mahesh, *Med. Phys.* **40**, 077301 (2013).
- ⁶ R. Behling, *Modern Diagnostic X-Ray Sources : Technology, Manufacturing, Reliability* (n.d.).

CHAPTER 3: Fundamentals of Mammographic Imaging

3.1 Breast Cancer Screening

Screening is a method whereby swift postulation of an unsuspected disease can be determined by means of an examination or other procedure in a population of asymptomatic women. The qualities of an ideal screening test include having high detection rates of cancers (true positive), and low false detection rates (false-positive), that subject patients to further unnecessary diagnostic testing¹⁻³. Essentially, a screening test should result in earlier detection of disease than previous methods, and ultimately result in the reduction of mortalities from the disease, or a major benefit such as eliminating the need for dangerous, harsh, or more invasive methods. Additionally, the degree of benefit must outweigh associated human risks, and economical aspect of the screening method^{3,4}.

Cancer screening procedures are developed by regulatory bodies in individual countries based on the national cancer incident and occurrence within the population. Specifics such as, age and frequency of screening coupled with cost must be taken into consideration. In addition, quality control measures must be implemented to ensure accuracy, consistency, and overall efficacy for screening equipment.

Screening provides many benefits. The main benefit of screening is the potential early detection of cancer to prevent death to an individual. An additional benefit is the prevention of more severe, costly treatment (prevention of chemotherapy and less surgery) of disease, and the associated trauma that comes with detection at a later stage⁴.

3.2 X-ray Mammography

Mammographic imaging is a medical imaging technique that uses low dose x-rays to obtain images of the breast anatomy. Specific equipment and techniques have been developed for the optimization of breast imaging since breasts are solely made up of soft tissue that have similar radiographic properties^{1,5,6}. For breast cancer screening, effectiveness is measured through clinical studies. Mammography has been shown to be significantly effective in the reduction of breast cancer mortality in randomized clinical trials as well as systematized screening studies⁵. X-ray mammography is the only noninvasive way for early detection of breast cancer in asymptotic patients.

The aim of x-ray mammography is to produce images with high spatial resolution that show the internal structure of the breast. Fine detail of the internal structure is necessary to detect mammographic features that are characteristic of breast cancer³. To further understand the requirements for x-ray mammography, the breast anatomy, and breast cancer features are covered in this chapter prior to description of mammographic imaging systems.

3.2.1 Breast Anatomy and mammographic features of breast cancer

The breast anatomy consist of adipose, glandular, and connective tissue. The tissue overlays the pectoral muscle extending from the clavicle down to the mid-sternum, and from the lateral border of the sternum to the axilla. The glandular tissue consist of lobules connected to the nipple by ducts (Figure 3.1), which are responsible for the lactation in breast. The darker skinned region around the nipple is called the areola. Fatty tissue surrounds the glands throughout the breast, which is held together by connective tissue and ligaments giving the breast its shape. The composition of glandular and adipose tissue varies from patient to patient as it is dependent on genetics and age.

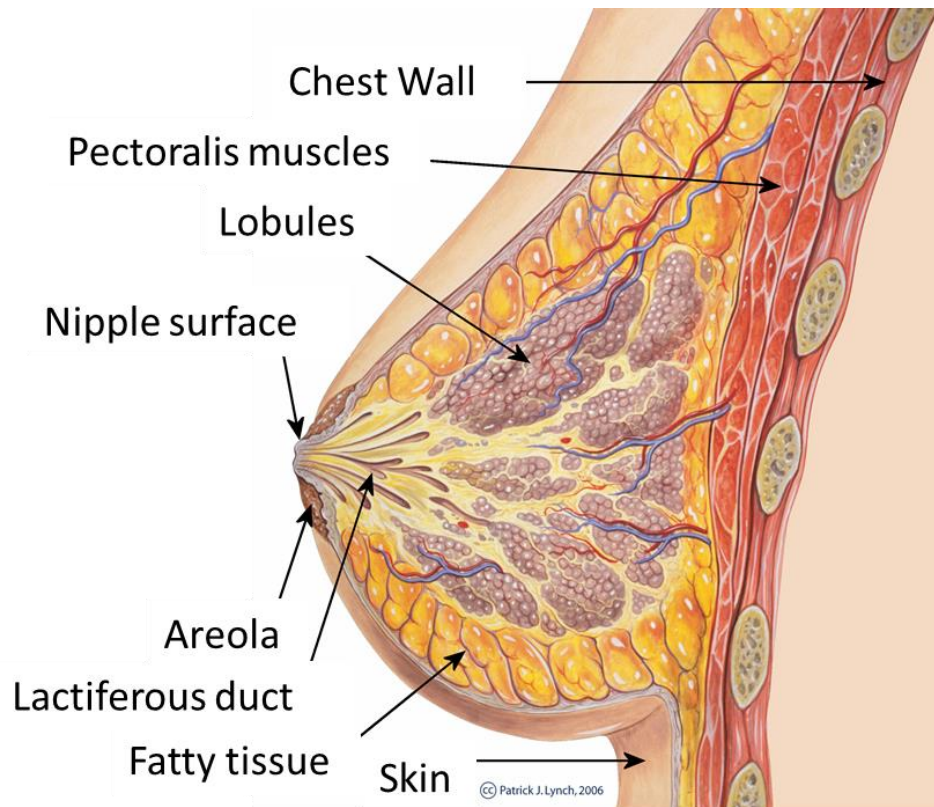


Figure 3.8 Diagram of breast anatomy. The diagram shows the major and surrounding structures of the breast. Image adapted from original © Patrick J Lynch. Reprinted with permission from the copyrighter based on the Creative Commons Attribution from Wikipedia.com

An important feature in the mammogram is determining the amount of glandular tissue present in the breast. On an x-ray image, the glandular tissue which is denser looks mostly white, while the adipose tissue looks like dark shades of grey. The ratio of the tissue on the mammogram is used to classify the breast density of patients according to the American College of Radiology (ACR) Breast Imaging Reporting and Data System (BI-RADS)². Table 3.1 shows the BIRADS classification for breast densities with their respective glandular tissue percentages⁷.

Table 3. 1 ACR BI-RADS Terms for Breast Density. Adapted from ACR BI-RADS Atlas 5th Edition^{8,9}.

Classification	Description	Percentage Glandular Tissue
a	Mostly Fat	< 25%
b	Scattered Fibroglandular	25 – 50 %
c	Heterogeneously Dense	51 – 75 %
d	Extremely Dense	>75%

The two general categories of mammographic findings that are indicative of cancer are masses and clustered microcalcifications. According to the ACR BI-RADS terminology, a breast mass is defined as a three-dimensional space occupying lesion that is seen on two mammographic projections². With a few exceptions, benign masses (non-cancerous) do not penetrate surrounding tissue, and have rounding (well delineated) borders, whereas malignant tissue extends through the basement membrane, invading surrounding glandular tissue. As a result, malignant masses are irregularly shaped with indistinct or spiculated margins. As the mass shape becomes more irregular, or mass margins become more spiculated, the probability that it is a cancer increases. Mass density is also important in determining whether the mass is malignant or benign. Its density is determined with respect to the fibroglandular tissue in the patient breast. Higher density masses have a higher chance of being cancers, though low-density ones do exist. Table 3.2 is a description of malignant masses according to ACR BI-RADS lexicon.

Table 3. 2 Description of the types of malignant masses according to ACR BR-RADS lexicon. Adapted from ACR BI-RADS Atlas 5th Edition^{8,9}

Shape	Margin	Density
Round	Circumscribed	High
Oval	Microlobulated	Equal
	Obscured	Low
Irregular	Indistinct	Fat containing
	Spiculated	

Associated calcifications in and around suspicious masses are also of concern since it may represent cancer. Calcifications are also present without masses which need to be analyzed as it may be the only indication of cancer. The prevalence of microcalcifications in mammograms are high, yet most microcalcifications are benign. Therefore, it is important to recognize individual size, and morphology and location of the cluster to determine whether cancer is present². Calcifications are usually found within the ducts of the breast and consequently take on the shape of the duct. The ACR BIRADS nomenclature for the assessment of microcalcifications are displayed in Table 3.3.

Table 3.3 . Description of the types of calcification clusters according to ACR BR-RADS lexicon Adapted from ACR BI-RADS Atlas 5th Edition^{8,9}

Calcification		
Typically benign	Suspicious morphology	Distribution
Skin	Amorphous	Diffuse
Vascular	Coarse heterogeneous	Regional
Coarse or “popcorn-like”	Fine pleomorphic	Grouped
Large rod-like	Fine linear or fine-linear branching	Linear
Round		Segmental
Rim		
Dystrophic		
Milk of calcium		
Suture		

3.3 X-ray Mammographic Imaging

Since normal breast tissue and cancerous tissue have similar attenuations of x-rays, the x-ray equipment needs to be optimized specifically for breast cancer detection. The range of energies with the largest attenuation difference is from 10 to 15 keV, and as energies increase, the difference decreases^{1,3}. However, at low energies there is high absorption of the x-ray energies, which causes high tissue dosage and long exposure times. Other than differentiating between tissues with small attenuation differences, detection of microcalcifications are also

important, as their size, morphology, and distribution are instrumental in diagnosis of diseased tissue^{3,4}. For the reason that x-ray mammography systems have to enhance the contrast between tissues of small attenuation differences, and detect microcalcifications while keeping patient dose to a minimum, dedicated x-ray tubes and other equipment are essential for x-ray mammography imaging^{1,3}. In order to ensure that optimal images are produced at the lowest possible patient dosage, quality control procedures have to be adhered to, which govern the design, and operation of an x-ray mammography system¹. This is further discussed in the following sections.

3.3.1 Influences on imaging quality

There are two factors that contribute to mammographic image quality: technical and clinical factors. Assuming that there is a close correlation between the two, only the technical aspects would be considered in this section. Mammographic image quality is the measure of how well the image achieves its purpose in demonstrating whether disease is present or not in the breast. The image must distinctly display physiological, and anatomical structures, including deviations from normal tissue caused by disease or injury¹⁰. A high quality mammogram should be able to depict features such as asymmetry between the left and right breast, distortions of normal structure of the breast tissue, characteristic morphology of masses, and the shape and distribution of calcifications^{1,3}. Several factors affect the extent to which these features are rendered optimal, and are the focus of this section.

Spatial Resolution

The spatial resolution in an image is contributed by four independent factors: geometric unsharpness, subject unsharpness, motion, and the image receptor. Geometric unsharpness is caused by the focal spot size, and the distances between the source to object and source to detector¹⁰. Figure 3.2(a) is a schematic of the relationship between focal spot size and geometric

unsharpness. The degree to which blurring increases, increases with the focal spot size, therefore a smaller focal spot size is favorable. Figure 3.2(b) illustrates the relationship with the source to object and source to detector distance relationship in geometric unsharpness. For a given size source, the extent of unsharpness decreases with an increase in the source to object distance. This can be done in either one of two ways, by moving the source further away from the object, or by moving the object closer to the image receptor^{3,10}. Geometric unsharpness becomes particularly important in spot magnification mammography. The ratio of the source to object distance (SOD) to source to imager distance (SID) governs the magnification at which the region of interest is imaged. For magnified imaging, the ratio of the SOD to SID is increased by raising the breast closer to the source. Accordingly, the geometric unsharpness is increased and is compensated for by using a focal spot of smaller size³.

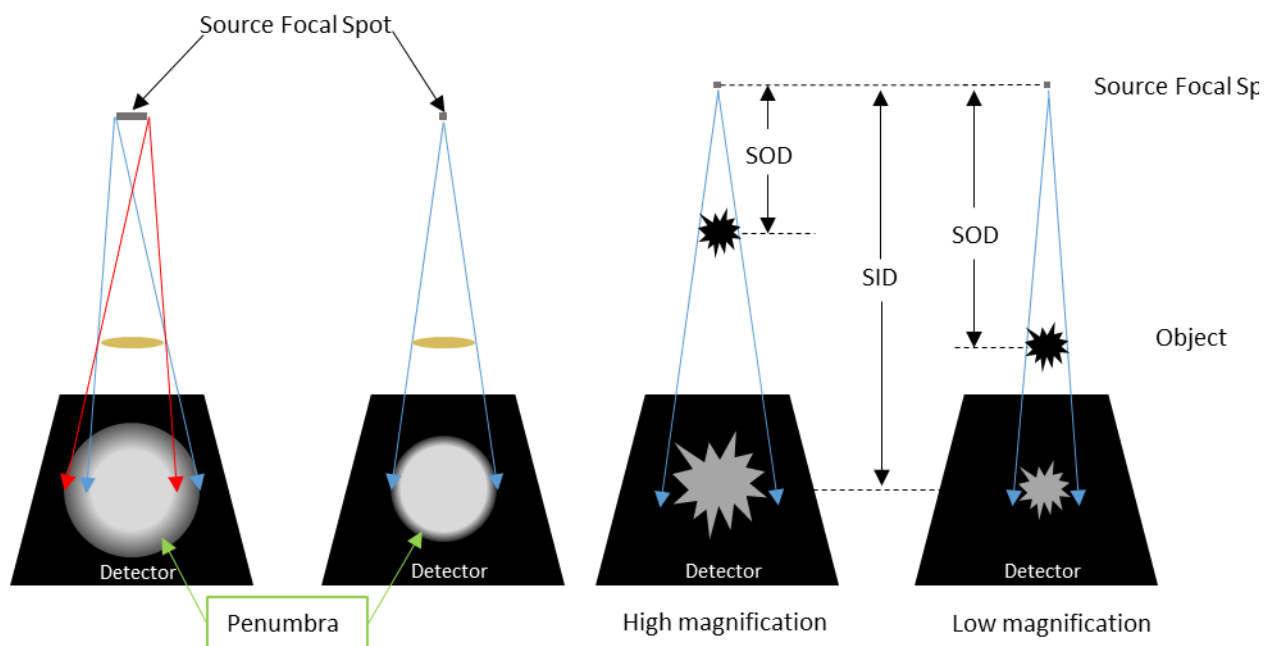


Figure 3.9 (Left) Schematic diagram showing the effect of focal spot size on resolution. (Right) Schematic diagram illustrating x-ray magnification

Subject unsharpness is sometimes referred to as absorption unsharpness. It can be the result of the composition of the object's structure in the patient, the shape of the object, or a combination of both¹⁰. This sometimes leads to a structure being anatomically indistinguishable from its background. Figure 3.3 shows a schematic diagram of the unsharpness due to the shape of an object.

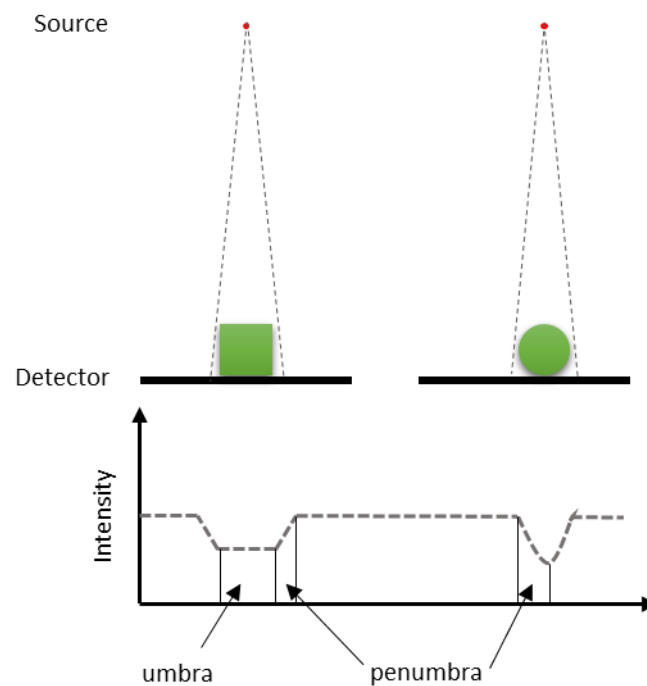


Figure 3.10 Illustration showing unsharpness in x-ray profile due to the shape of the object.

Motion unsharpness causes the margins of structures to become blurred as regions of the boundary may be projected onto different regions of the image receptor¹⁰. It's caused by both voluntary and involuntary movement of the patient. In mammography the main contributor is voluntary motion, and this can be reduced by shorter exposure times, and also compression to immobilize the breast³.

The image receptor is responsible for the formation of the final image, and the detector specifications dictate imaging parameters in mammography³. There is inherent unsharpness regardless of the type of image receptor used. In screen film mammography, thickness and composition of the light sensitive emulsion on the screen film influences the sharpness of structures in an image. Unsharpness increases with increasing thickness of the light sensitive emulsion, but the thicker the layer, the more sensitive it is to light¹. Therefore, a compromise has to be made with the composition of the film and thickness to optimize sensitivity and sharpness in short imaging times. In digital mammography, the digital receptors and display affect image sharpness. Data can be received and displayed in different modes that affect the level of unsharpness. Generally, digital receptors with smaller pixel sizes generate sharper images.

Contrast

Contrast is another key contributor to image quality in mammographic imaging. It indicates the degree to which subtle anatomical and physiological structures in the region of interest are differentiable in the image. The difference in radiolucency of the tissue being imaged, imaging receptor, and display methods are key contributing factors¹⁰.

The differences in tissue composition of the anatomical and physiological structures cause inherent “subject contrast” as they have differences in x-ray attenuation^{1,3,10}. Differences in contrast are the reflection of the thickness, physical density, and atomic number differences among different tissue¹⁰. As mentioned in section 1.2 there are only subtle differences in the composition of breast tissue leading to low inherent contrast. However, by adjusting various parameters on an imaging system for the optimization of breast imaging, the differences in the signals of the structures can be increased¹. Figure 3.4 is an illustration depicting the inherent contrast of tissue with varying thickness and different material compositions. With a

homogenous x-ray beam of incidence passing through the tissue of uniform attenuation coefficient, μ and varying thickness and composition, the intensity of the photons exiting the different regions will be different. The contrast is calculated as a difference in the signals, for example, the contrast between region 1 and region 3 is given by:

$$C_S = \frac{I_B - I_O}{I_B} \quad (3.11)$$

where C_S is the subject contrast, I_B intensity of the background, and I_O intensity in the region of the object. The intensity of photons exiting an object after traversing through an object is dependent on the attenuation coefficient and thickness. Synonymous to increasing thickness, increasing the attenuation coefficient, μ , decreases the signal¹. Since the breast is made up of soft tissue, lower energies with higher attenuation coefficient, and larger differential in attenuation values in the tissue are used to increase contrast between them.

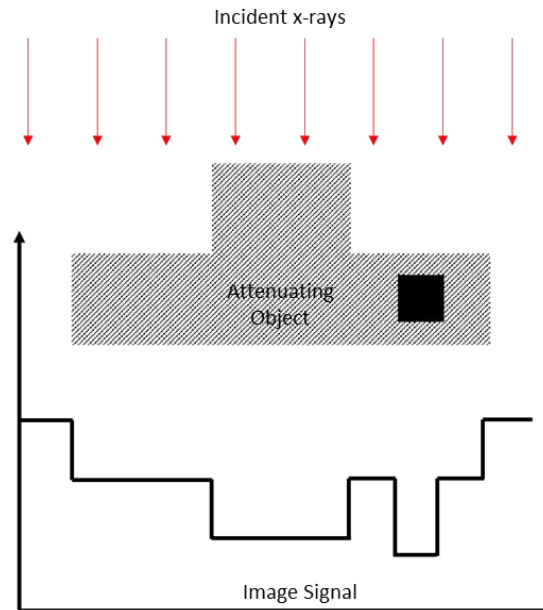


Figure 3.11 Demonstration of the effect of the attenuation coefficient on the contrast of an image. For the same material, there is an increase in attenuation with increasing material thickness, and for higher attenuating objects (darker object).

The imaging receptor converts the photons into intensity signals, and its characteristics are instrumental in producing contrast of the final image. Its contrast is determined by how well it can convert the differences in energy leaving the object into an output intensity signal^{1,10}. Specific to digital mammography, the contrast in the display can also be changed, within a dynamic range of the digital monitor.

Noise

Image noise is the information in an image that is useless, and a contributor to image degradation in x-ray imaging. All radiologic systems have some amount of noise. Sources of noise are from the tissue structure, radiation, the receptor, and quantum noise^{1,10}. Structure noise arises from the shadows of structures in the tissue that do not contribute information to the image. It is frequently responsible for missed lesions and abnormalities in images. Because of the breast volume and structure, it is standard for two projection views of each breast to be obtained for either screening or diagnostic imaging. The two views allow for an understanding of the superimposed structures that are present if only one view is taken, a means of working around structure noise.

Radiation noise is a consequence of non-uniformity of the x-ray beam due to the anode heel effect, and also scattered radiation. This interferes with the visualization of the anatomy in the imaged region because of its inhomogeneities^{3,10}. Tilting of the anode to combat the heel effect, and the use of anti-scatter grids help reduce the image noise permitting structures to be clearly seen. Quantum noise also influences the quantity of x-ray photons that the image receptor receives, and is usually the largest contributor of noise in imaging. The discrete nature of how the photons impinge on the surface of the detector leads to random fluctuations causing non-

uniformity in the image, and reducing the definition of structures^{3,11}. Sources that allow for sufficient photon flux, or longer exposures are necessary for the reduction of quantum noise.

Signal Difference-to-Noise Ratio

Since noise is counterproductive to visualization of objects in radiographic images, contrary to contrast and spatial resolution, it is useful to use the signal difference-to-noise ratio (SDNR) for the characterization of image quality⁵. The SDNR is the ratio of the detected signal difference to the standard deviation,

$$SDNR = \frac{S_{ROI} - S_B}{\sigma_B} \quad (3.12)$$

Where S_{ROI} is the average signal for the ROI, S_B the average signal of the background, and σ_B the standard deviation of the background. It is more meaningful to consider a region than to consider evaluating single pixels as it corresponds to a lesion or object of interest, to an equal area of the nearby background⁵.

3.3.2 Mammographic equipment

Each component of an x-ray mammography system influences the quality of the resulting image. Understanding the composition of normal, and diseased breast tissue, and influences on mammographic imaging have led to the development of specific techniques, x-ray tube and system designs. In addition, the risks associated with ionizing radiation requires minimizing dose while keeping images optimal.

The x-ray tube design is the single most important component of a dedicated mammography system. The x-ray tube typically operates at voltages below 35 kVp as a means of maximizing contrast between soft tissues in the breast. The x-ray tube is usually configured with two cathode filaments in a focusing cup that can produce two different focal spot sizes. The

larger of the focal spots usually has a nominal size of 0.3mm, while the smaller has a size of 0.1 mm¹. The larger focal spot is used in standard mammography imaging where views of the entire breast are needed. When specific areas of the breast need to be imaged, for example microcalcification clusters, magnified views are needed. The use of the smaller focal spot minimizes geometric blurring and maintains the spatial resolution necessary for visualization of microcalcifications¹. Rotation anodes are employed as a means to maximize tube amperage and minimize imaging time. The anode placement away from the chest wall (nipple side), and cathode placement over the chest wall achieves a more even distribution of transmitted x-ray as the heel effect is further away from the patient. An effective anode angle of $\sim 22^\circ$ relative to the plane of the detector, for a source to detector distance of 65 cm is typical for total detector coverage. The x-ray tube must be capable of producing an acceptable tube output as defined by MQSA.

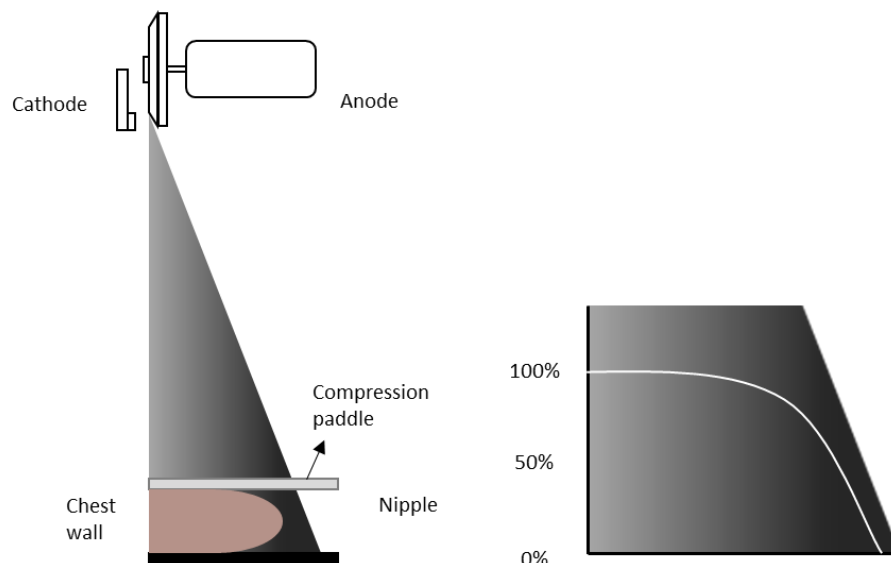


Figure 3.12 Illustration of a mammography unit's key components and orientation. Cathode and anode axis is along the chest wall direction, positioned such that the thicker side of the breast is under the cathode to promote a more uniform x-ray distribution. The figure on the right shows the fall off of intensity due to the heel effect. Adapted from

Other essential equipment necessary for mammography includes collimators, compression paddles, and anti-scatter grids. Collimators are fixed size metal apertures used to define the radiation field, focusing x-rays in the region of interest, and reducing scatter. Compression paddles are employed to reduce movement and achieve uniform tissue thickness. This yields less motion blur, and geometric blur of structures, as they are closer to the detector. It also acts to further reduce the amount of tissue overlap present in 2D mammography¹. Mammography systems also use antiscatter grids placed between the breast and the image receptor to reduce the scattered radiation transmitted through the breast.

Image receptors are another critical component of x-ray mammography machines. They are needed to provide imaging contrast, sufficient spatial resolution, and to allow for fast imaging times. There are currently two types of x-ray mammography machines: screen-film mammography and full field digital mammography. Screen film mammography involves using a cassette containing a screen film that needs to be developed as the image receptor. In full field digital mammography, the imaging receptor converts the photons into digital information, which is then sent to a digital monitor to be viewed. Both types of image receptors have particular requirements, and dictate the imaging parameters of the system³. These are discussed in the following two sections.

3.4 Mammographic modalities

3.4.1 Screen Film Mammography

Screen film mammography systems utilize film as the detector and the display medium. This introduces inherent disadvantages since imaging parameters have to be optimized to satisfy both imaging and viewing parameters, making all parameters interrelated. As a result, modification of any component forces a compromise of another to compensate for the change.

The mammography system's x-ray tube and geometry governs imaging parameters, making it critically important in determining the rate of exposure and beam quality of the x-ray beam. The x-ray tube, together with its power, distance, and the screen/film detector efficiency influences the time needed to produce an optimal image. This introduces a tradeoff between resolution and imaging speed. Ultimately, the overall system resolution is limited by the screen film detector's capacity to record and display the details of the breast that the other components of the system present ³.

Though film has high spatial resolution, it does not respond linearly to incident photons, and results in a very inefficient way to create radiographs. As a means to greatly improve their efficiency, films have been combined with intensifying screens on both sides of the film that stop the x-rays and convert them to light ¹¹. The end result is the efficient conversion to light, which exposes the film. A requirement of the FDA, is that all film/screen combinations designed specifically for mammography can resolve microcalcifications with sizes ranging from 200 to 300 μm ³. Development of film/screen detectors have resulted in different combinations of film/screen combinations, and choice is based on individual preference. Most modern screen film detectors use a single-emulsion film and single screen in the form of a radiography cassette. A schematic diagram of screen film detectors is represented in Figure 3.6.

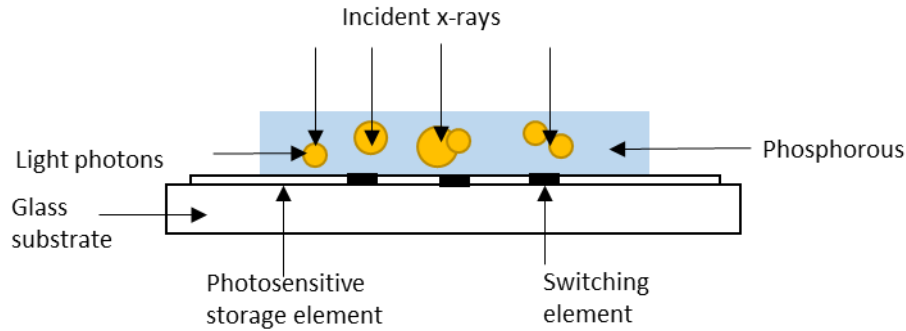


Figure 3.13 Schematic diagram of a screen film detector.

An additional limitation of film is that once the image is developed, it is unchangeable. Therefore, if the processed image is not optimal, it may result in repetition that introduces greater dose to the patient. It is also the only record of the image; therefore if it is misplaced, it cannot be retrieved. The physical space needed for the storage of x-rays images is another disadvantage.

3.4.2 Full Field Digital Mammography

The advent of digital detectors brought about the development of the digital mammography system. Digital mammography, contrary to SFM separates the acquisition of the image and its corresponding image display. Consequently, each part of the imaging sequence can be optimized giving this system unique properties. Mammography presents a great challenge for digital detectors because of the high spatial resolution required.

There are two main types of digital detectors used in mammography are indirect and direct detectors. Indirect detectors use a process that is synonymous to SFM, it uses a scintillator (usually cesium iodine) to absorb x-rays and generate a light scintillation. The scintillators are paired with either charged-coupled devices or thin-film transistor (TFT) panels. The CCD detector comprises of several million individual pixels that are charged by the incoming photons. The incoming light pattern creates a corresponding light pattern on the chip that is read out pixel

by pixel, then digitized and stored on a computer system¹². For indirect detectors using TFT panels, the converted light first encounters a photodiode layer that converts the visible light into electric charges. The TFT readout circuitry then transforms the charges into digital values for an image to be displayed and stored¹². Both indirect systems have an intrinsic degradation of resolution due to the scintillator screen spreading light.

Direct conversion detectors consist of an x-ray photoconducting layer that is grown directly onto a TFT charge collector and readout layer. Amorphous selenium is typically used as the photoconducting layer due to its superb x-ray detection properties, and high spatial resolution¹². Prior to x-ray exposure, an electric field is applied across the a-Se layer. During exposure, x-ray photons incident upon the layer of a-Se generates electrons and holes, and these charges migrate perpendicularly to the a-Se layer to the electrodes below without much lateral diffusion. The charges are stored in the charge-collection electrodes until readout^{3,12}.

Because of the conversion of analog signals to a digital matrix of number, compromises are made on the spatial resolution. For example, film screens have spatial resolutions greater than 20 cycles/mm, which would require a digital detector with pixel sizes of 25 μm . Very specialized monitors, and hard drives with huge capacities would have to be employed to realize this resolution.

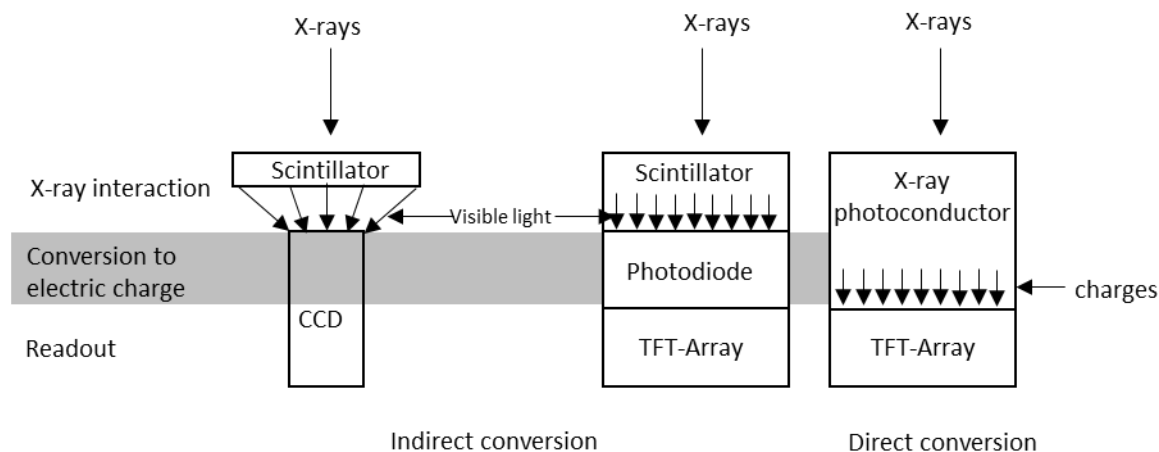


Figure 3.14 Illustration of the two types of digital detectors, indirect and direct conversion.

Advantages of digital mammography systems include the ability to post process. Over or under exposed mammograms can be corrected as image processing and image acquisition are separated. Image handling and storage is also made easier as it can be accessible on any computer with the appropriate equipment, and each mammogram does not require its own physical space.

3.4.3 Contrast Enhanced Full Field Digital mammography

Full field digital mammography developments have been rapid, leading to the development of other advanced imaging techniques⁵. Though the diagnostic accuracy of FFDM is at least equivalent to screen-film mammography⁵, there are still some limitations. Particularly in dense breast, and patients with fibrocystic disease, cancers are difficult to detect. The capability of being able to post process images has allowed for techniques that emphasize breast cancer with the use of an iodine based contrast agent: temporal subtraction, and dual-energy contrast enhanced mammography. Both imaging techniques exploit the differences between the atomic numbers of the soft tissue, and the iodinated contrast agent that accumulates in lesions

that are metabolically active. The difference in x-ray attenuation of the two regions are exploited to effectively cancel background tissue, leaving only the iodinated region.

In temporal subtraction, a radiographic image of the breast is taken prior to the injection of the iodinated contrast agent then another at the same x-ray tube energy. The presence of iodine in the post contrast image would increase contrast of the region, while attenuation of the normal tissue will remain the same as the pre-contrast image. In order to enhance the iodinated region, the pre-contrast image is subtracted from the post-contrast image. To avoid image artifacts and attain optimum image quality, the best image registration is required. As a result, imaging must be quick, using light breast compression that will allow for blood flow, while restricting motion between the pre-contrast and post-contrast image.

The dual energy contrast enhanced mammography technique exploits the differences in the energy dependence of attenuation between the breast tissue and the iodinated contrast agent⁵. For this technique, a pair of low and high-energy images are taken after administration of the iodinated contrast agent. The effective energies of the low and high-energy spectra “bracket” the k-edge of iodine, capitalizing on the sharp increase in attenuation of iodine. The low energy image is usually a standard mammographic image commonly used in mammography for the specified breast thickness. The high energy image is typically 45-49 kV, with the use of a filter to increase the mean energy of the spectrum. The low energy x-ray exposures allow for similar attenuation between the normal tissue and iodinated regions. The high energy x-rays, with mean energies above the k-edge of iodine (33 keV) cause the iodinated region to attenuate more x-rays, increasing contrast. Subtraction of the two images removes the background tissue, resulting in an image that consist primarily of the iodinated regions¹³.

3.5 Imaging quality and performance

Other than imaging performance of the system, skills and experience of the radiologist is also a determinant in the successful detection of cancers. Therefore, the performance of mammography systems are evaluated by receiver operating characteristics (ROC) curve analysis, as it assesses diagnostic abilities of different radiologist on the system, or as a means to compare two imaging modalities (for example, CT vs FFDM)¹.

In essence, the diagnostic test separates patients with normal, or abnormally suspicious breast. However, there is usually overlap of the two fields based on the decision criteria (BIRADS). Radiologist are still responsible for choosing whether the patient is normal or abnormal, and as a result, a 2 x 2 decision matrix is used to determine the accuracy of the diagnosis. Table 3.4 shows the decision matrix used in diagnosis.

Table 3.4 The decision matrix used in the diagnosis of breast cancer.

Diagnosis	Disease Truth	
	Positive	Negative
	Positive Negative	TP FN
		FP TN

TP is defined as the true positive value, which is the amount of lesions identified as cancers that proved to be cancers. The TN is the true negative value, and are lesions correctly identified as benign, and prove to be benign. FP is the false positive value, which is indicative of the amount of lesions identified as cancers that turned out to be benign, and FN is the false negative value, lesions identified as benign but are cancers³. For calculation of these parameter, the truth of the presence of disease needs to be determined independently by way of biopsy confirmation.

The values from the decision matrix can also be used to determine the sensitivity and specificity the screening. Sensitivity is the number of malignant cases that the radiologist correctly identifies as malignant, and is given by

$$Sensitivity = \frac{TP}{TP+FN} \quad (3.13)$$

Specificity is defined as the fraction of benign cases the radiologist correctly identifies as benign, and this is given by

$$Specificity = \frac{TN}{TN+FP} \quad (3.14)$$

Though heavily influenced by the incidence of disease, a measure of the overall diagnostic performance is the *accuracy*. The accuracy is defined as the ratio of the number of patients correctly diagnosed compared to the total population of patients. It is given by the equation,

$$Accuracy = \frac{TP+TN}{TP+TN+FP+FN} \quad (3.15)$$

However, accuracy is deemed a poor metric of performance and receiver operating characteristics provide a better description of the performance potential for mammography. Receiver operating characteristic (ROC) curves are derived from sensitivity and specificity. The curve is a plot of the sensitivity against (1 – specificity), and along the curve show the compromise between sensitivity and specificity¹. For comparison between readers or imaging systems, the area under the curve (AUC) is calculated and compared. In comparing imaging modalities with readers with similar ROCs, the larger AUC is indicative of an imaging system, more like to produce TP sand TNs. An example of an ROC is displayed in Figure 3.8.

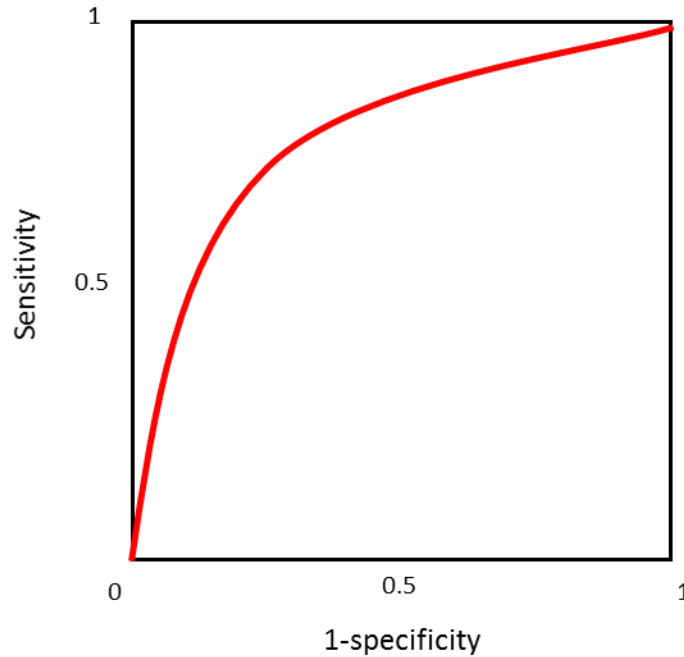


Figure 3.15 Example of an arbitrary ROC curve.

3.6 Digital Tomosynthesis

Though mammography screening has proven its effectiveness in the reduction of mortality rates with breast cancer, it has two serious inherent limitations¹⁴: low sensitivity, especially in women with dense breast parenchyma and low specificity leading to relatively high recall rates. Low sensitivity is due to the fact that normal tissue may be superimposed on a breast lesion, obscuring the cancer and leading to a high false positive rate. At times, the obscurity caused by the overlapping of tissues simulate a cancer, which leads to the low specificity. Consequently, improvement of mammographic techniques in breast cancer screening is of significant importance^{3,14}.

As mentioned previously in section 3.4.3, the development of full field digital detectors has allowed for advanced techniques in breast cancer x-ray imaging. Digital breast tomosynthesis, a quasi-3D imaging technique, was made possible by the availability of digital

detectors³. The technique is analogous to limited angle geometric tomography, in that a number of low-dose projections are acquired during rotation of the tube through a limited arc. A schematic view of the principles of tomosynthesis is shown in Figure 3.9.

Tube motion around the breast occurs in one of two manners: continuous, or step and shoot. The continuous motion involves the continuous movement of the x-ray tube along the fixed arc, while acquiring projection images at fixed points. For step-and-shoot, the x-ray tube comes to a stop at every fixed point before acquisition of the projection image. Both techniques have their advantages and disadvantages which will be discussed later.

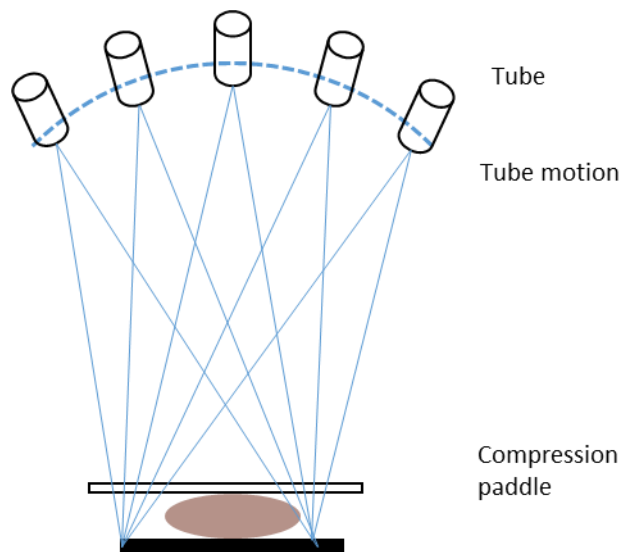


Figure 3.16 Schematic diagram of showing the principle of digital breast tomosynthesis.

What distinguishes digital breast tomosynthesis from conventional 2D mammography is the accompanying depth information with the corresponding reconstructed plane. This reduces the obscuring effect of overlapping tissue. Consequently, digital breast tomosynthesis improves lesion conspicuity compared to 2D mammography, improving sensitivity in mammographic

screening. Several retrospective studies have reported increased cancer detection rates when DBT is used in conjunction with full field digital mammography¹⁴.

There are currently two FDA approved tomosynthesis devices. The Hologic Selenia Dimension DBT, and GE SenoClaire DBT systems were FDA approved in 2011 and 2014 respectively. FDA approval only permits the use of DBT with standard FFDM as recall rates have significantly decreased when used together¹⁵. The Hologic system employs continuous motion, while the GE system utilizes step-and-shoot.

3.7 REFERENCES

- ¹ J.T. Bushberg, J.A. Seibert, E.M. Leidholdt, J.M. Boone, and M. Mahesh, *Med. Phys.* **40**, 077301 (2013).
- ² D. Ikeda, *Breast Imaging : The Requisites*, 2nd ed. (Elsevier/Mosby, St. Louis, Mo., 2011).
- ³ D.B. Kopans, *Breast Imaging* (Lippincott Williams & Wilkins, 2007).
- ⁴ M. Shetty, 458 (2015).
- ⁵ E.D. Pisano and M. Yaffe, *Digital Mammography*. (1998).
- ⁶ L. Lança and A. Silva, *Digit. Imaging Syst. Plain Radiogr.* **9781461450**, 1 (2013).
- ⁷ J. a Baker and E. Floyd, *AJR Am J Roentgenol* **166**, 773 (1996).
- ⁸ R. Bott, *Igarss* 2014 1 (2014).
- ⁹ A.C. of R. 2013 D’Orsi CJ, Sickled’Orsi CJ, Sickles EA, Mendelson EB, Morris EA et al. *ACR BI-RADS® Atlas, Breast Imaging Reporting and Data System*. Reston, VA, American College of Radiology; 2013s EA, Mendelson EB, Morris EA et al. *ACR BI-RADS® Atlas, Breast Imaging Rep*, 6 (n.d.).
- ¹⁰ W.R. Hendee and E.R. Ritenour, *Medical Imaging Physics* (Wiley-Liss, 2002).
- ¹¹ J.L. Prince and J.M. Links, *Medical Imaging Signals and Systems* (Pearson Prentice Hall, Upper Saddle River, New Jersey, 2006).
- ¹² E. Kotter and M. Langer, *Eur. Radiol.* **12**, 2562 (2002).
- ¹³ A. Smith and D. Ph, (n.d.).
- ¹⁴ F.J. Gilbert, K.C. Young, S.M. Astley, P. Whelehan, and M.G.C. Gillan, *Digital Breast Tomosynthesis* (2010).

¹⁵ A.W. Tucker, Y.Z. Lee, C.M. Kuzmiak, J. Calliste, J. Lu, and O. Zhou, in *SPIE Med. Imaging*, edited by B.R. Whiting and C. Hoeschen (International Society for Optics and Photonics, 2014), p. 903316.

CHAPTER 4: Carbon Nanotube X-ray Sources

4.1 Carbon Nanotubes

Many interesting and unique properties are afforded by the many graphitic structures that can be formed from the sp^2 hybridization of carbon. The tubular form of carbon structures was first reported in 1991 by Sumio Iijima, and further engendered interest and research¹. Carbon nanotubes (CNTs) are hollow, made up of one or more graphene cylinders, coaxially arranged, with diameters ranging from 4 to 30 nm in diameter^{1,2}. Initial synthesis of CNTs were done using a direct current arc-discharge process, similar to the techniques used in producing fullerene molecules. However, synthesis techniques such as chemical vapor deposition, and laser ablation, have since been used in CNT production.

4.1.1 Structure of CNTs

CNTs have unique structures that lead to unique properties of interest that are still being explored today². It is necessary to have an understanding of the structure of CNTs to appreciate its unique properties. CNTs are classified into two groups based on the number of graphene sheets (or layers) in their structure. CNTs with one layer are referred to as single-walled nanotubes (SWNTs), and with more than one layer, multi-walled nanotubes (MWNTs). Since MWNTs are essentially multiple coaxial SWNTs, for simplification we can consider the SWNT.

The single layer of graphene that constitutes the CNT is rolled into a seamless cylinder, with diameters ranging from 0.4 to 3 nm, and up to 1 μm in length^{1,2}. Their characteristics are determined on the graphene layer assembly, as it determines tube diameter and angular

orientation to the nanotube axis. The structure of a CNT is defined using a vector that connects two lattice points in the graphene sheet helical structure (see Figure 4.1)³.

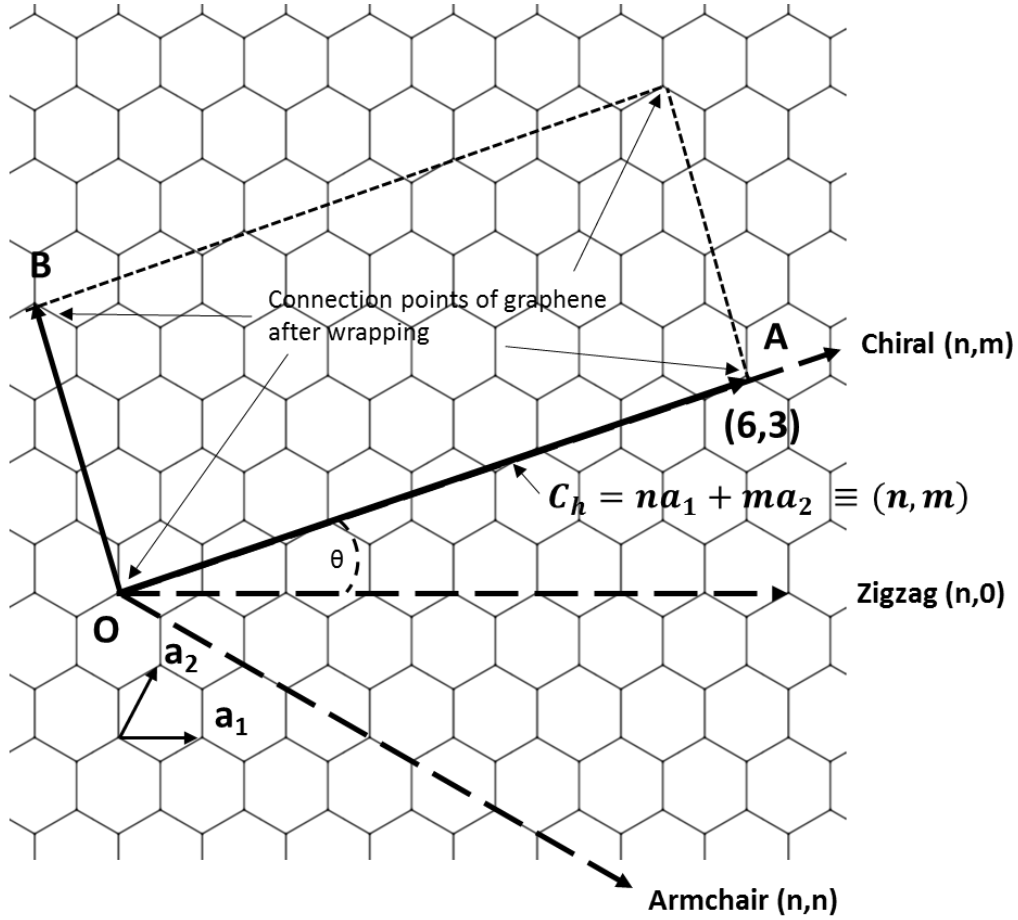


Figure 4.17 Shows a graphene sheet with chiral vectors depicting the types of CNT structures produced.

The vector represents the tube diameter when the graphene sheet is rolled, connecting the two crystallographic equivalent points^{3,4}. This vector is defined as the chiral vector, and it characterizes a CNT. The equation for the chiral vector is given by:

$$C_h = na_1 + ma_2 \equiv (n, m) \quad (4.16)$$

Where n and m are integers with $0 \leq |m| \leq n$, used to denote the number of unit vectors, a_1 and a_2 that compose the chiral vector^{1,3,5}. They are referred to as the chiral indices and are used

to specify the structure of SWNTs. The angle formed between the chiral vectors and the zigzag direction is known as the chiral angle. There are three different types of SWNTs, armchair, zigzag and chiral. Armchair CNTs have chiral angles θ and indices equal to 30° and $n = m \neq 0$ respectively, zigzag if $\theta = 0$ and indices $m = 0, n \neq 0$, and chiral if $0^\circ < \theta < 30^\circ$ ^{3,4,6}. Illustrations of the three types of SWNTs are in Figure 4.2.

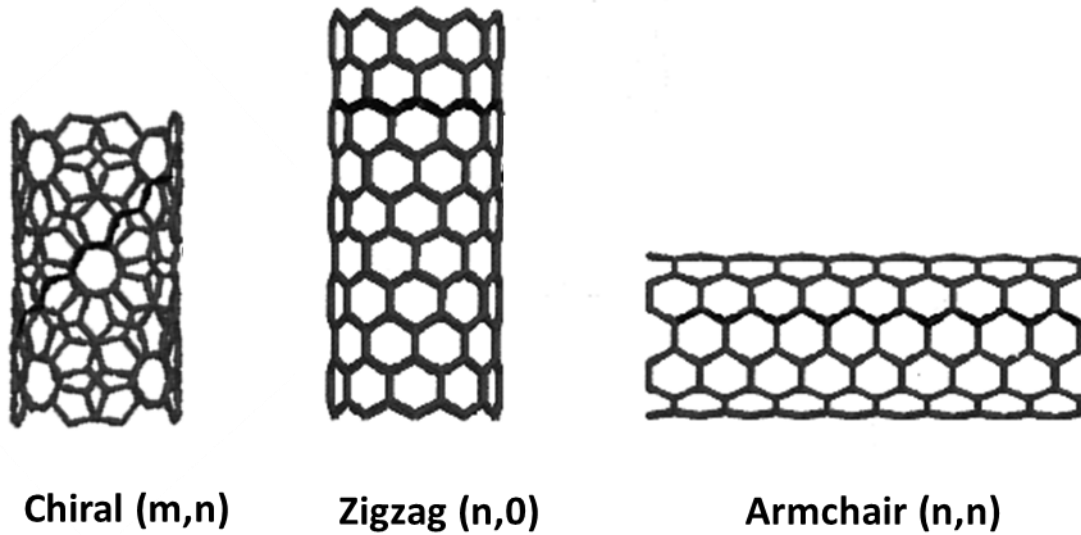


Figure 4.18 A representation of the three types of SWNT produced from the “rolling” of graphene sheets.

As previously mentioned, MWNTs contain multiple SWNTs concentrically arranged. The number of sheets usually range from 4 – 20, with interlayer spacing ranging from 0.33 nm – 0.344 nm³. Diameters range from 4 – 50 nm, with lengths exceeding 10 μm ^{2,3}. The electronic properties of individual CNTs are determined by their chiral indices, and they can be conducting and semiconducting. Of the SWNTs, the chiral tubes tend to be semiconducting while the armchair and zigzag tend to be conducting. MWNT tend to be semimetallic⁷. Several unique properties make CNT ideal candidates for field emission, namely (i) high thermal and electrical conductivity at room temperatures, (ii) high aspect ratios, (iii) high chemical and mechanical

stability at high temperatures, and (iv) the ideal whisker-like shape with sharp tip for field emission⁷.

4.2 Carbon nanotube field emission

4.2.1 Field Emission Theory

The field emission effect was first discovered by Ralph H. Fowler and Lothar Wolfgang Nordheim in 1928⁸. Field emission is the process whereby electrons tunnel through a barrier in the presence of a high electric field ($10^7 - 10^8$ V/cm), due to quantum mechanical effects^{8,9}. Since electrons are emitted by the application of an electric field instead of heating up the material, it is also referred to as “cold electron emission”. As illustrated in Figure 4.3, the external electric field lowers the effective work function, allowing the electrons near the Fermi surface with sufficient energy to tunnel through the potential barrier. The emission current density produced from the field emission is given by the Fowler-Nordheim equation:

$$J = \frac{aF_e^2}{\phi} e^{\frac{-b\phi^{3/2}}{F_e}} \quad (4.17)$$

Where J is the current density in A/cm^2 , a and b are constants with respective values of $1.54 \times 10^{-6} \text{ A}\cdot\text{eV}\cdot\text{V}^{-2}$ and $6.83 \times 10^7 \text{ eV}^{3/2} \text{ Vcm}^{-1}$, ϕ is the work function of the material, and F_e is the calculated enhanced field¹⁰. From the equation it can be deduced that current is only dependent on the applied electric field.

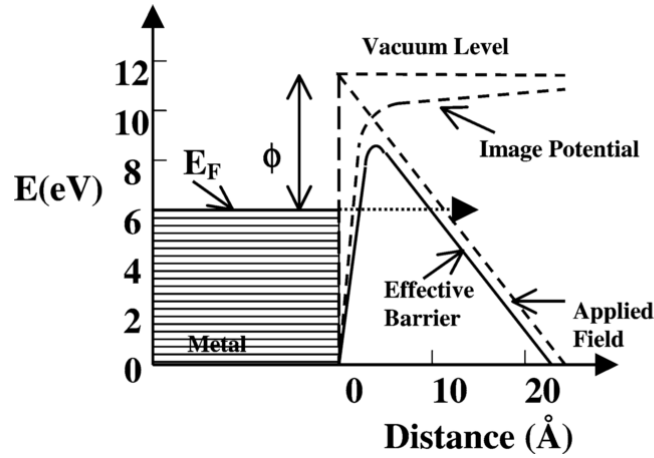


Figure 4.19 Diagram of the field emission effect. The effective barrier is lowered by the electric field so that electrons near the Fermi level can tunnel through the barrier¹¹.

Due to the high aspect ratios, and needle like tips of CNTs, the electric field at the tips far exceed the mean value of this parameter¹². As a result, CNTs have high electric field enhancement factors, which enhance the electric field making it possible to achieve high emission currents^{12,11}. The enhanced field, F_e , from Equation 4.1 is given by:

$$F_e = \beta F \quad (4.18)$$

where β is the electric field enhancement, and F is the electric field V/m. The field enhancement factor is most influential in the performance of CNT based cathodes. Compared to conventional field emission field emitters, CNTs function at relatively low voltages, allowing them to be used in miniature devices for a number of applications. Main applications of CNTs include, flat-panel field emission display, transparent conductive thin films, electron sources for electron microscopes, and x-ray sources to name a few⁶.

4.2.2 CNT X-ray sources

The basic design of the x-ray tube has remained changed in the last century. Since CNT field emission is a better alternative to thermionic emission due to the emission of electrons at

room temperature, compared to thermionic emission that requires heating of the cathode to high temperatures, CNTs are ideal candidates for cathodes in x-ray tubes¹¹. However, there are conditions that need to be satisfied for the stable operation of CNT cathodes, that determine its I-V characteristics¹². Over a decade ago, our lab reported the optimization of the morphology of CNT films capable of producing high, and stable current emission. The cathodes were constructed with purified SWNT bundles produced via laser ablation¹³. The SWNTs have an average diameter of 1.4 nm and an average bundle size of 50 nm. Presently, all CNT x-ray tubes cathodes are constructed using these SWNT in a triode type design¹³. Components of the CNT x-ray tube include one or an array of CNT cathodes, gate electrode, focusing electrodes, and anodes under a steady state vacuum around 10^{-10} torr. A schematic diagram of a CNT based x-ray source is shown in Figure 4.4.

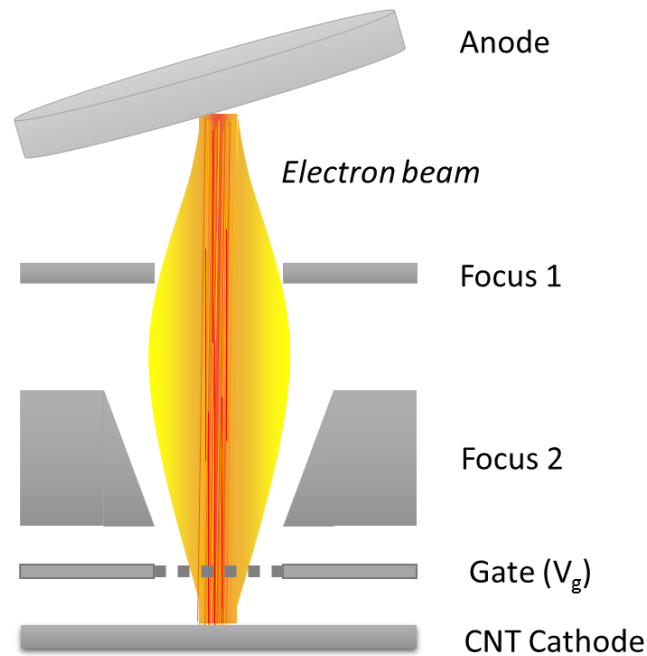


Figure 4.20 Diagram of typical CNT source design. The source consist of a CNT cathode, gate mesh, focusing electrodes and an anode. A small voltage is applied across the gate mesh and the cathode, while a large voltage is applied to the anode.

The CNTs are electrophoretically deposited onto a molybdenum substrate by methods developed in our lab¹⁴. Areas of CNT deposition is dependent on the application of the x-ray tube. Above the cathode is the gate mesh, constructed of tungsten bars. Voltages (Gate-cathode, V_{gc}) can be applied either to the cathode or gate while the other is grounded, on the order of 1000 – 2000 V. Focusing electrodes are placed above the gate, and are used to control the size of the desired focal spot by application a negative or positive voltage¹⁵. Anodes in CNT x-ray tubes are made of tungsten, and are angled at 16° ¹⁵. Large DC voltages ranging from 30 kVp to 160 kVp are applied to the anode depending on the imaging or therapy application. Because of the triode design in the CNT x-ray tubes, the anode current is less than current emitted from the cathode. The ratio of the tube current to the cathode current is known as the transmission rate. For CNT x-ray sources, usual transmission rates are about 60% to 70%^{15–17}. Maximum tube current is limited to the heat capacity of the anode, and is calculated by the maximum power divided by the anode voltage. High tube currents allow for short x-ray pulses, which is beneficial in diagnostic imaging. High voltage feedthroughs and CNT source spacing is designed to prevent arcing in the tube. The focal spot size of CNT sources is dependent on electric field distribution between the gate through to the anode, and are of paramount importance in determining the system's spatial resolution¹⁵.

4.3 CNT X-Ray source applications

The compact design, flexibility of cathode shape, and the instantaneous triggering of x-ray sources give CNT x-ray sources unique advantages over thermionic x-ray sources. These advantages can be exploited to further improve upon current x-ray system for medical and industrial applications. Current applications of x-ray sources include: micro beam radiation therapy (MRT), micro-CT, and stationary digital chest tomosynthesis (s-DCT). This section

briefly describes each of these developed systems from our lab, and a summary of their respective results.

4.3.1 MRT

Micro-beam radiation therapy is a novel form of radio therapy based on spatial fractionation of planar x-ray beams^{18,19}. The spatial fractionation of x-ray beams reduce the damage of normal tissue, while disrupting cancerous tissue, even at high peak doses¹⁹. This method was first developed at synchrotron facilities by Slatkin et al, and is being investigated in the treatment of tumors in small animals, with convincing evidence that normal tissue is preserved while suppression of the tumor growth is achieved^{18,19}. The widths range from 20 nm to a few microns with spacing several times the width of the beam, creating unique dose profiles with high peak to valley dose ratios¹⁹. Adequately high PVDRs are achieved by using orthovoltages, and collimators with narrow openings. High voltages are required as the collimation greatly reduces the dose rate of the x-ray beam, which is difficult to achieve using current commercially available x-ray sources. As a result, MRT research has been studied at synchrotron facilities, which are limited^{18,20}.

Utilizing CNT x-ray sources to create multiple long narrow focal spots (line-focused x-ray source), Hadsell et al. developed a desktop MRT system capable of delivering high microbeam dose rates, for treatment of tumor bearing small animals²⁰. The system is capable of achieving dose rates of 2 Gy/s with line widths of 300 nm²⁰. The MRT system has previously demonstrated MRT dose distributions in both phantoms and live mice^{18,20}. Figure __ shows the MRT system over at our lab in UNC, and the histology of the mouse brain highlighting the therapeutic effect of the micro-beam.

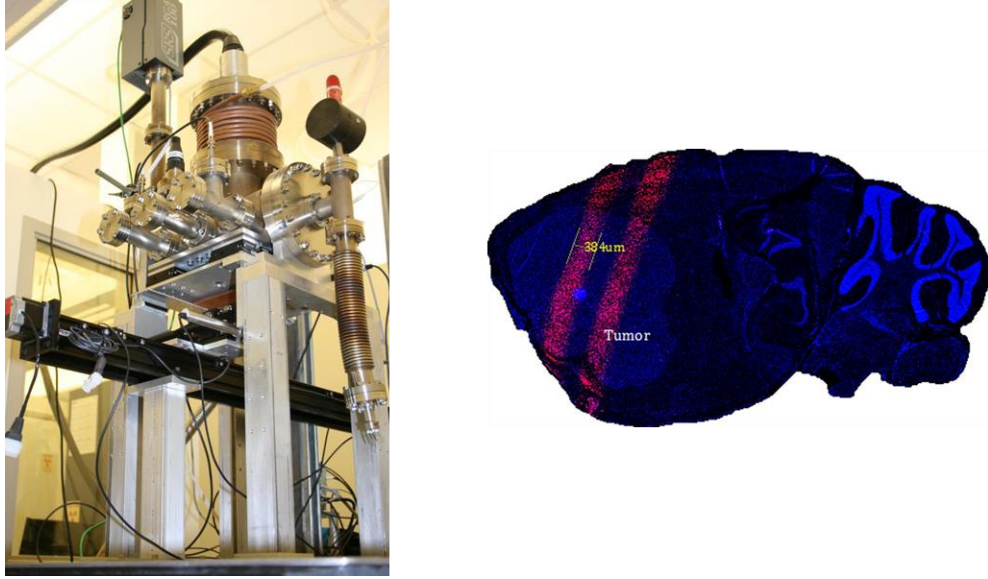


Figure 4.21 (a) Image of the desktop MRT system. (b) A histological slice of a mouse brain showing paths of irradiation^{18,20}.

4.3.2 Micro-CT

Micro-computed tomography is an *ex vivo* imaging modality used in the imaging of small animals in pre-clinical cancer studies^{21,22}. Commercial micro-CT systems presently available have very high spatial resolution, however *in vivo* imaging is challenging due to the faster respiratory motions of smaller animals than humans²¹. Motion during imaging causes motion artifacts which degrades the systems spatial resolution. Techniques that can be employed include gating of the x-ray source to a periodic cycle, and retrospective gating. Gating with thermionic sources are impractical due to their slow switch on/off times. Retrospective gating results in excessive radiation, that may affect the outcome of long term studies²².

Using CNT x-ray sources, a micro-CT system capable of cardiac and respiratory gating imaging was developed at UNC. Respiratory and cardiac cycles are captured using sensors, instantaneously triggering x-ray sources during specific periods of the cycle. Figure 4.6 has an

image of a micro-CT device with CNT x-ray sources, and reconstructed images of a mouse gated to both cardiac and respiration cycles²².

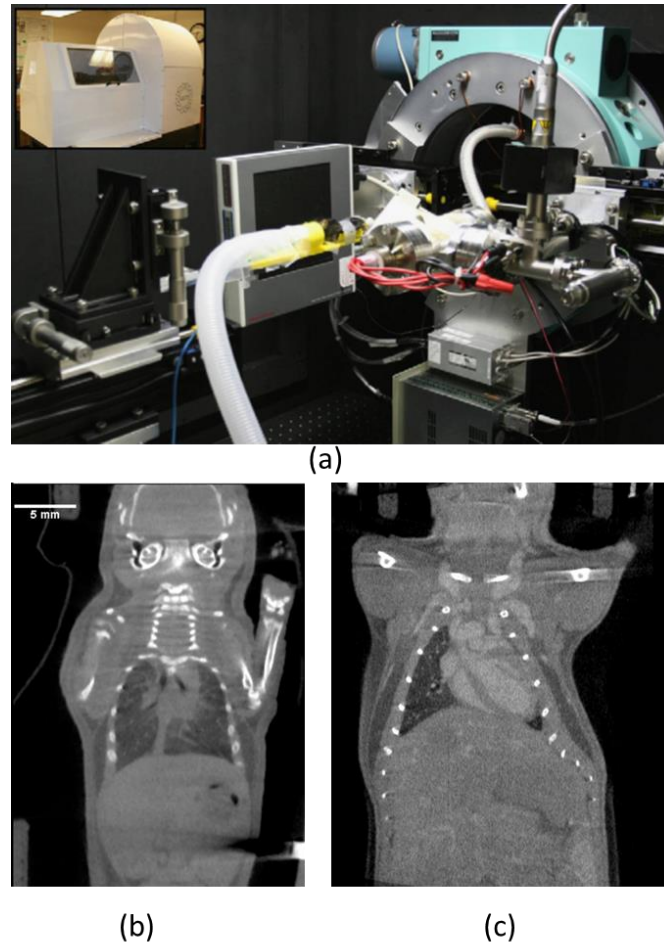
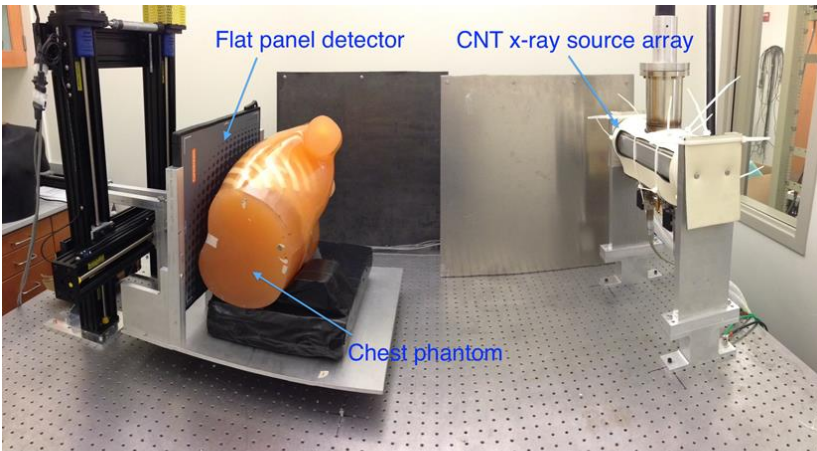


Figure 4.22 (a) Image showing the setup of the micro-CT system, the inset image shows the system covered and shielded. (b) A reconstructed slice of micro-CT mouse image gated to its respiration cycle, and (c) gated to cardiac cycle²².

4.3.3 s-DCT

Though chest computed tomography (CT) has been shown to be the most effective in the diagnosis of chest diseases, it is costly and involves high patient dose, which makes it not practicable for screening purposes. Alternatively, chest radiography is a 2D imaging modality, with low sensitivity due to the superimposition of tissue. Chest tomosynthesis has been an

emerging modality for the early detection in lung cancer screening. It has shown to be more sensitive in the detection of long nodules than 2D imaging, with significantly less dose than CT²³. In current chest tomosynthesis system, a single thermionic source is traversed through an arc of fixed angle during the acquisition of projection images. As a result, source motion reduces the system spatial resolution due to focal spot blurring. In addition, scan times are relatively long, leading to patient motion which further degrades image quality. Utilizing stationary x-ray sources will allow for rapid image acquisition, with focal spot blurring since there is no motion of the x-ray tube. Figure 4.6 (a) is an image of the stationary digital chest tomosynthesis prototype system developed by Shan et al^{23,24}. Studies on this system showed the feasibility of this system using phantoms, producing tomosynthesis images without focal spot blurring, and with adequate entrance dosage. Figure (b) is a reconstructed slice of an anthropomorphic phantom images with s-DCT system.



(a)



(b)

Figure 4.23 (a) Laboratory setup of the bench top s-DCT system. (b) Reconstructed slice of an anthropomorphic phantom images with the s-DCT system²³.

4.4 REFERENCES

- ¹ S. Iijima, *Nature* **354**, 56 (1991).
- ² S. Iijima, *Phys. B Condens. Matter* **323**, 1 (2002).
- ³ Y. Saito, *Carbon Nanotube and Related Field Emitters* (2010).
- ⁴ R. Smalley, M. Dresselhaus, and G. Dresselhaus, *Carbon Nanotubes: Synthesis, Structure, Properties, and Applications* (2003).
- ⁵ S. Iijima and T. Ichihashi, *Nature* **363**, 603 (1993).
- ⁶ M.H.M.O. Hamanaka, V.P. Mammana, and P.J. Tatsch, *Review of Field Emission from Carbon Nanotubes: Highlighting Measuring Energy Spread* (2013).
- ⁷ W.I. Milne, K.B.K. Teo, G.A.J. Amaratunga, P. Legagneux, L. Gangloff, J. Schnell, V. Semet, V. Thien, and O. Groening, 933 (2004).
- ⁸ R. Gomer, *Surf. Sci.* **299-300**, 129 (1994).
- ⁹ G. Fursey, *Field Emission in Vacuum Microelectronics* (2015).
- ¹⁰ A. Kyrtsakis and J.P. Xanthakis, (2015).
- ¹¹ Y. Cheng and O. Zhou, *Comptes Rendus Phys.* **4**, 1021 (2003).
- ¹² M.D. Bel'skii, G.S. Bocharov, a. V. Eletsii, and T.J. Sommerer, *Tech. Phys.* **55**, 289 (2010).
- ¹³ G.Z. Yue, Q. Qiu, B. Gao, Y. Cheng, J. Zhang, H. Shimoda, S. Chang, J.P. Lu, and O. Zhou, *Appl. Phys. Lett.* **81**, 355 (2002).
- ¹⁴ B. Gao, G.Z. Yue, Q. Qiu, Y. Cheng, H. Shimoda, and L. Fleming, *Adv. Mater.* **13**, 1770 (2001).
- ¹⁵ S. Sultana, X. Calderón-Colón, G. Cao, O. Zhou, and J. Lu, *Proc. SPIE* **7622**, 76225G (2010).

- ¹⁶ X. Qian, R. Rajaram, X. Calderon-Colon, G. Yang, T. Phan, D.S. Lalush, J. Lu, and O. Zhou, *Med. Phys.* **36**, 4389 (2009).
- ¹⁷ X. Qian, A. Tucker, E. Gidcumb, J. Shan, G. Yang, X. Calderon-Colon, S. Sultana, J. Lu, O. Zhou, D. Spronk, F. Sprenger, Y. Zhang, D. Kennedy, T. Farbizio, and Z. Jing, *Med. Phys.* **39**, 2090 (2012).
- ¹⁸ L. Zhang, H. Yuan, C. Inscoe, P. Chtcheprov, M. Hadsell, Y. Lee, J. Lu, S. Chang, and O. Zhou, *Expert Rev. Anticancer Ther.* **14**, 1411 (2014).
- ¹⁹ M.A. Grotzer, E. Schültke, E. Bräuer-Krisch, and J.A. Laissue, *Phys. Medica* **31**, 564 (2015).
- ²⁰ M. Hadsell, J. Zhang, P. Laganis, F. Sprenger, J. Shan, L. Zhang, L. Burk, H. Yuan, S. Chang, J. Lu, and O. Zhou, *Appl. Phys. Lett.* **103**, (2013).
- ²¹ G. Cao, Y.Z. Lee, R. Peng, Z. Liu, R. Rajaram, X. Calderon-Colon, L. An, P. Wang, T. Phan, S. Sultana, D.S. Lalush, J.P. Lu, and O. Zhou, *Phys. Med. Biol.* **54**, 2323 (2009).
- ²² Y.Z. Lee, L. Burk, K.-H. Wang, G. Cao, J. Lu, and O. Zhou, *Nucl. Instrum. Methods Phys. Res. A.* **648**, S281 (2011).
- ²³ J. Shan, P. Chtcheprov, A.W. Tucker, Y.Z. Lee, X. Wang, D. Foos, M.D. Heath, J. Lu, and O. Zhou, *Station. Chest Tomosynthesis Using a CNT X-Ray Source Array* **81**, 86680E (2013).
- ²⁴ J. Shan, P. Chtcheprov, A.W. Tucker, Y.Z. Lee, X. Wang, D. Foos, M.D. Heath, J. Lu, and O. Zhou, *Station. Chest Tomosynthesis Using a CNT X-Ray Source Array* **81**, 86680E (2013).

CHAPTER 5: Stationary Digital Breast Tomosynthesis

5.1 Motivation for a stationary digital breast tomosynthesis system

5.1.1 Limitations of current DBT systems

As mentioned in Chapter 3.3, current DBT scanners are based on FFDM systems, requiring a single x-ray source that traverses the angular span to collect projection images at different angular increments. The motion of the x-ray source either occurs in a continuous motion (CM) or a step-and-shoot motion (SSM). Continuous motion involves the simultaneous acquisition of projection images during tube motion, whereas the step and shoot motion involves a momentary pause during the acquisition of the projection image¹. The mechanical motion of the x-ray source introduces two main limitations of the current DBT systems: focal spot blurring and long scan times². The continuous gantry movement and mechanical instability due to the acceleration and deceleration of the x-ray tube causes blurring of the focal spot, consequently increasing its size. Accordingly, this reduces the spatial resolution of the system. Also, since the x-ray tube has to move through the distance of the angular span, DBT scanning times are long with respect to FFDM. Long scan times allow for sufficient patient motion during image acquisition which further compromises image quality. This degradation in image quality results in an unfavorable decrease in the sensitivity for small microcalcifications (MC) compared to FFDM. MC visibility plays a crucial role in determination of malignancy of lesions in breast cancer diagnosis³. The decreased visibility of MCs moving from FFDM to DBT is the governing reason as to why DBT systems have to be used in conjunction with FFDM, or the s-DBT system has to have the capability for synthetic 2D imaging^{1,4-6}. Patients imaged with both modalities

receive more than double the mammography dose, which may be of concern with regard to radiation protection, especially in the screening population.

These two main limitations are interconnected to each other, and the improvement of one is counterproductive to the other. For example, the focal spot blurring can be decreased by decreasing the rate at which the source moves, however, this increases imaging time. Increasing the imaging time leads to additional patient motion, and degradation in image quality. Conversely, imaging time can be reduced by increasing the rate at which the x-ray source moves, but that increases the focal spot blurring, further degrading the system spatial resolution.

5.1.2 Proposed solution and advantages of s-DBT

As a means to overcome the limitations caused by the mechanical motion of the x-ray source, novel designs have previously been explored and tested. One design that seemed promising was the design of a multiple thermionic x-ray source array^{7,8}. However, due to the complexity of design and control of the individual thermionic x-ray sources, it was deemed impractical and not suitable for clinical applications. As previously discussed, CNT x-ray sources allow for compact, unique designs, which can be switched on instantaneously. Therefore, the basis of s-DBT is to use a linearly distributed array of CNT x-ray sources, to take the angular projection images eliminating mechanical motion of the x-ray tube. Since there is no mechanical motion, the linear CNT x-ray source array overcomes focal spot blurring, improving the spatial resolution of the DBT system. In addition, the electronic controlling of the CNT sources can potentially shorten the acquisition time of a DBT data set provided there is sufficient tube flux. The decrease in DBT acquisition time is continuously desirable as it decreases the amount of patient motion, further removing image blur. Another unique advantage of implementing multiple stationary sources is the independence of the imaging time to the angular span for the

projection images. Increasing the angular span, without compromising imaging time, would also increase the overall system resolution. The overall increase in DBT system resolution by employing a stationary source should increase the quality of the 3D images, further increasing the visibility of masses and more importantly, microcalcifications.

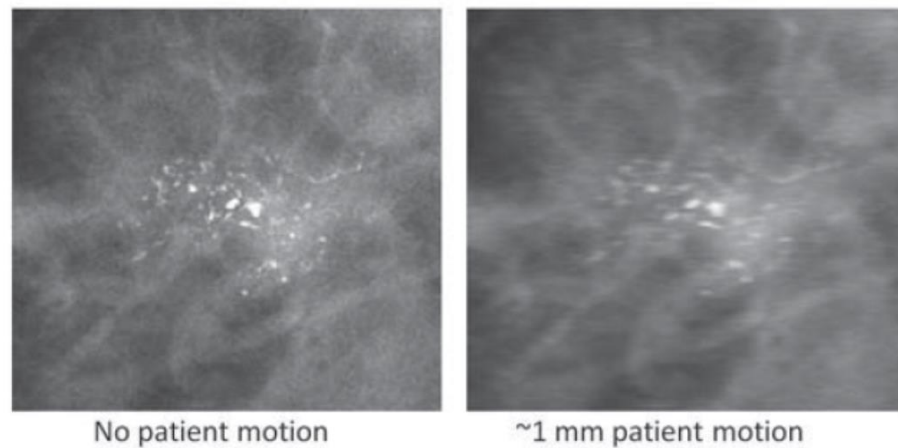


Figure 5.24 Effect of patient motion on visibility of microcalcifications. Attribution: © Andrew Smith⁹.

5.2 First generation stationary digital breast tomosynthesis system

The first generation s-DBT system is the current iteration of s-DBT systems that we have designed and optimized, the system is capable of human imaging. The system is based on the development of two prior prototype s-DBT systems that are not discussed in this thesis. By using industry standard phantoms, and human specimen imaging, this system has shown increased spatial resolution over the only FDA approved continuous motion DBT (CM-DBT) system. The first generation system is currently undergoing the first-ever clinical trial using CNT stationary x-ray source arrays for human imaging at the University of North Carolina Cancer Hospital.

5.2.1 CNT x-ray source array

This CNT x-ray source array (XinRay System Inc., Research Triangle Park, NC) comprises of 31 x-ray sources assembled linearly encased in a stainless steel housing, and a 1

mm thick aluminum window (Al). The Al window acts as a vacuum barrier, and also an inherent beam filter for the x-ray tube. Two ion pumps used to maintain a tube pressure at or lower than 10^{-7} torr are connected to the ends of the tube as seen in Figure 5.2. An external collimator is attached outside of the x-ray tube window to provide sufficient elimination of x-rays outside of the image receptor, and prevent unnecessary patient exposure. The 31 sources are distributed along 370 mm, with an equiangular spacing of 1 degree from the iso-center of the system. Each of the 31 sources consists of a CNT cathode, a grounded gate, focusing electrodes, and a tungsten anode. For field emission from the cathodes, a negative voltage is applied to the cathode, usually within the range 1 kV – 2 kV. Synonymous to conventional x-ray tubes, a positive high voltage is applied to the anode to accelerate the electrons for bombardment and x-ray production.

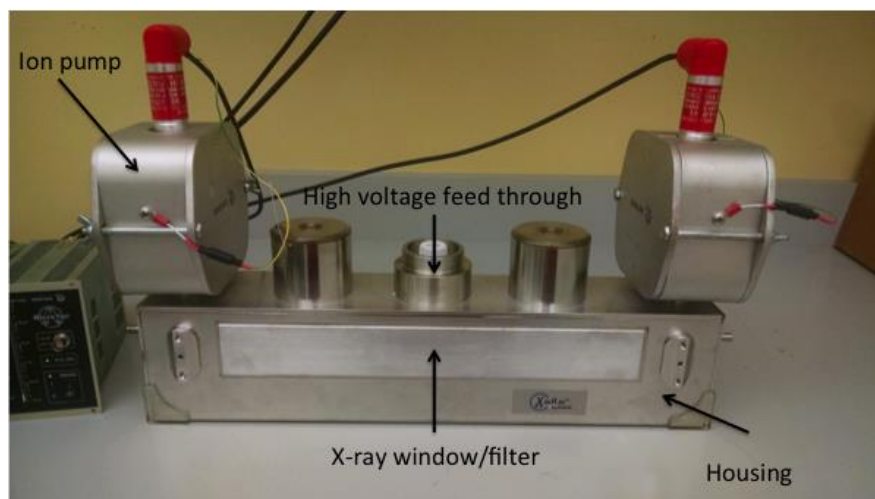


Figure 5.25 Photo of s-DBT tube with the key components labelled.

The tube is designed and conditioned to 45 kVp anode potential, however operation of this tube does not exceed 40 kVp. Due to current anode thermal restrictions, cathode current does not exceed 43 mA. The required average gate-cathode voltage for the 31 individual sources is 1.4

kV. The transmission rate, defined as the ratio of tube current to emitted cathode current as in conventional thermionic tubes, is approximately 61% for each of the 31 sources. The average focal spot size for each source was 0.64 ± 0.04 mm width, and 0.61 ± 0.05 mm length. System MTF was measured at approximately 4 cycle/mm, indicative of a 33% increase in in-plane resolution over the Hologic Selenia Dimensions DBT system¹⁰.

5.2.2 System Description / Assembly and Integration

The first generation s-DBT system was constructed by replacing the single thermionic x-ray source from the Selenia Dimension DBT system (Hologic Inc., Bedford, MA with the CNT x-ray source array described in the previous section. In keeping the design of the s-DBT system similar to the Hologic DBT system, the SID was the same at 70 cm, with the source array parallel to the surface of the detector. This SID results in an angular coverage of 30 degrees with a 1 degree separation between the focal spots relative to the iso-center, which is 4 cm above the detector surface. The system geometry is shown in Figure 5.3, and the geometry of the s-DBT system is shown in Table 5.1.

Table 5.5 The specifications of the first generation system.

No. of views	Up to 31
Angular range	Up to 30°
Detector FOV	24 x 29 cm
Source to detector distance	700 mm
Angular spacing between sources	1°
X-ray anode	Tungsten
Anode tilt angle	16°
X-ray window	1 mm Al
Anode voltage	Up to 45 kVp
Tube current	Up to 38 mA
Focal spot size (FWHM)	0.60 x 0.61 mm

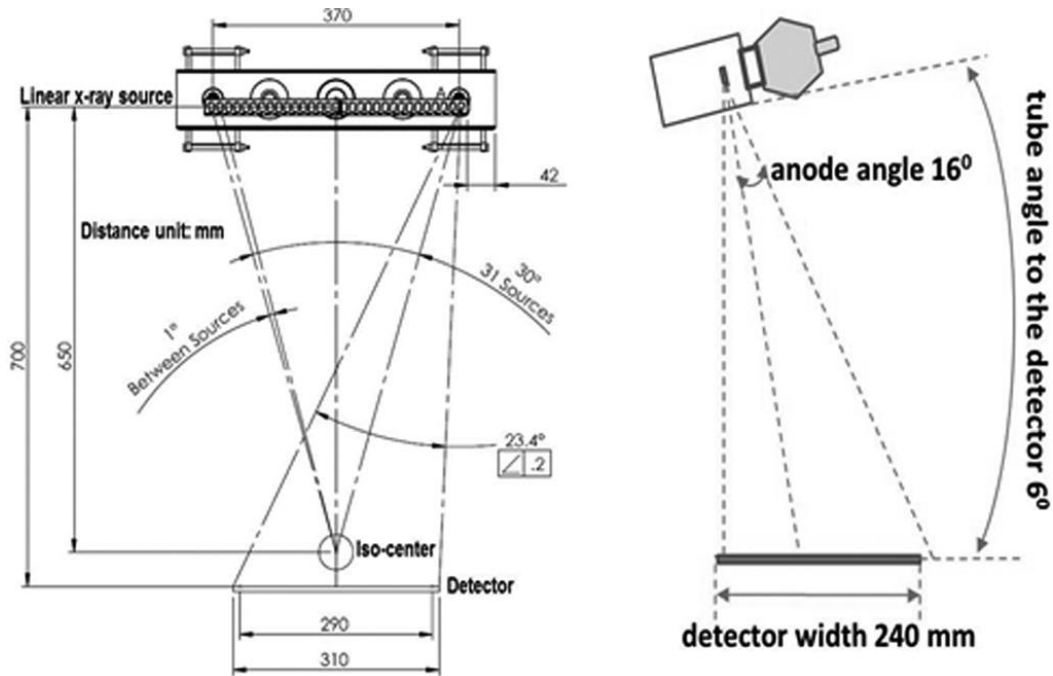


Figure 5.26. System geometry of the first generation stationary digital breast tomosynthesis system with the CNT x-ray source array.

For system operation, the CNT x-ray source array was electronically integrated into Selenia Dimensions system gantry that houses an amorphous selenium (a-Si) detector. The detector has a 24 x 29 cm field of view, and is capable of operation in a 2 x 2 binning mode (140 μm pixel size) and full resolution mode (70 μm pixel size). To synchronize the detector integration and readout times with the x-ray source exposure, a custom built electronic control system (ECS) (H&P Advanced Technology., Erlangen, Germany) is used. The ECS is capable of supplying up to 3.1 kV to each cathode, with current pulses ranging from 10 ms to 250 ms. A custom built electronic box supplied by Hologic provides the necessary transistor-transistor logic (TTL) signals from the detector to the ECS for triggering the x-ray source exposure and desired sequence. The gate-cathode extraction voltage required for the programmed emission current from each source is also regulated by the ECS.

All system components are controlled remotely via software written mainly in LabVIEW, and allows for operating via the Selenia Dimensions control console.

5.2.3 System performance and optimization

The CNT x-ray source array characteristics and the s-DBT system acquisition geometry characterizes the stationary tomosynthesis system. System performance was evaluated upon completion of system construction. The in-plane (x-y) and depth (z) resolution of the system was measured by the modulation transfer function (MTF), and artifact spread function (ASF) respectively.

Previous studies have indicated that the optimal image quality of a DBT system is dependent on a number of system configuration parameters¹¹⁻¹³. For a fixed angular span, there is an optimal number of projection images that would produce the best image quality, of course keeping patient dose to acceptable standards as defined by MQSA. The dependence of the image quality on the system configuration parameters were investigated by Tucker et al.¹⁴, and is covered in this section.

In tomosynthesis, the limited number of projection views coupled with the limited angular span results in unavoidable image artifacts that arise from blurring of objects in out of focus planes¹⁵. A DBT system's ability to resolve objects in the direction perpendicular to the detector plane (z-axis) is referred to as the system's depth resolution. The artifact spread function (ASF), used to quantify system depth resolution, measures the degree to which blurring of objects in out of focus planes occur. The ASF is defined as the ratio between the contrast of an object out of the focus plane, to that of the respective object in the focal plane^{15,16}. For the ASF measurement of the 1st generation system, the American College of Radiology (ACR) mammography accreditation phantom (CIRS Model 015) was imaged using 15 projections over

either 14° or 28°, and 29 projections over a 28° angular span with both equal and unequal dose distribution (see Table 5.2). Using the set of six largest aluminum oxide specks (0.54 mm diameter) in the ACR phantom used to simulate MCs, the ASF was calculated for each configuration parameter. Calculation of the ASF at the focal different slices away from the focal plane is given by:

$$ASF(z) = \frac{\max[\mu_{mc}(z)] - \mu_{bkg}(z)}{\mu_{bkg}(z)} \quad (5.19)$$

Where the “ $\max[\mu_{mc}(z)]$ ” is the maximum pixel value of the region of interest (ROI) for the slice located at z , and $\mu_{bkg}(z)$ is the average value of the background pixels of the ROI for the slice. ASF was plotted as a function of distance from the focal plane and the data was then fitted to a Gaussian curve. The full width half maximum (FWHM) of the fitted Gaussian ASF was used as the measure of z -axis resolution¹⁷. As seen in Table 5.2, the angular span is the dominating factor of the ASF. A significant reduction in the ASF is observed from 14° to 28° keeping the number of projections constant, whereas no significant change is observed by changing entrance dose, dose distribution, or detector pixel size. Figure 5.4 shows the measured ASF for the s-DBT system for 14° and 28° angular span using the same entrance dose and number of projections. As illustrated in the figure, there is an approximate 50% reduction in the FWHM of the ASF moving from 14° to 28° angular coverage.

Table 5. 6 The calculated results for SdNR, FWHM of the ASF, and MTF. The data is separated into the five groups of configurations. MMOC stands for more mAs on central projections. LMOC stands for less mAs on central projections. The 29 projection view, and 28° angular span, with an even dose distribution resulted in the highest quality factor value for an exposure of 100 mAs. Reprinted with permission from Tucker et al., Med. Phys., 40, 031917-8, (2013). Copyright 2013, American Association of Physicists in Medicine.

Group	Number of Projections	Total angular span	Entrance dose	Detect or Resolution	mAs distribution	SdNR	FWHM of ASF	MTF at 10%	QF
1	15	14°	727	140	Uniform	5.72 ± 0.21	7.8	4.14 ± 0.01	0.85
1	15	28°	682	140	Uniform	5.44 ± 0.20	4.08	4.20 ± 0.03	1
2	15	28°	682	140	Uniform	5.44 ± 0.20	4.08	4.20 ± 0.03	1
2	29	28°	656	140	Uniform	5.81 ± 0.16	4.1	4.25 ± 0.02	1.02
3	29	28°	656	140	Uniform	5.81 ± 0.16	4.1	4.25 ± 0.02	1.02
3	29	28°	665	140	LMOC	4.97 ± 0.20	4.03	4.23 ± 0.01	0.98
3	29	28°	675	140	MMOC	5.04 ± 0.16	4.05	4.25 ± 0.01	0.98
4	29	28°	385	140	Uniform	4.32 ± 0.14	4.14	4.30 ± 0.01	0.93
4	29	28°	523	140	Uniform	4.87 ± 0.12	3.93	4.28 ± 0.02	0.98
4	29	28°	656	140	Uniform	5.81 ± 0.16	4.1	4.25 ± 0.02	1.02
4	29	28°	791	140	Uniform	6.06 ± 0.24	4.04	4.23 ± 0.02	1.04
5	15	28°	682	70	Uniform	2.97 ± 0.08	4.3	5.15 ± 0.05	0.91
5	15	28°	682	140	Uniform	5.44 ± 0.20	4.08	4.20 ± 0.03	1

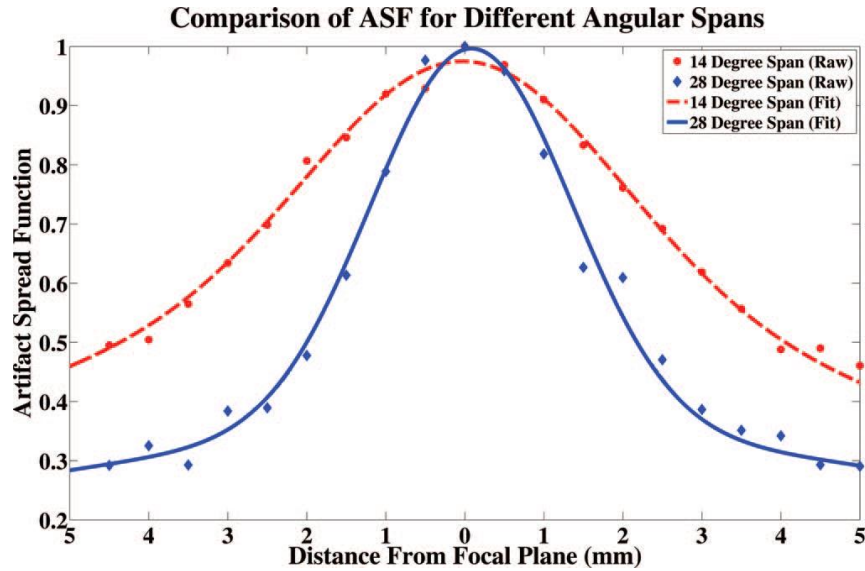


Figure 5.27 ASF plots for 14° and 28° angular span with equal number of projections and entrance dose. Reprinted with permission from Tucker et al., Med. Phys., 40, 031917-8, (2013). Copyright 2013, American Association of Physicists in Medicine.

Further analysis of system configuration parameters effect on the ASF were conducted by reducing the angular coverage while simultaneously reducing the total entrance dose. For this experiment, the entrance dose per projection was kept constant, and the angular coverage was decreased by omitting the necessary projection images. Figure 5.5 shows the relationship of the s-DBT system FWHM of the ASF against the increasing angular span. Based on the figure, it is observed that the ASF increases with increasing angular span of the projection images. The ASF results indicate that the ASF is affected solely by the angular coverage, and is unresponsive to the number of projection images and entrance dose for a fixed angular span.

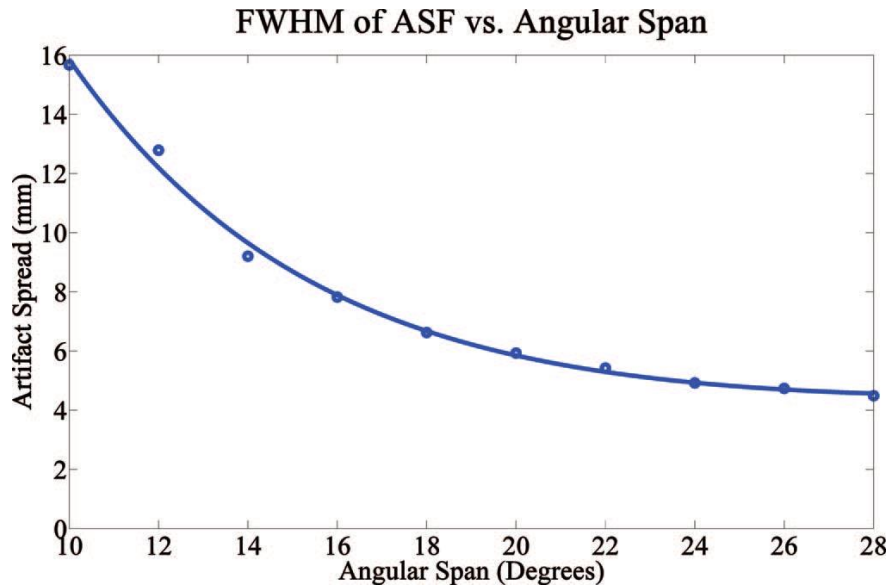


Figure 5.28 FWHM of the ASF versus increasing angular span of the tomosynthesis acquisition. A decrease in the ASF is observed with increasing angular span. Reprinted with permission from Tucker et al., Med. Phys., 40, 031917-8, (2013). Copyright 2013, American Association of Physicists in Medicine.

The decrease in the object artifacts in planes away from the focal plane of the object is as a result of the increase in information in the Fourier domain^{12,18}.

The most commonly accepted, and proven measure of determining the spatial resolution of a medical x-ray imaging system is the modulation transfer function (MTF)^{19,20}. The MTF characterizes the spatial frequency response of an imaging system, which provides a useful measure of system performance for characterization and comparison²¹. The resolution of an x-ray imaging system is the capability of this system to differentiate two objects. For this study, the 1st generation system MTF dependence on system configuration was measured from the in-focus slice of the wires in the phantom for each respective configuration. System configurations are listed in Table 5.2. Multiple line spread functions (LSFs) were generated and transformed into a single oversampled LSF using the calculated angle the wire²². The oversampled LSF was then fitted to a Gaussian and the MTF calculated by taking the discrete Fourier transform of the fitted

Gaussian. The corresponding frequency at 10% of the MTF was taken as the in-plane resolution. The system detector was operated in both 2 x 2 binning mode and full resolution mode with respective pixel sizes of 140 x 140 μm and 70 x 70 μm effective pixel size.

System MTF for each configuration is also listed in Table 5.2. As observed, a notable change in system MTF was observed only with the change in detector pixel size. This is because the in-plane resolution is governed mainly by x-ray focal spot size and detector pixel size for the same reconstruction method. Since system MTF depends mainly on focal spot size, and detector pixel size, this also serves as a good indication of the limiting factors of the in-plane spatial resolution of the system. Figure 5.6 shows the plotted system MTFs for equal number of projections and entrance dose for both detector pixel sizes. Using the 10% value as the in-plane spatial resolution, the MTFs were 5.15 ± 0.05 cycles/mm and 4.2 ± 0.03 cycles/mm for the 70 μm and 140 μm pixel sizes respectively. The smaller detector pixel size resulted in a 25% increase in the in-plane spatial resolution for the s-DBT system. This result suggests that given the system's current effective focal spot size, the in-plane resolution can be further improved with a higher resolution detector.

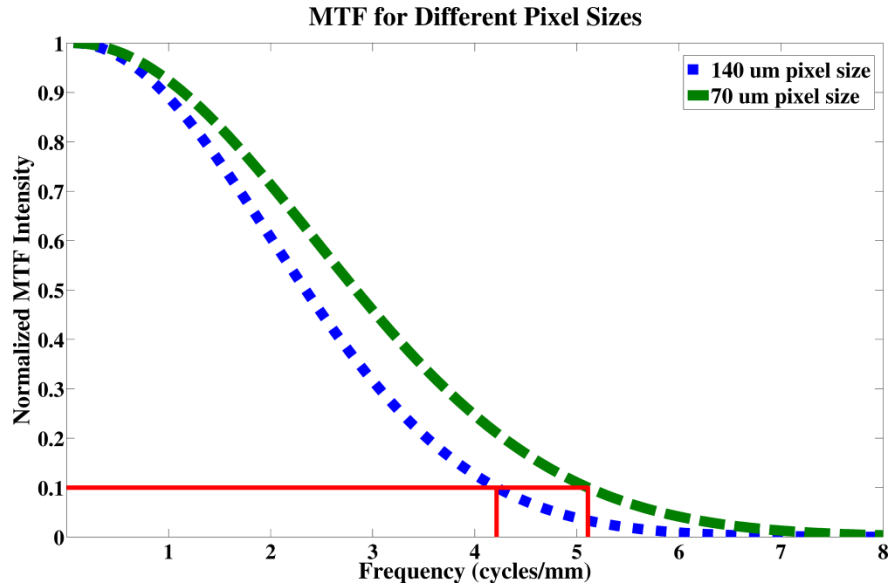


Figure 5.29 MTF plots comparing the 70 μm pixel size and the 140 μm pixel size. MTF at 10% was used as the figure of merit. The 70 μm pixel size (5.1 cycles per mm) when compared to the 140 μm case (4.2 cycles per mm) was approximately 25% better. Reprinted with permission from Tucker et al., Med. Phys., 40, 031917-8, (2013). Copyright 2013, American Association of Physicists in Medicine.

In determining the system's configuration that resulted in the highest reconstructed image resolution, the in-plane and depth resolution together with signal difference to noise ratio (SdNR) of the simulated mass in the ACR phantom (see Figure 5.7) were combined to form a quality factor metric (QF)¹². The QF is an indication of the system performance to detect masses and MCs, and is given by the equation:

$$QF = \frac{1}{3} \left(\frac{SdNR}{SdNR_0} + \frac{ASF_0}{ASF} + \frac{MTF}{MTF_0} \right) \quad (5.20)$$

Where "SdNR" is the signal difference to noise ratio calculation, "ASF" is the FWHM of the artifact spread function, and "MTF" is the spatial resolution at 10% MTF peak value. MTF_0 ,

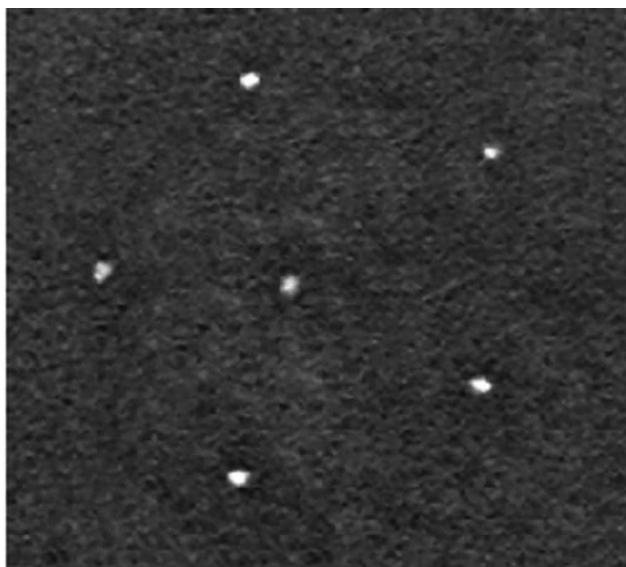


Figure 5.30 Magnified view of the 0.54 mm speck cluster found in the ACR phantom. ASF analysis was completed on all specks in the cluster for each configuration

SdNR₀, and ASF₀ are the corresponding values for the reference configuration of 28°, 15 projection views, 682 mR, and 140 μ m detector pixel. All calculated quality factors are listed in Table 5.2. As expected, keeping the detector pixel size constant, the SdNR of the system increases with increasing entrance dose. Neither angular span nor the number of projection had any significant impact on the SdNR when investigated at similar entrance doses. However, the detector pixel size affected the SdNR for similar imaging parameters, with the full resolution (70 μ m pixel) resulting in a poorer SdNR. This decrease in SdNR is counterproductive to the increase in system resolution gained from the decrease in detector pixel size. Based on the calculated image QFs, the highest resulting QFs for the same entrance dose was the configuration with 29 projections evenly distributed over a 28° span, and the detector in 2 x 2 binning mode¹⁴. However, keeping entrance dose constant, increasing the number of projections increases total image acquisition time. Long image acquisition times are unfavorable as it allows for greater patient motion. Less than 2% degradation in the QF is observed using the same

angular span, similar entrance dose, and 15 projection images for the binned detector. Since using 15 projections for the same total exposure (mAs) shortens imaging time by approximately 50% of the time required for 29 projections (14 less detector readout times, t_{read}), this was chosen as the optimal system configuration.

It is important to note that the QF used in this experiment gave equal weight to each metric in the QF equation. Therefore, the optimal QF for this phantom study may not be optimal in the clinical setting as it excludes the effects of other external factors such as patient motion, and image quality preference by radiologist.

5.3 Specimen study

Since the s-DBT system was shown to have improved spatial resolution and image quality in phantom evaluations compared to the CMDBT system, we evaluated its performance in the imaging of breast biopsied specimens against FFDM, and CMDBT in two separate studies^{23,24}. Thirty nine patients with known breast lesions scheduled for biopsies (BIRADS 4 and 5) were recruited under institutional review board (IRB) approved protocol. Following the lumpectomy, specimen samples were placed in specimen imaging and transport containers and imaged on a GE Senograph FFDM system (General Electric, Fairfield, CT USA), and s-DBT system. A subset of 23 of the 39 breast specimen samples were also imaged on a Selenia Dimensions DBT system. In the first study, s-DBT system performance was evaluated against FFDM in assessing whether s-DBT can improve surgical margin assessment in the lumpectomy specimens by radiologist evaluation²³. For the second study, MC visibility was evaluated between the s-DBT system and the CM DBT²⁴. These studies serve as a necessary precursor to human clinical trials. A summary of both studies is covered in this chapter.

5.3.1 Evaluation of s-DBT vs 2D

In excisional breast biopsies, the biopsied specimen is imaged using magnified 2D mammography to confirm the removal of the lesion by the surgeon or pathologist. However, the superimposition of tissue in the 2D image can make it difficult to detect lesion margins. Since DBT reduces the overlap of tissue, this modality may be potentially useful in the evaluation of biopsied specimens, and may reduce the surgical recall rate²³. However, the reduced visibility of microcalcifications of DBT makes it unfavorable compared to FFDM. The objective of this study was to evaluate whether s-DBT provided diagnostically equivalent tomographic images to FFDM in the assessment of lumpectomy specimens. Radiologist evaluated image quality based on masses, microcalcifications, and margins.

Materials and Methods

Specimens were first imaged on the GE Senography system (General Electric, Fairfield, CT USA) using 26 kVp tube potential, and dose based on the specimen sample thickness at a radiographic magnification of 1.8. Images were then taken via the s-DBT system using the optimal configuration as described in section 5.2.3 (15 projection images over a 28° angular span and detector pixel size of 140 µm). A total tube exposure of 100 mAs was used for imaging each specimen. Reconstruction of s-DBT datasets was conducted using the RTT software, with 0.5 mm slice spacing.

Four breast fellowship-trained radiologists were used to perform the reader study over two separate sessions. All images were viewed in each session showing half of the images in the 2D modality and the rest s-DBT first for the first session, and a reversal in the order with respect to which modality is viewed first in the second session after a 4 week washout period. Readers provided malignancy scores for both masses and MCs in the specimen ranging between 1 and 5,

with 1 being benign and 5 highly malignant. The reader preference in malignancy scoring between the two imaging modalities were documented for three categories (if relevant) for each specimen. The categories for assessment include mass margins, shape, morphology of masses, and MC evaluation. Reader preference in assessment of specimens was scored on an integer scale ranging from -3 and +3, with -3 indicating a strong preference to the 2D image, 0, indicative of indecisiveness, and +3, strong preference to s-DBT. Sensitivity and specificity were calculated based on reader malignancy scores, and the McNemar test was used to compare the degree to which readers' diagnosis is affected between the two modalities. A two-sided t test was applied to reader preferences to compare whether there was an observed difference between imaging modalities. Further analysis on the reader preference was conducted using a linear mixed model with a random intercept effect and the Wald test, to determine whether the mean reader preference was larger than zero²³. Cohen kappa method was also used to compare the consistency of the reader preference over time.

Results

The pathological diagnoses of the specimen samples determined that of the 39 patients, 20 patients were BIRADS 4 (51%) and 19 were BIRADS 5 (49%). Of the BIRADS 4 and 5 patients, 8 (40%) and 17 (89%) were determined to be malignant respectively. Reader sensitivity and specificity for each imaging modality were calculated for each reader based on the pathological results, and is reported Table 5.3. Since the malignancy scale used in our study was not based on BIRADS scoring, values ranging between 3 and 5 were interpreted as malignant (positive). Readers 1 and 3 have a total of 38 responses as they failed to score for one patient. Comparing the readers' performance in sensitivity, readers 3 and 4 scored higher sensitivity values for s-DBT than 2D mammography, both identifying all of the malignant cases.

Conversely, reader 1 and 2 recorded higher sensitivity values for 2D mammography, where reader 1 identified all, and reader 2 identified 84% of the malignant cases. In comparing specificity, readers 1 and 4 recorded higher values for 2D mammography, both identifying 29% of the benign cases. Reader 2 was the only reader that had higher specificity values for s-DBT, identifying 50% of the cases. Reader 3 did not identify any benign cases for either imaging modality.

Table 5.7 Sensitivity and specificity values by Reader and Modality. Reprinted from Tucker et al., Acad Radiol. 2014 Dec; 21(12):1547-52.

Reader	Sensitivity		Specificity	
	FFDM	s-DBT	FFDM	s-DBT
1	24/24 (1.00)	23/25 (0.92)	4/14 (0.29)	2/13 (0.15)
2	21/25 (0.84)	19/25 (0.76)	5/14 (0.36)	7/14 (0.50)
3	24/25 (0.96)	25/25 (1.00)	0/13 (0.00)	0/13 (0.00)
4	23/25 (0.92)	25/25 (1.00)	4/14 (0.29)	2/14 (0.14)

The results of the McNemar test used to investigate the disagreement in diagnosis between two modalities are reported in Table 5.4. Readers 1, 2 have p-values greater than 0.05 that are indicative of no significant difference in diagnosis based on imaging modality. Reader 3's p value was not applicable as there was no observable difference between the two modalities, hence, like readers 1 and 2, there was no significant difference in the diagnosis between modalities. Only reader 4 had a p-value less than 0.05, which suggests that the diagnosis of the specimen is dependent on the imaging modality.

Table 5.8 Calculated values from the McNemar test showing the disagreement between imaging modalities for the four readers. Reprinted from Tucker et al., Acad Radiol. 2014 Dec; 21(12):1547-52.

Modality = FFDM	Modality = s-DBT		
	Negative	Positive	Subtotal
Reader 1 (P = 0.5637)			
Negative	1	1	2
Positive	2	32	34
Subtotal	3	33	36
Reader 2 (P = 0.2482)			
Negative	5	4	9
Positive	8	22	30
Subtotal	13	26	39
Reader 3 (P = NA)			
Negative	0	0	0
Positive	0	35	35
Subtotal	0	35	35
Reader 4 (P = 0.0455)			
Negative	2	4	6
Positive	0	33	33
Subtotal	2	37	39

Table 5.5 presents the results from the two-sided *t* test conducted on reader preference with respect to masses, MCs, and margins. Positive values represent a preference for s-DBT and conversely, negative values represent a preference for 2D mammography. Based on the mean preference, it can be seen that readers had a higher preference in s-DBT for masses and mass margins, with average preferences of 0.07 ± 1.34 and 0.16 ± 1.22 respectively. With respect to MCs, the mean preference was -0.7 ± 0.95 indicative of reader preference in 2D mammography. Three out of four readers showed a significant confidence in their preference to 2D mammography over s-DBT ($P < .05$).

Table 5.9 Results of the two-sided t test on reader preference. Positive values represent a preference for s-DBT compared to 2D mammography. Reprinted from Tucker et al., Acad Radiol. 2014 Dec; 21(12):1547-52.

Reader	Masses			Microcalcifications			Margins		
	Mean	SD	P Value	Mean	SD	P Value	Mean	SD	P Value
1	-1.02	1.40	<.05	-1.80	1.01	<.05	-0.44	1.35	<.05
2	0.18	1.20	.4094	-0.54	0.70	<.05	0.19	1.14	.2984
3	0.75	1.35	<.05	-0.20	0.98	0.259	0.70	1.35	<.05
4	0.08	0.86	.5800	-0.62	0.52	<.05	0.21	0.72	.0743
Overall	0.07	1.34	-	-0.70	0.95	—	0.16	1.22	—

Secondary analysis using the mixed linear model showed the same trend in reader preference, with s-DBT being favored over 2D mammography for masses and margins, and FFDM being favored for MCs. Results for the mixed linear model are displayed in Table 5.6.

The concordance of the reader preference consistency between reads, as indicated by the Cohen kappa value, gave values of 0.2, 0.21, 0.46 and 0.35 for readers 1 through 4 respectively. Based on these values readers 3 and 4 had larger level of agreement between reads compared to readers 1 and 2.

Discussion

Based on the results and analysis, the two imaging modalities performed identically in malignancy diagnosis. The positive predictive value for s-DBT was only 3% higher than that of FFDM. Average reader preferences indicated a trend towards s-DBT for masses and margins, though there was no substantial difference ($P > .05$). The increased conspicuity of the masses and margins were as a result of the decreased overlapping of tissue. With respect to MCs, readers had significantly more confidence in 2D mammography ($P < .05$), indicative of better MCs visibility. For this study, MCs were imaged at a magnification factor of 1.8 for FFDM, compared to 1.08

for the s-DBT system. The ability of a FFDM system to utilize a smaller focal spot at increased magnification views gives this technique a unique advantage over all DBT systems. The increased magnification, coupled with a small focal spot results in magnified images without increasing the x-ray penumbra effect. DBT systems use relatively large focal spot sizes due to anode power limitations, and increasing the radiographic magnification would increase the x-ray penumbra effect resulting in blurred images. This magnification of MCs may be responsible for the readers' significant preference of FFDM.

Other limitations of the study include the storage container for specimens, as it is designed for 2D imaging. Grid patterns inside of the specimen imaging and transport containers, used for identifying locations of findings, cause imaging artifacts that reduce image quality. Another source of imaging artifacts arose from the presence of biopsy needles used to mark suspicious lesions. Removal of the grid pattern and biopsy needles will reduce image artifacts, and should be considered for future studies.

It is important to note that clinical studies involving “enriched” samples may result in biased results. Meaning that since the patients recruited were already suspected of having a malignancy, a bias was anticipated towards scoring specimens as malignant. This may explain the reason for both modalities having relatively low sensitivity.

In conclusion, this study reports the first human tissue images, using a CNT x-ray source array. Results have indicated that the s-DBT system performs comparably to the FFDM system in the malignancy diagnosis of the specimen sample, with a favorable preference in FFDM for MC visibility. Although minimal, readers' preferred s-DBT over FFDM for mass and margin evaluation. As a result, s-DBT may be a feasible alternative to FFDM in the imaging of lumpectomy specimens.

5.3.2 CM-DBT

As previously mentioned in, focal spot blurring in CM DBT decreases spatial resolution, and consequently decreases the visibility of microcalcifications. The physically quantified higher spatial resolution of the s-DBT system may result in increased MCs visibility in human imaging. This increase, if translated to the clinical setting, may negate the need for combination imaging of FFDM and DBT. The purpose of this study was to determine whether the measured gain in spatial resolution of the s-DBT system over the CMDBT system had any effect on MC visibility. Corresponding MCs on in-focus reconstructed slices from the s-DBT and CMDBT system were analyzed and compared for in-plane resolution (x and y plane) and depth resolution (z).

Methods and Materials

Twenty three of the thirty nine recruited patients' biopsied breast tissue were also imaged using a CM DBT (Hologic Selenia Dimensions 3D). The system acquired 15 projection images equiangular spaced over a 14 degree angular span (-7 to 7 degrees), and the detector was operated in 2 x 2 binning mode (140 um pixel size). A tube voltage of 26 kVp, and 100 mAs exposure were used for imaging every specimen. The corresponding 23 of the 39 patient specimens imaged on s-DBT prior to imaging on the CM DBT system were also imaged at 26 kVp tube voltage, 100 mAs exposure, and the detector in binning mode. Both imaging data sets were reconstructed using RTT software, utilizing a slice spacing of 0.5 mm.

Only specimen images where MCs were seen on images from both imaging modalities were considered for analysis. Additional, only isolated MCs were selected for ease of processing. Accordingly, 12 MCs selected for analysis. Under the assumption that a smaller area is symbolic of sharper imaging, in-plane resolution of the MCs were quantified by the area estimate. Area estimates were determined using a localized thresholding method for the respective regions of

interest²⁴. The localized thresholding method involved establishing a 50% cutoff based on the maximum pixel intensity of the MCs. Only the pixels above the cutoff were considered as part of the MCs, and they were multiplied by the reconstructed pixel size to produce the estimated area of the MC. Depth resolution of the systems were measured by calculating the FWHM of the ASF for the isolated MCs for both modalities. The ASF equation is given in section 5.23.

Results

Figure 5.8 contains graphical representations of the comparison for MC area calculations. The calculated areas were smaller for all MC reconstructed from the s-DBT system, indicative of sharper MC images. An average decrease of $29 \pm 13 \%$, and up to a 43% decrease in the areas of some MCs were observed moving from DBT to s-DBT. Figure 5.9 shows an example of a MC chosen for analysis and its corresponding magnified ROI for both imaging modalities. MCs appear sharper in the s-DBT magnified ROI compared to that of CM DBT. Figure 5.10 shows a visual comparison of 6 MCs at equal magnification chosen for analysis. Based on the figure, it can be visually observed that the MCs imaged by s-DBT appear sharper than those imaged on CM DBT.

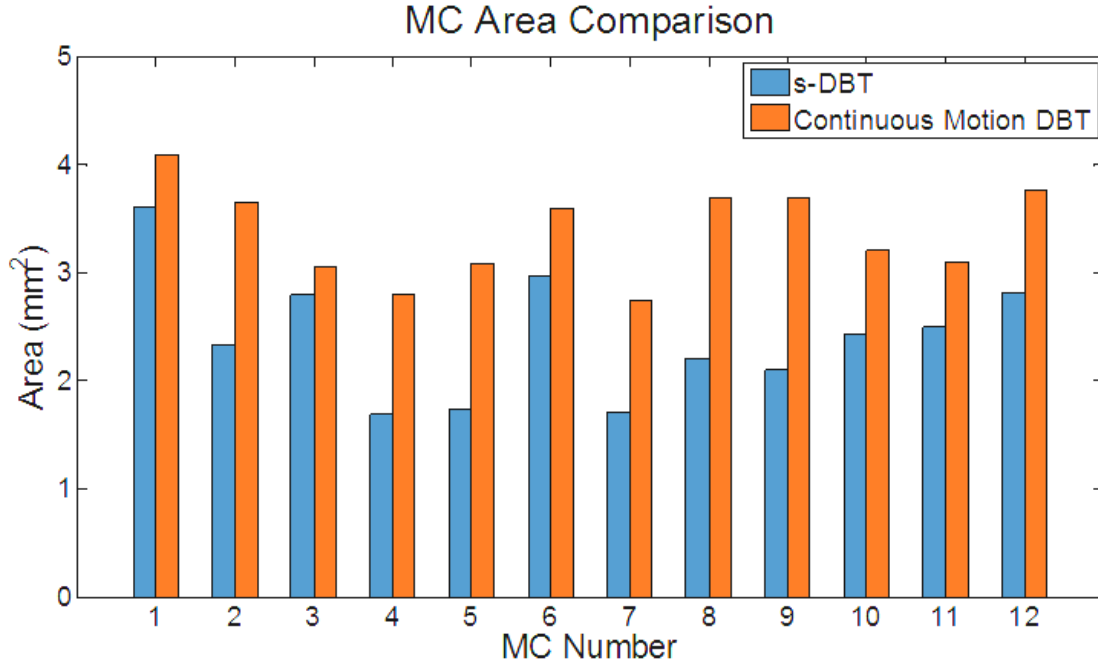


Figure 5.31 Graph comparing the calculated MC area for both imaging modalities. s-DBT resulted in smaller MC areas for each MC measured

Figure 5.11 is the graphical representation comparing the FWHM of the ASF for all 12 MCs. As observed, a smaller FWHM of the ASF was recorded for all 12 MC imaged via s-DBT compared to CM DBT, with an average difference of 2 ± 0.67 mm. This confirms that the wider angular span of the s-DBT increased depth resolution compared to CM DBT. Figure 5.12 shows a plot comparing the ASF for the 2nd analyzed MC.

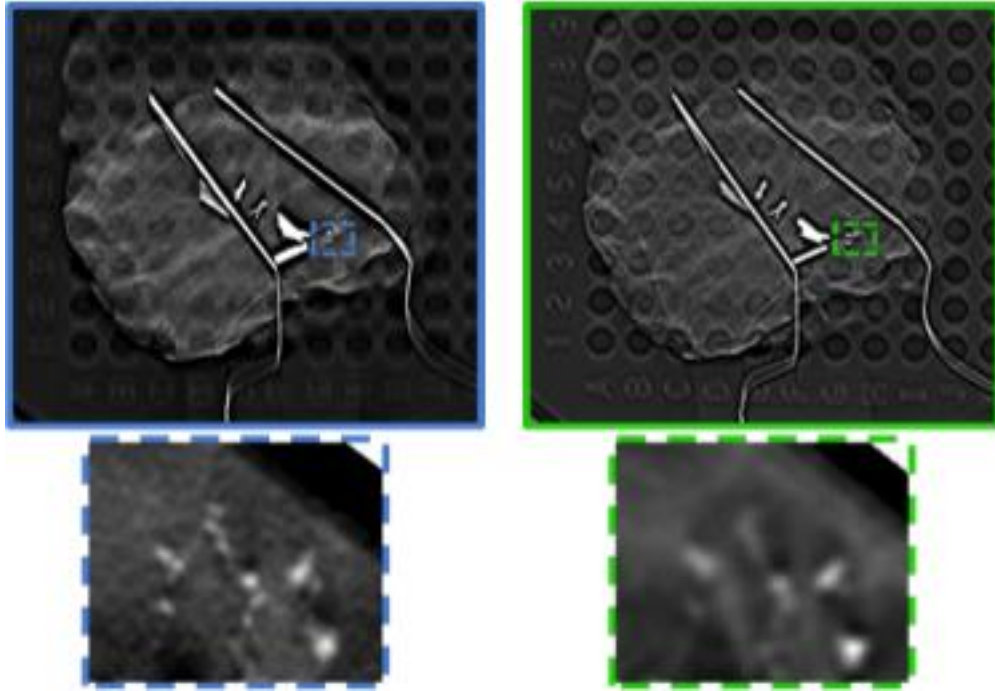


Figure 5.32 Reconstruction slice of a specimen with a large cluster of MCs using the s-DBT system (Top-Left) and the continuous motion DBT system (Top-Right). MC sharpness is superior in the zoomed in s-DBT reconstruction (Bottom-Left) compared to the continuous motion DBT system (Bottom-Right). Reprinted with permission from SPIE. Tucker et al., Increased microcalcification visibility in lumpectomy specimens using a stationary digital breast tomosynthesis system, Proc. of SPIE, 2014.

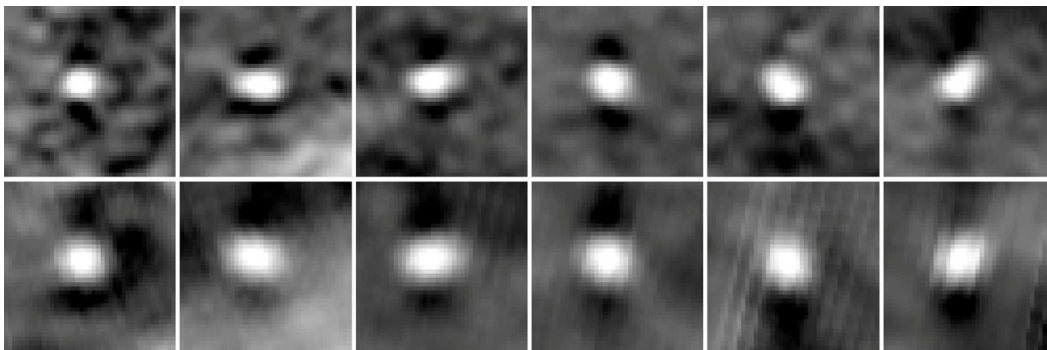


Figure 5.33 Magnified ROIs of 6 MCs. The row above contains the s-DBT reconstruction images, while the row below contains the continuous motion DBT system reconstruction images. Less blur in the x-y plane is visually observed for all 6 MCs. Reprinted with permission from SPIE. Tucker et al., Increased microcalcification visibility in lumpectomy specimens using a stationary digital breast tomosynthesis system, Proc. of SPIE, 2014.

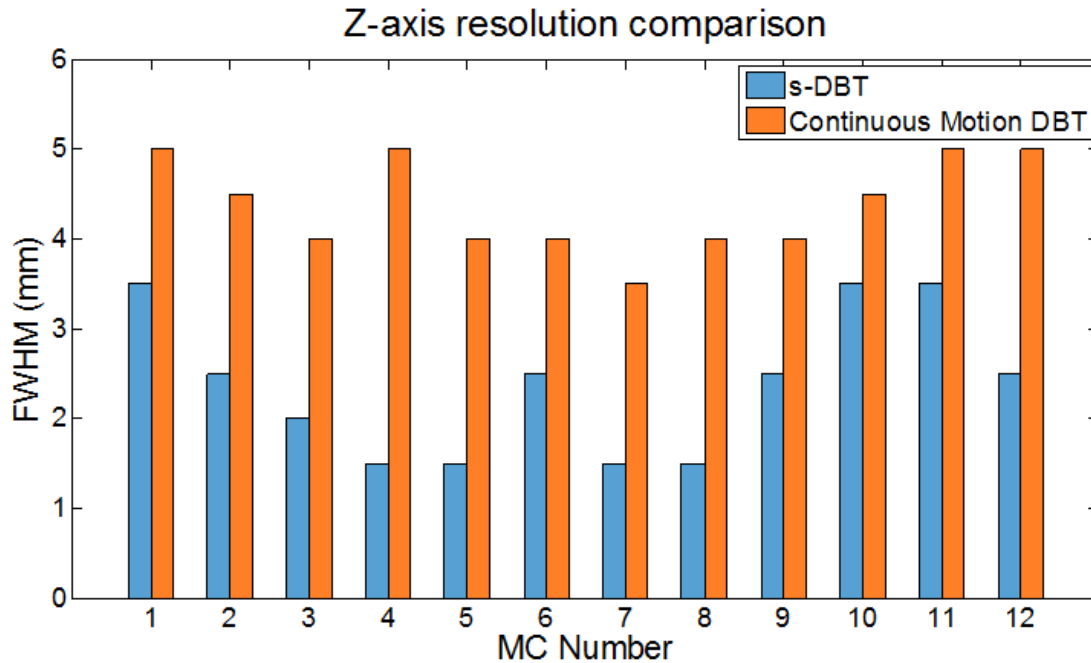


Figure 5.34 Comparison of the FWHM of the ASF for s-DBT and continuous motion DBT.s-DBT's wider angular span resulted in narrower ASF

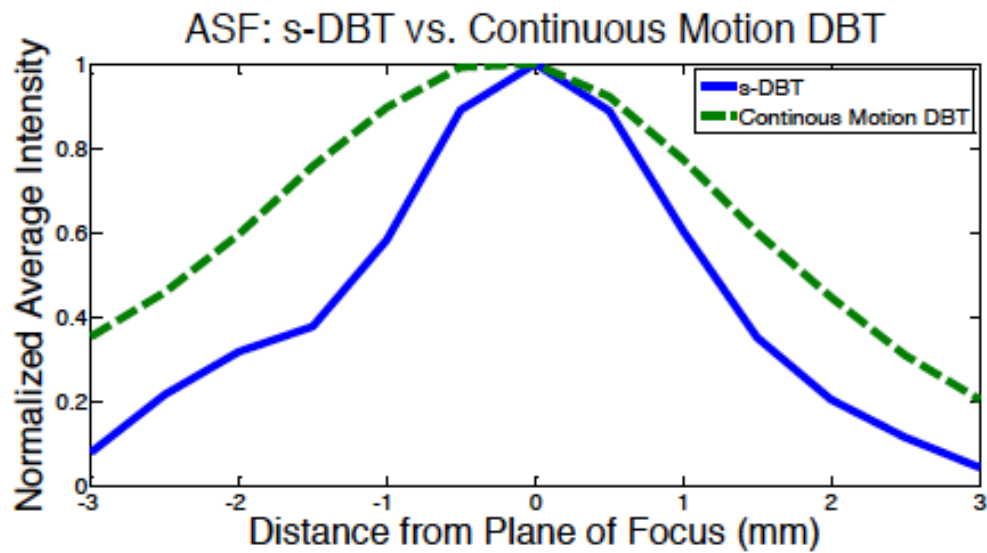


Figure 5.35 Plot of the ASF for s-DBT and continuous motion DBT for MC number 6. The larger angular coverage of the s-DBT system reduces out-of-plane reconstruction artifacts. Reprinted with permission from SPIE. Tucker et al., Increased microcalcification visibility in lumpectomy specimens using a stationary digital breast tomosynthesis system, Proc. of SPIE, 2014.

Discussion

For each MC, areas measured from s-DBT images produced lesser values. Provided the assumption that the MC area is indicative of sharpness, the increased MC visibility in s-DBT is as a result of its increased in-plane resolution over s-DBT. With respect to the ASF, the decrease moving from CM DBT to s-DBT was expected due the larger angular span of s-DBT. The larger angular span reduces out of plane artifacts as more data is sampled in the Fourier domain¹². Since s-DBT imaging time is independent of angular span, this is a unique advantage that can be exploited in human imaging, as depth resolution could be increased without compromising imaging time. These results are suggestive of the improved performance of s-DBT over CM DBT for the imaging of MCs. This improvement in MC visibility may negate the need for combination imaging, reducing overall patient dose.

5.4 Clinical Trial

5.4.1 Purpose

As the s-DBT system showed improved spatial resolution over CM DBT in phantom studies, and lumpectomy specimen imaging, and performed comparably to FFDM in the lumpectomy specimen imaging, the system had to be evaluated in human imaging trials. The faster scan times and improved in-plane and depth resolution should result in better patient images. The objective of this study was to compare s-DBT and conventional 2D mammography devices with respect to radiologist confidence levels in evaluating patients with known breast lesions²⁵.

Study population

The clinical study was approved by the University of North Carolina's Institutional Review Board regulations (Clinical Trials.gov registration number NCT01773850). One hundred

consenting women are currently being recruited. Patients with showing breast lesions discovered by mammography and BI-RADS scores of 4 or 5, scheduled to undergo breast biopsy, were enrolled in this study. Preceding to the surgical breast biopsy procedure, patients were imaged on the s-DBT system by a specialized mammography technologist. Patient dose was administered based on patient compression thickness adapted from Hologic's suggested technique chart for normal (50% adipose, 50% glandular) breast. Scan time ranged from 2.5 s to 5 s, based on patient dose. 2D and reconstructed s-DBT images were downloaded onto a dedicated computer in the mammography reading room at the UNC Cancer Hospital for radiologists to evaluate. Fifty-five patients have been recruited to date.

Materials and Methods

A GE Senographe 2D mammography system was used for each patient's diagnostic digital mammography image set. This system utilizes a Mo/Rh target/filter combination with a 100 μm pixel size, cesium iodide (CsI) detector. Tube potential and exposure were based on UNC Mammography's clinical protocol for patients based on compression thickness. Patient were images in both craniocaudal view (CC) and mediolateral oblique (MLO) views.

Image reconstruction was conducted using software developed by Real Time Tomography, LLC (Villanova, PA). All 3D reconstructions have 0.5 mm slice spacing.

Three breast-fellowship trained radiologists conducted a preliminary reader study on 10 patient images and the findings were presented at the SPIE Medical Imaging Conference²⁵. For assessment, s-DBT images were read first, assessing breast density, lesion type, BI-RAD scoring, and confidence levels (-2 not confident; 0 neutral; +2 very confident). Upon evaluation of the s-DBT data set, readers were provided with the 2D FFDM images to determine whether there was any additional diagnostic information.

5.4.2 Results

Images in Figure 5.13 shows the FFDM image and corresponding reconstructed slice of a patient breast using the GE Senographe system and s-DBT system. Mass conspicuity (highlighted by red circle) is more obvious in the s-DBT reconstructed slice, while the superimposition of breast tissue makes it difficult to locate the mass in the FFDM image. The tumor extension to the skin in s-DBT is highlighted by the red circle, which was not seen in the FFDM 2D image.

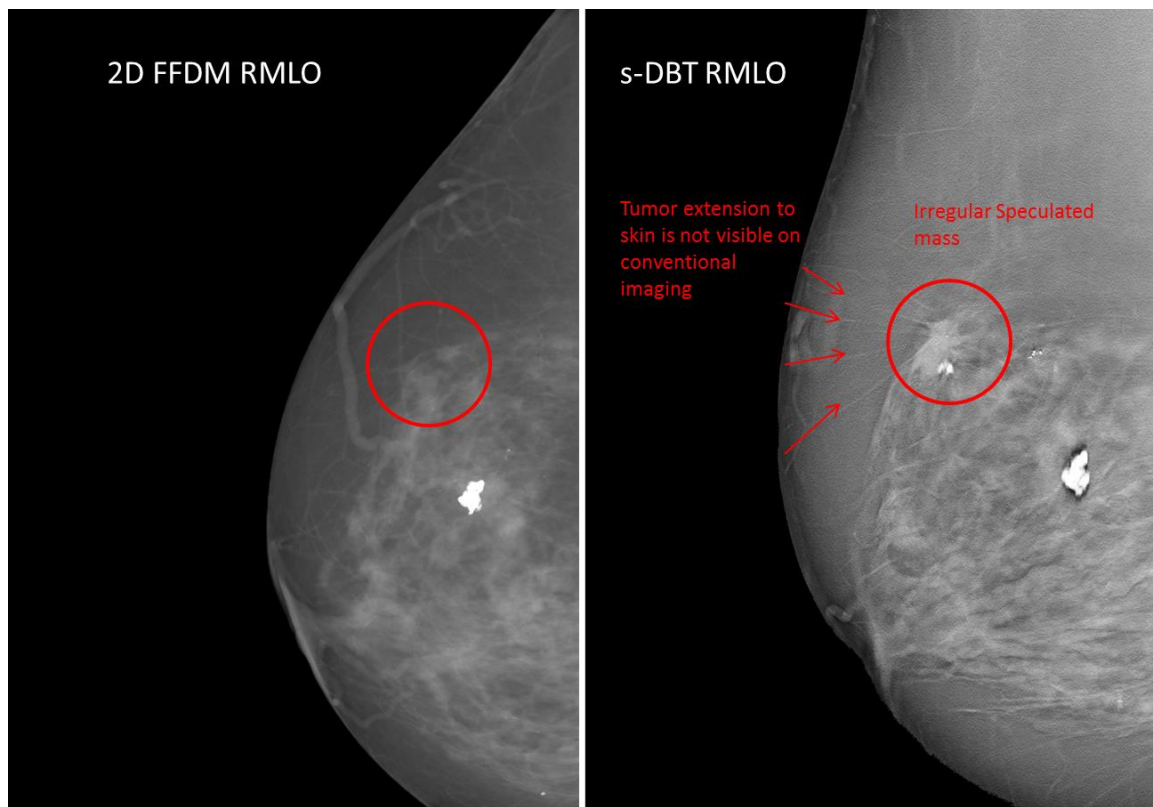


Figure 5.36 (Left) FFDM image of a patient in the MLO view. (Right) Reconstructed slice of the same patient in MLO view. In the s-DT reconstructed slice, a speculated mass is clearly observed while this is not observed in the 2D image. Tumor extension towards the skin is visible only in the s-DBT slice. Reprinted from Jabari Calliste et al. SPIE Med. Imaging Phys. Med. Imaging (2015), p. 941228²⁵.

Figure 5.14 below shows magnified ROI containing MC clusters in FFDM images and s-DBT reconstructed slices of patients' breasts. MCs visible on the 2D FFDM images are visible and focused at different slice depths in the 3D reconstruction volume. Visual inspection of the image comparisons look analogous.

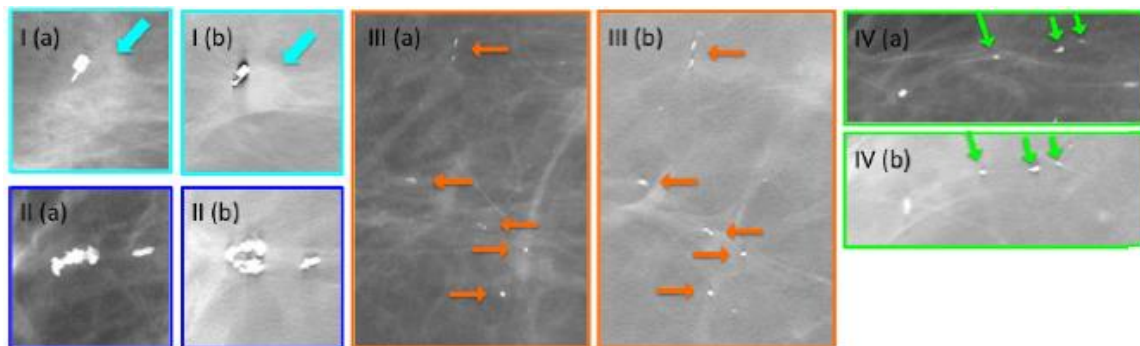


Figure 5.37 Magnified ROIs with calcification clusters. (I) Zoomed in image of a suspicious mass in (a) a FFDM image and (b) an s-DBT reconstructed slice with the mass in focus, of a patient breast with known lesions. (II, III, IV) Zoomed in images of MC clusters in (a) FFDM image and (b) an s-DBT reconstruction slice with the MC cluster in focus, of a patient breast with known lesions. Reprinted from Jabari Calliste et al. SPIE Med. Imaging Phys. Med. Imaging (2015), p. 941228

Table 5.6 list the preliminary reader results. Visibility of masses and their margin, as a result of tissue overlap elimination in s-DBT, resulted in all radiologists being more confident in s-DBT for masses. Microcalcification clusters were viewed equivalently in both modalities for most cases. For few cases, MC visibility was better in FFDM, however, it did not change the outcome of the readers' diagnosis. Sharper MC images in FFDM are due to the smaller focal spot size compared to s-DBT. Based on the radiologists' findings, s-DBT may be diagnostically equivalent to FFDM.

Table 5.10 The radiologist findings of 10 evaluated patients. Reprinted from Jabari Calliste et al. SPIE Med. Imaging Phys. Med. Imaging (2015), p. 941228

S-DBT					2D MAMMO	
No.	Breast Density	Lesion Type	BI-RADS Scoring	Confidence	Additional Diagnostic Information	Additional Notes
4	Heterogeneously Dense	Mass	3, 4A, 4A	+2	No new diagnostic information	Margins are significantly better in tomo
		Microcalcs	Benign	+2		
7	Heterogeneously Dense	Mass & Calcs	5	+2	No additional diagnostic information	Margins are much better with tomo MC visualization appears the same
9	Scattered	Mass	4A	+2	No additional diagnostic info.	2nd lesion better in mammo
		Mass	4A, 4A, 3	+2		
13	Scattered	Mass	5	+2	No additional diagnostic info.	Mass margins significantly better in tomo
		Microcalcs	4A	+2		See more benign calcs (does not change procedure)
		Microcalcs	Benign			
14	Heterogeneously Dense	Mass	3	+2	No additional diagnostic info.	Definitely more confident in tomo for mass

		Microcalcs	4A	+2		MC visualization the same
		Microcalcs	Benign	+2		
15	Scattered	Mass	4B, 4B, 4A	+2	No additional diagnostic info.	Mass margin better with tomo.
		Microcalcs	Benign	+2		
17	Heterogeneously Dense (2) & Extremely Dense	Microcalcs	4A	0	No additional diagnostic info.	Cannot see architectural distortion
18	Fatty	Mass	4A, 3	+2	Nothing new diagnostically	Tomo superior in viewing masses
		Microcalcs	Benign	+2		Calcs not observed
19	Heterogeneously Dense	Mass	5	+2	Diagnostically equivalent	Mass margins significantly better with tomo
		Microcalcs	Malignant	0		Smaller calcs viewed better on mammo
		Microcalcs	Benign	+2		
23	Scattered	Mass	Benign	+2	Diagnostically equivalent	Mass margins better with tomo

5.4.3 Discussion

The preliminary results from this study are indicative that the s-DBT system can produce increased lesion conspicuity and comparable MC visibility, with respect to a GE Senographe 2D

mammography system. Movement of the x-ray tube in CM, and to a lesser extent SSM DBT systems, causes focal spot blur degrading image quality. The higher spatial resolution of the s-DBT system compared to the current DBT systems is attributed to its stationary focal spots. This increase in the in-plane resolution improved microcalcifications visibility. When compared to FFDM system, microcalcification visibility is less distinct. This is expected because of the FFDM system has a smaller focal spot size, giving it higher resolution. However, according to the readers, MCs observed on FFDM 2D images are visible with s-DBT and produced equivalent diagnostic readings.

The s-DBT system is capable of acquiring images over large angular spans without a compromise in scan time. This unique advantage increases z-axis resolution, without additional image degradation due to patient motion. Present FDA approved systems, GE Senoclaire, and Hologic Selenia Dimensions, have imaging times of 9 s and 4.5 s respectively, with smaller acquisition angles than s-DBT²⁶. This s-DBT system is capable of attaining faster acquisition times with the most current detector technology, and can be further improved with a reduction in detector readout time.

The initial findings of the first-ever clinical trial using CNT stationary X-ray source arrays for human imaging are presented here. The preliminary results demonstrated that s-DBT is superior in lesion conspicuity, and comparable in MC visualization, compared to 2D FFDM. Completion of this study is necessary for statistical significance, and upon completion, may show improvement of MC visualization in s-DBT compared to CM and SSM DBT, and images that are diagnostically equivalent to FFDM²⁵. If so, this may lead to the subsequent negation of 2D mammography images, resulting in a reduction of overall patient dose.

5.5 REFERENCES

- ¹ A. Tagliafico, N. Houssami, and M. Calabrese, editors , *Digital Breast Tomosynthesis* (Springer International Publishing, Cham, 2016).
- ²*Digital Breast Tomosynthesis* (2010).
- ³ M. Scimeca, E. Giannini, C. Antonacci, C.A. Pistolese, L.G. Spagnoli, and E. Bonanno, *BMC Cancer* **14**, 286 (2014).
- ⁴ J.S. Nelson, J.R. Wells, J.A. Baker, and E. Samei, *Med. Phys.* **43**, 2538 (2016).
- ⁵ M.L. Spangler, M.L. Zuley, J.H. Sumkin, G. Abrams, M.A. Ganott, C. Hakim, R. Perrin, D.M. Chough, R. Shah, and D. Gur, *AJR. Am. J. Roentgenol.* **196**, 320 (2011).
- ⁶ A. Tagliafico, G. Mariscotti, M. Durando, C. Stevanin, G. Tagliafico, L. Martino, B. Bignotti, M. Calabrese, and N. Houssami, *Eur. Radiol.* **25**, 9 (2015).
- ⁷ R.A. Robb, E.A. Hoffman, L.J. Sinak, L.D. Harris, and E.L. Ritman, *Proc. IEEE* **71**, 308 (1983).
- ⁸ H.T. Morgan, (2000).
- ⁹(n.d.).
- ¹⁰ X. Qian, A. Tucker, E. Gidcumb, J. Shan, G. Yang, X. Calderon-Colon, S. Sultana, J. Lu, O. Zhou, D. Spronk, F. Sprenger, Y. Zhang, D. Kennedy, T. Farbizio, and Z. Jing, *Med. Phys.* **39**, 2090 (2012).
- ¹¹ I. Reiser and R.M. Nishikawa, *Med. Phys.* **37**, 1591 (2010).
- ¹² I. Sechopoulos and C. Ghetti, *Med. Phys.* **36**, 1199 (2009).
- ¹³ J. Zhou, B. Zhao, and W. Zhao, *Med. Phys.* **34**, 1098 (2007).
- ¹⁴ A.W. Tucker, J. Lu, and O. Zhou, *Med. Phys.* **40**, 031917 (2013).

- ¹⁵ Y.-H. Hu, B. Zhao, and W. Zhao, *Med. Phys.* **35**, 5242 (2008).
- ¹⁶ Y. Zhang, H.-P. Chan, B. Sahiner, J. Wei, M.M. Goodsitt, L.M. Hadjiiski, J. Ge, and C. Zhou, *Med. Phys.* **33**, 3781 (2006).
- ¹⁷ A.W. Tucker, J. Lu, and O. Zhou, *Med. Phys.* **40**, 031917 (2013).
- ¹⁸ A.S. Chawla, J.Y. Lo, J.A. Baker, and E. Samei, *Med. Phys.* **36**, 4859 (2009).
- ¹⁹ A. Kuhls-Gilcrist, A. Jain, D.R. Bednarek, K.R. Hoffmann, and S. Rudin, *Med. Phys.* **37**, 724 (2010).
- ²⁰ A.L.C. Kwan, J.M. Boone, K. Yang, and S.-Y.Y. Huang, *Med Phys* **34**, 275 (2007).
- ²¹ I.A. Cunningham and A. Fenster, *Med. Phys.* **14**, 533 (1987).
- ²² H. Fujita, D.-Y. Tsai, T. Itoh, K. Doi, J. Morishita, K. Ueda, and A. Ohtsuka, *IEEE Trans. Med. Imaging* **11**, 34 (1992).
- ²³ A.W. Tucker, J. Calliste, E.M. Gidcumb, J. Wu, C.M. Kuzmiak, N. Hyun, D. Zeng, J. Lu, O. Zhou, and Y.Z. Lee, *Acad. Radiol.* **1** (2014).
- ²⁴ A.W. Tucker, Y.Z. Lee, C.M. Kuzmiak, J. Calliste, J. Lu, and O. Zhou, in *SPIE Med. Imaging*, edited by B.R. Whiting and C. Hoeschen (International Society for Optics and Photonics, 2014), p. 903316.
- ²⁵ J. Calliste, A.W. Tucker, E. Gidcumb, C.M. Kuzmiak, J. Lu, O.Z. Zhou, and Y.Z. Lee, in *SPIE Med. Imaging Phys. Med. Imaging* (2015), p. 941228.
- ²⁶ I.S. Reiser and I. Sechopoulos, *Med. Phys. Int. J.* **2**, 57 (2014).

CHAPTER 6:A new generation s-DBT system

6.1 Motivation

Mammography screening is the current gold standard for the early detection of breast cancer, and through randomized trials, has shown to reduce mortality¹. However, since mammography is a 2D imaging modality, it is inherently limited due to the superimposition of both normal and pathological tissue. The overlapping of tissue consequently makes it difficult to differentiate between malignant lesions, and normal tissue lowering the sensitivity and specificity of this imaging modality². As a means to overcome the limitations of 2D mammography, tomographic imaging methods were introduced. Digital breast tomosynthesis (DBT), a relatively new imaging modality, is an imaging technique that produces pseudo 3D images of the breast by reconstructing multiple low dose x-ray projections over a limited angle. This reduces tissue overlap, making lesions more conspicuous with the additional depth information. Recent studies have shown a significant increase in cancer detection when DBT is added to 2D mammography^{3,4}. However, DBT has not shown an improvement in the imaging of microcalcifications (MCs) ⁵.

Currently, two DBT systems are FDA approved for use in the United States (Hologic, GE)⁶. These DBT systems utilize an x-ray tube with single source that moves around the breast in a fixed angular span in either continuous motion (CM) or a step-and-shoot motion (SSM). For continuous motion (e.g Hologic Selenia Dimensions DBT system), the x-ray tube is moves continuously along the arc and projection images are taken simultaneously at set positions. The main advantage of this type of acquisition is the imaging speed. However, there is the

disadvantage of focal spot blurring due to tube motion during imaging. Contrary to CM, the SSM (e.g. GE SenoClaire DBT system) stops at each designated position before acquisition of a projection image, which avoids focal spot blur due to motion. Though there is no motion due to tube travel, the abrupt stop may introduce residual vibrations which introduce focal spot blur. Another disadvantage of SSM is the long imaging times, which allows for patient motion and overall degradation in image quality². Therefore, in all DBT system which requires the mechanical motion of the x-ray source during the scan, the image quality is limited either due to the tube motion or the long scan time. This leads to the unfavorable decrease in MC visibility comparing the DBT to 2D mammography. MC visibility is instrumental in determination of malignancy of lesions in breast cancer diagnosis. Characteristics such as distribution, morphology, and size are important for determining malignancy. Since there is a reduction in MC visibility with DBT, the FDA approved systems have to be used in conjunction with 2D mammography or the system must have the capability for synthetic 2D imaging⁷.

To overcome the limitations of moving gantry DBT systems, we developed and demonstrated a first generation stationary breast tomosynthesis (s-DBT) system that uses a linear carbon nanotube (CNT) x-ray source array⁸. The 1st generation s-DBT (1G s-DBT) system consist of 31 CNT x-ray sources linearly distributed over a 30° angular span that are electronically controlled, and can be instantaneously triggered^{8,9}. Since the stationary sources are not subject to focal spot blur, and images can be acquired rapidly, the in-plane system resolution is improved. Additionally, image acquisition time is independent of angular span since there is no motion, allowing for large angular spans, thus higher in-depth resolution, without increasing the scan times. The improved resolution of the first generation s-DBT system over CM DBT has been demonstrated with image evaluation phantoms and a human specimen study^{8,10-13}. The first

generation s-DBT is current undergoing clinical trials at the University of North Carolina Cancer Hospital.

There are some limitations of the 1G s-DBT system. Those include limited tube flux, limiting x-ray energy, and the maximum angular span of 30°. Limited tube flux results in patient compression thickness limitations, as sufficient dose to patients with breast thicknesses over 6.5 cm cannot be delivered in suitable scan times (4 seconds). Patients with large compression thickness can be imaged at longer scan times; however, this is unfavorable as it introduces greater patient motion degrading image quality. Moreover, it does not allow the investigation of dual energy imaging as higher tube flux is required with the use of high and low energy filters. Acquisition geometry parameters such as total angular span, angular coverage, and number of projections are of particular importance in DBT as reconstruction image quality is dependent on these parameters^{14,15}. Previous studies have indicated that an increase angular span coupled with an optimal amount of projection views increases depth resolution^{12,14–16}.

Hypothetically, construction of a new s-DBT system with higher tube flux, and a wider angular span would result in a system capable of decreased image acquisition time, inclusion of patients with thick and dense breast, and increased depth resolution. Here we report the characterization results of the 2nd generation s-DBT system with higher tube flux, higher x-ray energy, and larger angular span. Compared with the 1G s-DBT system it shows significant improvement in spatial resolution, and a reduction in the scanning time for all size patients.

6.2 Methods and Materials

6.2.1 Digital Breast Tomosynthesis systems

Second generation s-DBT system

The 2nd generation s-DBT system (2G s-DBT) was designed to be comparable to the 1st generation system except that the new design has 21 sources compared to 31 on the Gen 1 system, and a larger angular span, 35° versus 28° on the Gen 1 system. The Gen 2 s-DBT system was constructed, and characterized in our labs at UNC. The x-ray output and beam quality were measured. In-plane spatial resolution was quantified by determining the system modulation transfer function (MTF), and the system in-depth resolution was evaluated by means of measuring the artifact spread function (ASF). System MTF and ASF were compared to measurements taken on the 1G s-DBT system (1G s-DBT), and the commercial GE SenoClaire DBT system.

Distributed CNT x-ray source array

The carbon nanotube x-ray source array in 2G s-DBT comprises of 21 linearly distributed x-ray focal spots along 473 mm. At a source to object distance of 745 mm, it provides 35° coverage, see Figure 6.1. The linear distribution of the sources vary to provide an equiangular spacing of 1.6° between neighboring focal spots. Each x-ray source consist of a CNT cathode, gate, an individual tungsten anode with a 16° tilt, and focusing electrodes. The x-ray tube window is made of 0.5 mm Al, which provides a vacuum seal, and also serves as the inherent spectrum filter. Two ion pumps that maintain, and allow for the monitoring of pressure are also attached to the CNT x-ray source array.

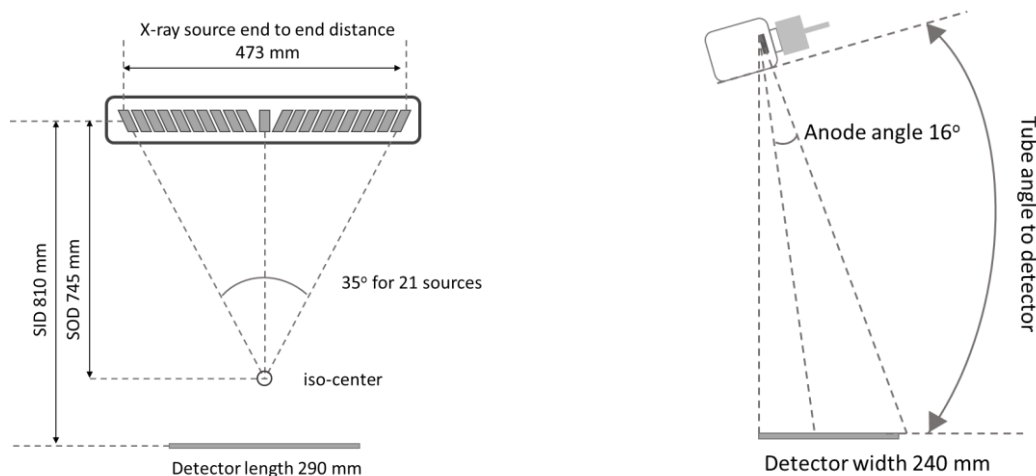


Figure 6.38 Geometry of the 2G s-DBT system (left) front view (right) side view.
Second generation s-DBT system construction

The 2G s-DBT system, as shown in Figure 6.2, was assembled by substituting the original single thermionic x-ray source on the Hologic Selenia Dimensions DBT (Hologic Bedford, MA USA) system with the CNT x-ray source array (XinRay Systems LLC, Research Triangle Park, NC). The CNT x-ray tube is mounted at an 810 mm source to image (detector) distance (SID), and a source to object distance (SOD) of 745 mm. The entire tube is rotated to 6° away from the chest wall as illustrated in Figure 6.1. The CNT x-ray linear source array was electronically incorporated with the Hologic Selenia Dimensions gantry allowing each source to be controlled individually.

The electronic interface comprises of a specially designed and constructed electronic control system (ECS) with an embedded cathode power supply, and an anode power supply (Spellman STR50P6). The ECS allows for manipulation in the number of sources used and its sequence, cathode current, and source exposure time⁸. An in house graphics user interface (GUI) coupled with a LabVIEW program were used to communicate with the detector of the Selenia Dimensions gantry, permitting images to be acquired using the Selenia Dimensions workstation.

The detector for the Selenia Dimensions work station operates in two modes: 2 x 2 binning mode (140 μm pixel size), and full resolution (70 μm pixel size).

System Collimation

The x-ray beams are collimated using an external collimator. The collimator is designed to ensure the x-ray field fully covers the flat panel detector, not extending beyond 2% of the source-imaging-plane distance (SID), along the length and width of the detector, keeping within the Mammography Quality Standards Act and Program (MQSA) regulations. The external collimator was designed specifically for the 2G s-DBT system. It is constructed of 2.5 mm thick stainless steel, spanning the length of the x-ray tube window (500 mm). It contains 21 individual rectangular apertures of fixed dimension, 13.12 mm (scanning) x 10.80 mm (chest wall).

1.1.1 GE Senographe SenoClaire DBT system

The GE SenoClaire DBT system was used for comparing system resolution of the 2nd generation system. This system uses a Mo/Rh target/filter combination with a 100 μm detector pixel size. For the tomosynthesis acquisition, the system takes 9 projection images over a 25° angular span. The GE system uses a hybrid reconstruction method, adaptive statistical iterative reconstruction (ASIR).

6.3 X-ray output and beam quality

The output and beam quality of the x-ray source array were measured for the 2G s-DBT system. The radiation entrance dose was measured using a dosimeter (Radcal Accu -Pro 9096) and ion chamber (Radcal 10 \times 6-6 M Mammography Ion Chamber Sensor). The ion chamber was fastened to the underside of the compression paddle, centered in the scanning direction and 4cm away from the chest wall. The paddled was fixed at a height of 4.2 cm. In order to

investigate the x-ray tube potential on the entrance dose, the total accumulated dose was measured for x-ray tube voltages ranging from 20 kVp to 40 kVp in increments of 5 kVp. A constant total exposure of 29.5 mAs was used for the acquisition of all total dose measurements. The entrance dose measurements were repeated three times for each setting. The average of the total accumulated dose for each tube voltage setting was divided by the total exposure to determine the dose rate.

The beam quality x-ray source array was determined by measuring the half value layer (HVL) of aluminum and comparing to the standards set by the Mammography Quality Standards Act Regulations (MQSA). Aluminum alloy sheets of different thicknesses were used as additional filtration, and placed over the mammography probe. Dose measurements were collected three times for each aluminum thickness and the average dose was used in the calculation of the dose rate.

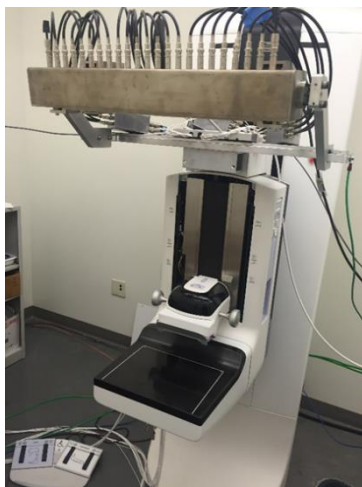


Figure 6. 39 (Left) s-DBT system with integrated CNT x-ray source array (XinRay Systems LLC, Research Triangle Park, NC) with 21 x-ray sources. (Right) GE SenoClaire system that utilizes 9 projection images over a 25° angular span.

6.4 X-ray focal spot size measurement

The pinhole method was used for the measurement of the focal spot size for each source in the array following the European standards (EN 12543-2). A 1.5 mm thick gold phantom, with a 100 μm diameter pinhole was used for the measurement. The pinhole phantom and detector (Hamamatsu C7940DK-02) were mounted to apparatus that allowed for rotation about the iso-center. The pinhole phantom was placed between the source and detector, and carefully aligned with each focal spot before imaging. Images were blank and gain offset corrected, and magnification factors were calculated based on analysis of the projection images.

6.5 Geometry Calibration

The limited amount of data available for the reconstruction of DBT datasets requires an accurate geometry calibration procedure for accurate reconstruction¹⁷. The geometry calibration procedure involves determining the precise position of focal spots relative to the detector¹⁸. Geometric relationships between each source and its relative position to the detector were determined by imaging a calibration phantom which contains metal balls with known geometry. Three sets of projection images were taken with the phantom on the detector, 4cm, and 6cm above the detector respectively. The images were blank and gain offset corrected, then processed through MATLAB for identification of the metal balls and their positions at each of the three phantom position heights. Using the three points for each metal ball detected at their respective heights, lines were projected to determine the point of intersection. Due to the uncertainty in the determining the orientation of the projected lines, there are numerous points of intersection. To determine the coordinates of the focal spot based on projection lines, an average of the points of intersection can be taken. However, using average coordinates introduce large errors because of this uncertainty in orientation. As a means to improve the accuracy of the geometry calibration

method, a statistical model based optimization method was employed to determine the coordinates of each source relative to the center of the detector in 3D space^{19,20}.

For the z coordinates of the focal spot, magnification factors for the known distance between the steel balls in top and the bottom plane of the phantom were used to determine the SID distance for each focal spot²⁰.

6.6 Image reconstruction

Image reconstructions were conducted using a commercial reconstruction system from Real Time Tomosynthesis (RTT version 3.4.4.38793) (Villanova, PA) and an in house iterative reconstruction package utilizing adapted fan-beam volume reconstruction (AFVR), specifically developed for stationary tomosynthesis systems with linear source arrays. The RTT software package utilizes a filtered back projection method (FBP) method, which is fast and allows for real time reconstruction²¹. The AFVR reconstruction method uses a simultaneous algebraic reconstruction technique (SART) that permit fast iterative reconstruction²².

6.7 System modulation transfer function

The modulation transfer function is the spatial frequency response of the imaging system, which is indicative of the systems resolution characteristics. The resolution of an x-ray imaging system is the capability of this system to distinguish objects that are close together. The most widely accepted, and established measure of determining the spatial resolution of a medical x-ray imaging system is the modulation transfer function (MTF)^{23,24}. In this study, the MTF was measured using a slightly slanted (approximately 2° in the direction perpendicular to the chest wall) MTF phantom parallel to the plane of the detector. The MTF phantom consist of two 50 µm tungsten wires orthogonal to each other. The wires in the phantom images were used to sample multiple line spread functions (LSFs) , which were transformed into a single oversampled

LSF using the calculated angle of slant of the wire perpendicular to the measured direction ²⁵.

The oversampled LSF was then fitted to a Gaussian function for removal of noise, and the MTF calculated by taking the discrete Fourier transform of the fitted Gaussian. As the figure of merit, the corresponding frequency at 10% of the MTF was taken as the in-plane resolution.

6.7.1 Projection images MTF

The central projection images (source 8 and 11 for 1st and 2nd s-DBT, and 0° for commercial DBT systems) were analyzed for each DBT system. In each case, the section of the wire in the central region, 4 cm away from the chest wall was used to generate the LSF. For comparison between the s-DBT systems and the commercial DBT systems, only the scanning direction was analyzed. For the 2G s-DBT system, the MTF at different compression heights in both scanning and chest wall directions were analyzed.

6.7.2 Reconstructed in-focus plane MTF

No post processing filters were applied upon reconstruction. The reconstructed in-focus slice for the 40 mm compression thickness was analyzed for system spatial resolution in the scanning direction. The LSF was generated for the wire perpendicular to the scanning direction, in the central region of the breast paddle, and 4 cm away from the chest wall. For the GE system, the reconstructed data of the phantom was not available, therefore it was left out of the system MTF analysis.

6.8 Phantom imaging

For image quality evaluation, an American College of radiology (ACR) mammography accreditation phantom (CIRS Model 015) was imaged and reconstructed into tomosynthesis slices. The ACR phantom contains of aluminum oxide (AL₂O₃) specks ranging from 0.54 to 0.16

mm in diameter, masses ranging from 2 to 0.25 mm in thickness, and nylon fibers that range from 1.56 to 0.4 mm in diameter. The projection images were acquired at 30 kVp and a total entrance dose of approximately 580 mR for both s-DBT systems. The automatic exposure control (AEC) was used when imaging with the GE SenoClaire DBT, and Hologic Selenia Dimensions system.

6.9 Artifact spread function

In tomosynthesis, the limited number of projection views coupled with the limited angular span results in unavoidable image artifacts²⁶. The image artifacts arise from blurring of objects in and out of focus planes, and the degree to which blurring occurs is indicative of the depth resolution of the DBT system. This is quantified by measuring the artifact spread function (ASF) which is defined as the ratio between the contrast of the object out of the focus plane, to that of the respective object in the focal plane^{26,27}. For the ASF measurement of the 2nd generation system, the ACR phantom was imaged using 21 projections over a 35° angular span and reconstructed. The current system configuration for the 1st generation system was used for this measurement. The ASF was then calculated using the set of six largest aluminum oxide specks (0.54 mm diameter) in the ACR phantom used to simulate MCs. It was calculated by measuring the contrast between the object and background for the region of interest for every reconstructed slice^{28,29}. Calculation of the ASF is given by the equation:

$$ASF(z) = \frac{\max[\mu_{mc}(z)] - \mu_{bkg}(z)}{\mu_{bkg}(z)} \quad (6.21)$$

Where the “ $\max[\mu_{mc}(z)]$ ” is the maximum pixel value of the region of interest (ROI) for the slice located at z , and $\mu_{bkg}(z)$ is the average value of the background pixels of the ROI for the slice. The data was then fitted to a Gaussian and the full width half maximum (FWHM) was used as the measure of z -axis resolution¹².

6.10 Results

6.10.1 CNT x-ray source array characterization

The transmission rates, and focal spot size measurements were investigated for the 2G s-DBT system. A total tube potential of 30 kVp was used for the characterization of the CNT sources. The measured cathode and anode current waveform from each source was captured with an oscilloscope, and a summary is plotted in figure 6.3. The results indicate that all CNT sources can output 43 mA of anode current consistently from source to source. The calculated transmission rates were consistent for all sources having an average value of $68 \pm 4\%$. All acquired projection images in this study used an output of 29.33 ± 1.98 mA tube current, varying the pulse width of the sources to achieve the desired x-ray exposure (mAs).

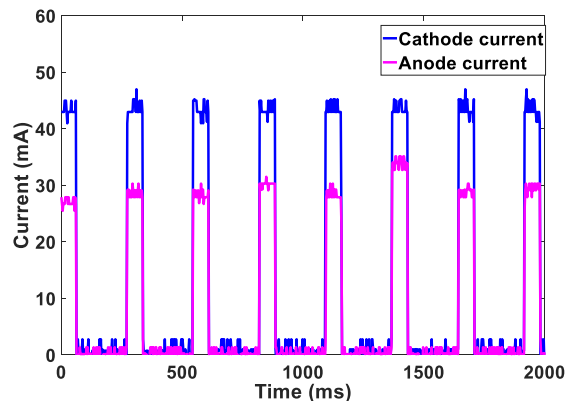


Figure 6.40 The cathode current waveform and anode current waveform for a 60 ms pulse width from 8 different CNT sources. The results indicate that with ECS all CNT sources can consistently produce 43 mA cathode current across all sources.

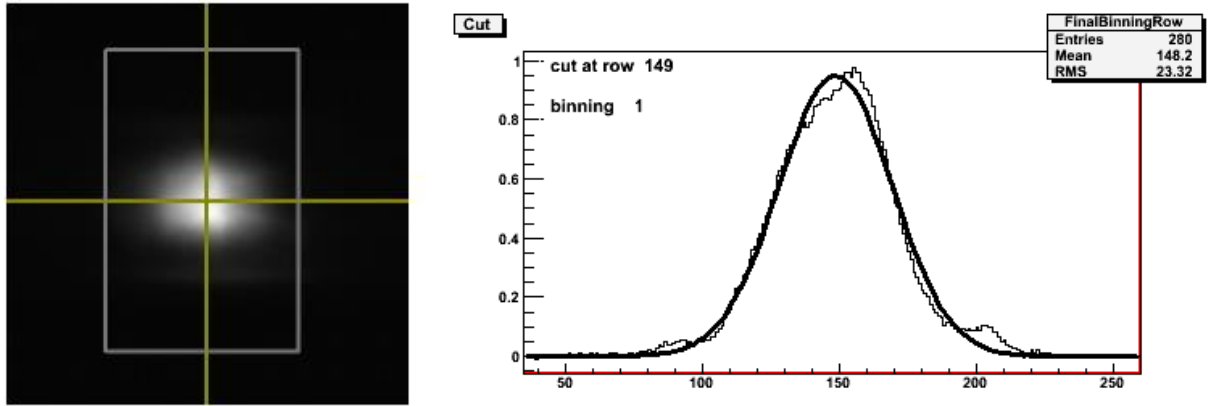


Figure 6.41 Focal spot measurement using a pinhole phantom. (Left) A pinhole image acquired at 40 kVp. (Right) Shows the normalized intensity profile of the length of the pinhole image.

The focal spot size was determined by analysis of the pinhole images generated from the respective sources. Figure 6.4(a) shows a pinhole image from a source. Normalized intensity profiles were generated and fitted to a 2D Gaussian distribution across the length and width of the ROI as shown in Figure 6.4(b). The 20% cut of the Gaussian distribution was used as the focal spot size. Figure 6.5 shows the experimentally measured focal spot sizes for the 21 sources. Based on the measurement, the focal spot sizes are consistent from source to source, having an average length of 1.29 ± 0.1 mm and an average width of 1.54 ± 0.15 mm.

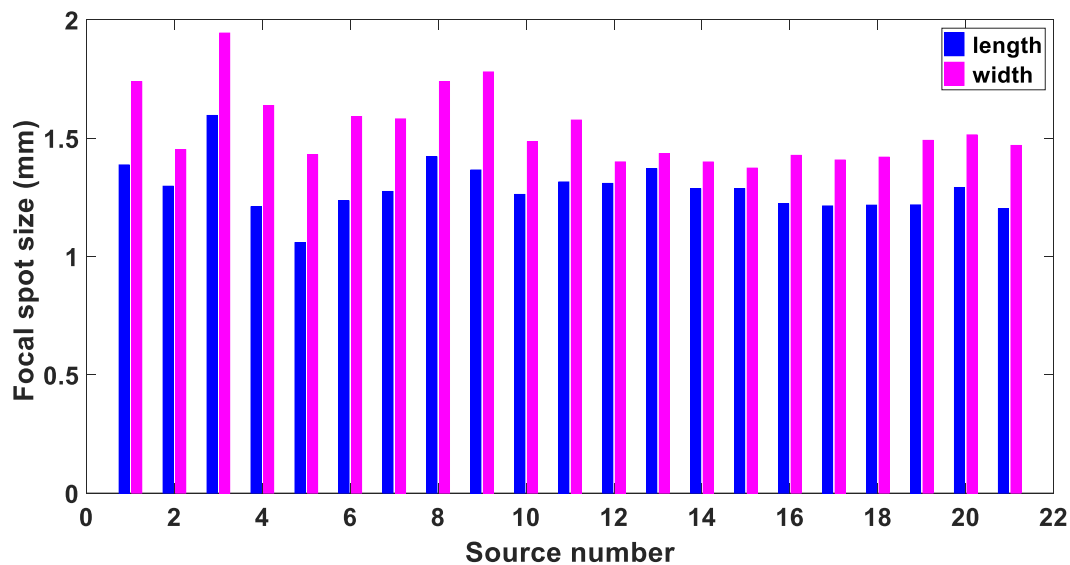


Figure 6.42 Focal spot size measurement of 21 sources in the source array. The results show a good source-to-source consistency.

6.10.2 Beam quality

The spectrum of the x-ray source was measured at the highest operational tube voltage of 49 kVp using a CdTe detector (AMPTEK, Inc., Bedford, Mass.). The measured normalized spectrum at 49 kVp is shown in Figure 6.6 and compared to a simulated spectrum generated with SpekCalc v1.1 for a tungsten anode, 49 kVp tube potential and an Al x-ray window of thickness 0.5 mm. The measured spectra agrees with the simulated spectrum, with respective mean energies at 24.96 keV and 26 keV.

The beam quality of medical x-ray imaging devices are quantified using the first HVL. At a constant total tube potential of 30 kVp and 1.55 mAs per source, the dose rate was measured and plotted against thickness of Al alloy sheets. The first HVL was interpolated from the data and calculated to be 0.45 mm, which is in accordance MQSA's quality standard of 0.33 mm Al for 30 kVp.

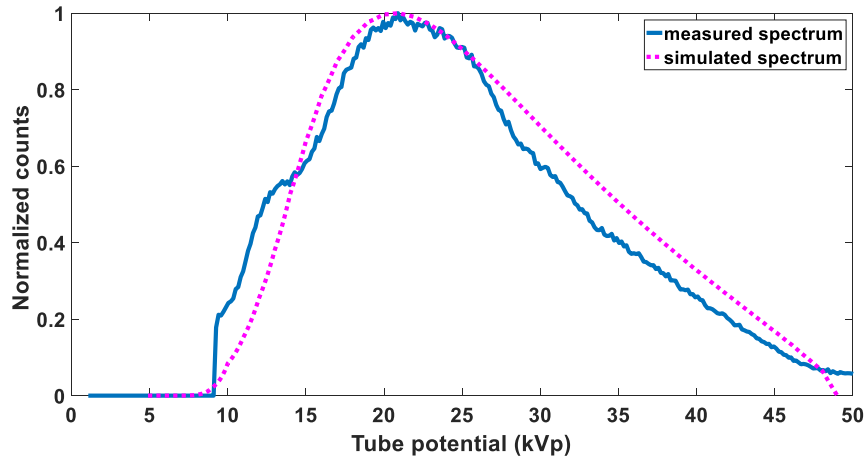


Figure 6. 43 Experimentally measured, and simulated spectra for 49 keV tube potential.

6.10.3 System geometry calibration

Table 6.1 list the geometry calibration results for the x (chest wall), y (scanning direction) and z (SID) coordinates of the focal spots relative to the detector. The measured calibration data for both x, and y directions were fitted to a line to determine how well the focal spots fit its linear design. Figure 6.7(a) shows the raw data and fitted line of the calibration utilizing the optimization method for the x-direction. The fitted linear regression line had a relatively small slope of 0.093 and an R-squared value of 0.77. The small slope is indicative of a slight tilt of the tube in the x-y plane, and the R-squared value suggest that there is a bit of variation between the measured and predicted x-coordinate values. For further investigation, residual analyses comparing the observed and predicted values were conducted and are shown in figure 6.7(b). The random pattern of the residual plot displays the variation of each source from its predicted value. All 21 sources had an average x-coordinate value of 225.57 ± 0.61 mm. The measured y-coordinate calibration data was then used to calculate the inter-angular spacing, and total angular coverage for comparison with its design parameters. Source angles relative to the iso-center were

determined using the calculated average SOD of 744.44 ± 3.33 mm. Figure 6.8(a) displays the raw data and fitted line of the calibration for the y-direction. Based on the focal spots y-coordinates, the angular positions from the center of the detector were determined for each source. An average equiangular spacing of 1.76 ± 0.029 degrees was calculated between sources. Residual angles established from the design parameters are plotted in figure 6.8(b). The largest angular difference measured based on the design criteria was 0.14 degrees, demonstrating that the sources were constructed within 1% error of its angular design specifications.

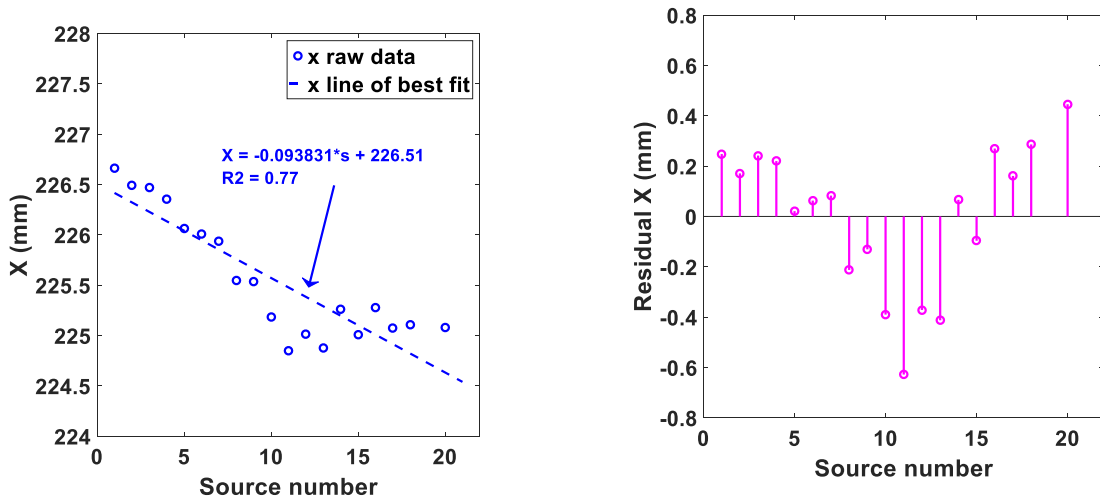


Figure 6.44 Geometry calibration results. (Left) X coordinates of focal spots in the 2G s-DBT source array using the optimization method. (Right) Shows the error of the coordinates from a straight line.

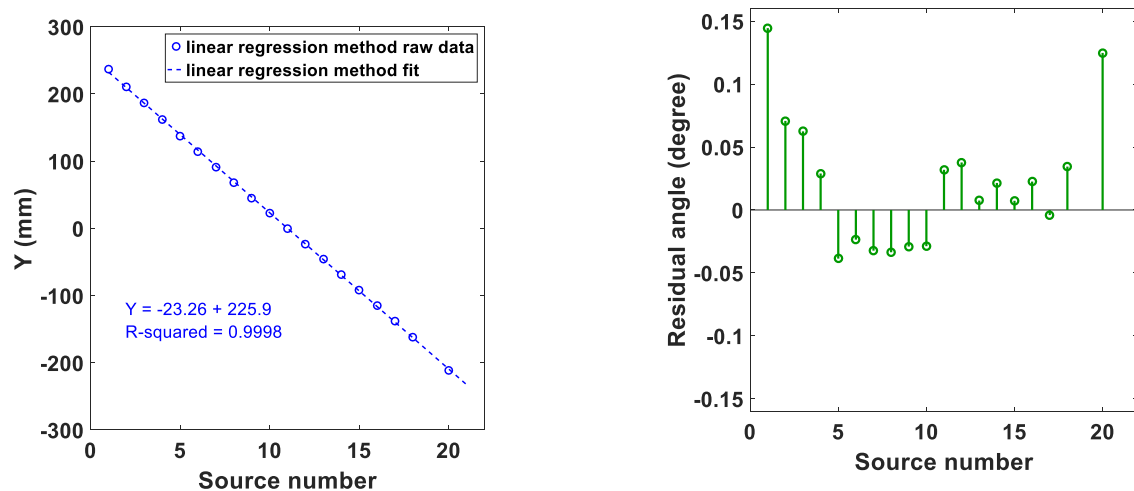


Figure 6.45 Geometry calibration results. (Left) Y coordinates of the focal spots (Right) show the errors in the angular distribution of sources calculated from the y coordinates.

Table 6.11 x-y-z coordinates, and angular distribution of each focal spot in the linear CNT source array relative to the detector.

Source Number	X (mm)	Y (mm)	Z (mm)	Angle from iso-center (degrees)	Design angle (degrees)	Difference from design angle (degrees)
1	226.66	236.79	816.41	17.64	17.50	0.14
2	226.49	210.95	804.41	15.82	15.75	0.07
3	226.47	186.47	809.33	14.06	14.00	0.06
4	226.35	162.03	806.49	12.28	12.25	0.03
5	226.06	137.45	810.19	10.46	10.50	-0.04
6	226.01	114.27	810.47	8.73	8.75	-0.02
7	225.94	90.98	810.80	6.97	7.00	-0.03
8	225.55	67.96	810.00	5.22	5.25	-0.03
9	225.53	45.15	810.19	3.47	3.50	-0.03
10	225.18	22.37	812.68	1.72	1.75	-0.03
11	224.85	-0.41	807.11	-0.03	0.00	-0.03
12	225.01	-23.24	808.56	-1.79	-1.75	0.04
13	224.88	-45.63	807.11	-3.51	-3.50	0.01
14	225.26	-68.69	808.22	-5.27	-5.25	0.02
15	225.01	-91.50	805.87	-7.01	-7.00	0.01
16	225.28	-114.88	808.50	-8.77	-8.75	0.02
17	225.08	-137.92	817.53	-10.50	-10.50	0.00
18	225.11	-162.10	809.33	-12.28	-12.25	0.03
19						
20	225.08	-211.71	806.19	-15.87	-15.75	0.12
21						

Average	225.57 ± 0.61	809.44 ± 3.33	0.02 ± 0.052
---------	-------------------	-------------------	------------------

6.10.4 Radiation dose and system scan time

Dose measurements

Total accumulative radiation entrance dose was measured using the dosimeter at different tube potentials and 1.55 mAs exposure per source. A plot of the entrance dose rate correlation with x-ray tube potential, together with the entrance dose rate of the 1st generation system, and the Selenia Dimensions DBT system for comparison is displayed in Figure 6.9. As observed in the figure, the dose rate of the 2nd generation system diverges from the 1st generation as the tube potential increases. The measurements show an approximate doubling of the average dose rate moving from the 1st generation system to the 2nd generation system.

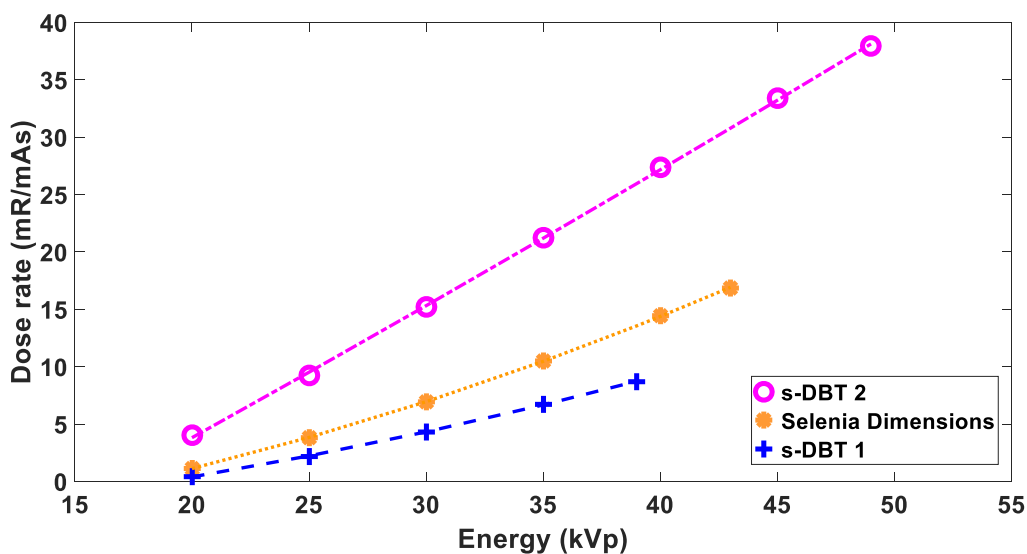


Figure 6.46 Measure entrance dose rate for Hologic DBT system, Gen 1, and Gen 2 s-DBT system

Scan Time

Scan time for the 2G s-DBT system was calculated and compared to the 1st generation system. For s-DBT scan time is dependent on a number of factors. The equation for s-DBT scan time is given by

$$T_{acq} = N_{projection} * (\Delta t_{exp} + \Delta t_{readout}) \quad (6.22)$$

where “ T_{acq} ” is the total acquisition time, “ $N_{projection}$ ” is the number of projection images, “ Δt_{exp} ” is the exposure time per projection, and “ $\Delta t_{readout}$ ” is the detector readout time per projection. The exposure time per view is a function of the required entrance dose, and the x-ray tube current. Keeping the same number of projections constant, total image dose, and tube current constant, the dose rate of the 2nd generation system results in shorter image acquisition times as a result of its higher entrance dose rate.

Table 6.2 list a comparison of image acquisition times between the two s-DBT systems for different compression thicknesses. Total dose, and detector read out time was kept constant for the comparison. The total entrance dose for each compression thickness for the s-DBT systems were matched to the total entrance dose from the Selenia Dimensions system automatic exposure control (AEC) for normal breast (50/50 adipose glandular). In order to keep the imaging time around and under 5 seconds for some compression thicknesses in the clinical trial of the 1st generation system, a compromise was made between the number of projection views and image acquisition time. Based on the table, at a compression thickness of 75 mm for the 1st generation system, scan time is longer than 5 second. These long scan times are unfavorable as patient motion degrades image quality.

Table 6.12 Comparison of imaging times between the 1st and 2G s-DBT systems. The 2nd generation system is capable of measuring all compression thicknesses shown in about 4 seconds.

Thickness	1 st s-DBT no. of sources	Scan time 1st s-DBT	2 nd s-DBT no. of sources	Scan time 2nd s-DBT
10	9	2.40	15	2.20
15	9	2.63	15	2.32
20	13	3.23	15	2.46
25	13	3.61	15	2.53
30	13	3.90	15	2.56
35	15	4.60	15	2.66
40	15	3.78	15	3.00
45	15	4.15	15	3.11
50	15	4.63	15	3.27
55	15	4.42	15	3.53
60	15	4.88	15	3.70
65	15	4.85	15	3.95
70	15	4.84	15	4.20
75	15	5.19	15	4.32
80	15	5.48	15	4.22
85	15	5.86	15	4.20
90	15	6.18	15	4.14

Comparing the 2nd generation system, scan times for all compression thicknesses are around or under 4 seconds. Using the total amount of projections the 1st generation is capable of for comparison (15 projections), the 2nd generation system has a faster imaging time at each thickness, regardless if the 1st generation system used less to reduce scan time. The reduction in scan time would lead to less patient motion, yielding better image quality.

6.10.5 System Resolution

MTF of DBT projection images

The MTF of the central source was analyzed from the respective projection image of the 50 μm tungsten wire phantom for each DBT system. The oversampled LSFs needed for MTF calculation were generated three times for the region of interest (ROI) across the wires to

measure MTF, as illustrated in figure 6.10(a). Figure 6.11 shows the calculated MTF in the scanning direction for the central source for the DBT systems. Using 10% of the normalized MTF (MTF_{10}) intensity as the figure of merit, the 2G s-DBT system has the highest spatial resolution with an 8.3% increase over the 1st generation system at full resolution ($70\ \mu\text{m} \times 70\ \mu\text{m}$ pixel). Both Hologic and GE DBT systems had lower projection $MTFs_{10}$ at 4.7 cycles/mm and 5.7 cycles/mm respectively.

The effect of geometric unsharpness on the height above the detector was determined by comparing MTF_{10} values for the 2G s-DBT projections at different heights in both scanning and chest wall directions (Figure 6.12). The detector was used in full resolution mode for all measurements. In this study, the wired phantom resting on the detector was used as the reference (wire height 10 mm) MTF_{10} . Based on this, a 22% and 23% reduction in projection MTFs were measured in the chest wall and scanning direction respectively, showing no noticeable reduction in resolution of one direction over the other.

6.10.6 In-plane system resolution

The system MTF was measured from the in-focus reconstructed slice of the wire phantom. For both s-DBT systems image acquisition sets, RTT software and our AFVR reconstruction method were employed for reconstruction. The Hologic system reconstruction was done via RTT only. The smallest slice separation of 0.1 mm was chosen for reconstructions done via the RTT software, and 0.2 mm for AFVR reconstructions to minimize z-offset and attain the highest measurable MTF. Figure 6.10(b) shows the oversampled LSF and its respective Gaussian fitted LSF for the highlighted ROI in figure 6.10(a).

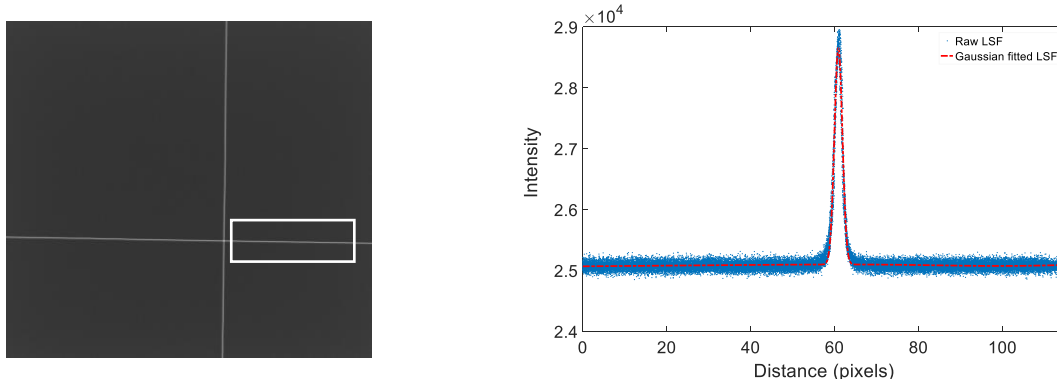


Figure 6.47 (a) A reconstructed in-focus slice of the 50 μm cross wire phantom. The ROI highlighted by the white box illustrates an example of the region used to calculate the MTF. (b) The accompanying LSF of the horizontal tungsten wire and the Gaussian-fitted LSF.

Figure 6.13 displays a plot of the full resolution 2G s-DBT system for both the FBP and AFVR reconstruction methods, and the Selenia Dimensions system. Comparing MTF_{10} in the scanning direction, both reconstruction methods resulted in higher system MTFs for the 2G s-DBT system than the Selenia Dimensions system. The AFVR reconstruction method yielded an MTF of 7.7 cycles/mm performing 1 cycle/mm better than the FBP method. In comparing both systems with the same FBP reconstruction method, the 2G s-DBT system has a system MTF of 6.7 cycle/mm, indicative of an over 50% increase of the in-plane spatial resolution.

Table 6.3 list the experimentally measured MTFs of the DBT systems. The full resolution 2nd generation system had a higher system MTF than all systems in the relative categories. The 2nd generation system utilizing the binned detector mode (140 μm) had higher projection MTFs than both commercial DBT systems, and a higher system MTF value than the Selenia Dimensions employing the same FBP reconstruction.

Table 6.13. Experimentally measured MTF for the 1st and 2G s-DBT systems in the scanning direction. The 1st generation system is currently configured to operate only in full resolution mode, therefore measurements at pixel size 140 μm were unavailable.

Detector pixel size	Selenia	GE	1st gen s- DBT	2nd gen s-DBT	
	Dimensions 140 μm	SenoClaire 100 μm	70 μm	140 μm	70 μm
Projection MTF ₁₀ (cycles/mm)	4.7	5.66 ± 0.12	7.2	6.4	7.8
System MTF ₁₀ FBP (cycles/mm)	4.0		5.58 ± 0.21	4.5 ± 0.20	6.6 ± 0.11
System MTF ₁₀ AFVR (cycles/mm)			6.68 ± 0.20	5.4 ± 0.56	7.7 ± 0.11

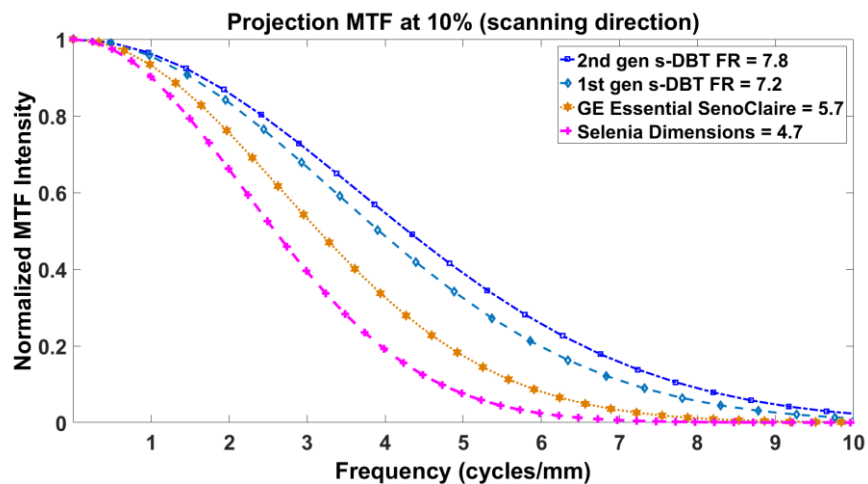


Figure 6.48. Projection MTFs of the two FDA approved devices and both s-DBT systems.

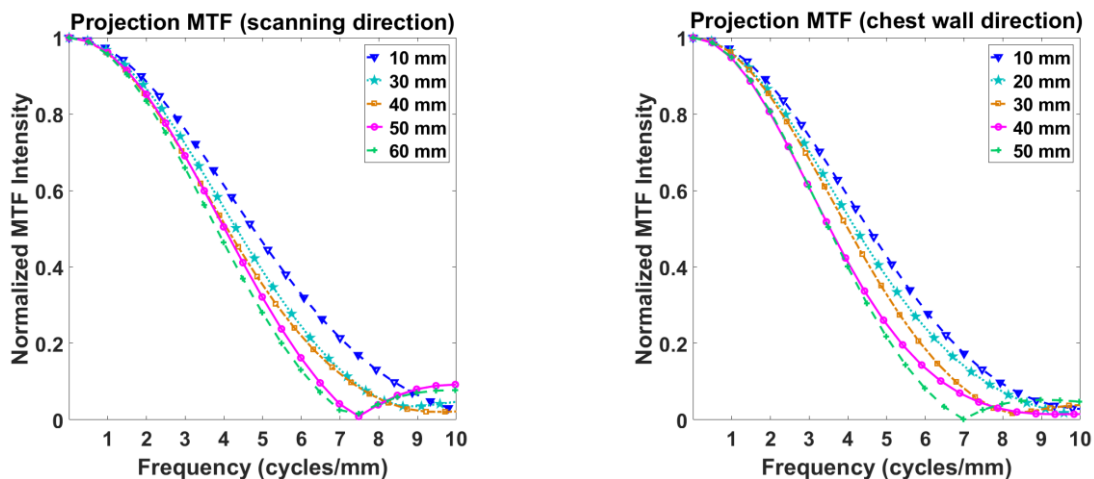


Figure 6.49. MTF measured from the central source projection for different heights above the detector for the Gen 2 s-DBT system (a) scanning direction (b) chest wall direction.

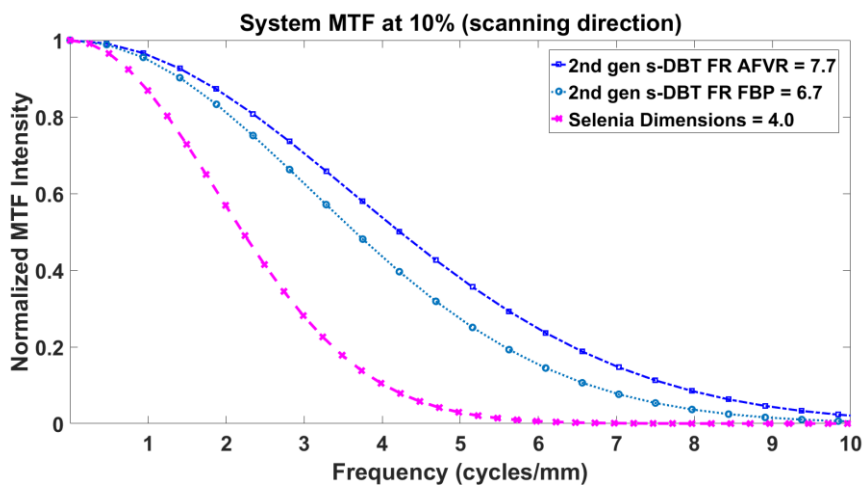


Figure 6.50 The system MTFs of the Selenia dimensions system compared to the 2nd generation system utilizing the AFVR and FBP reconstruction methods.

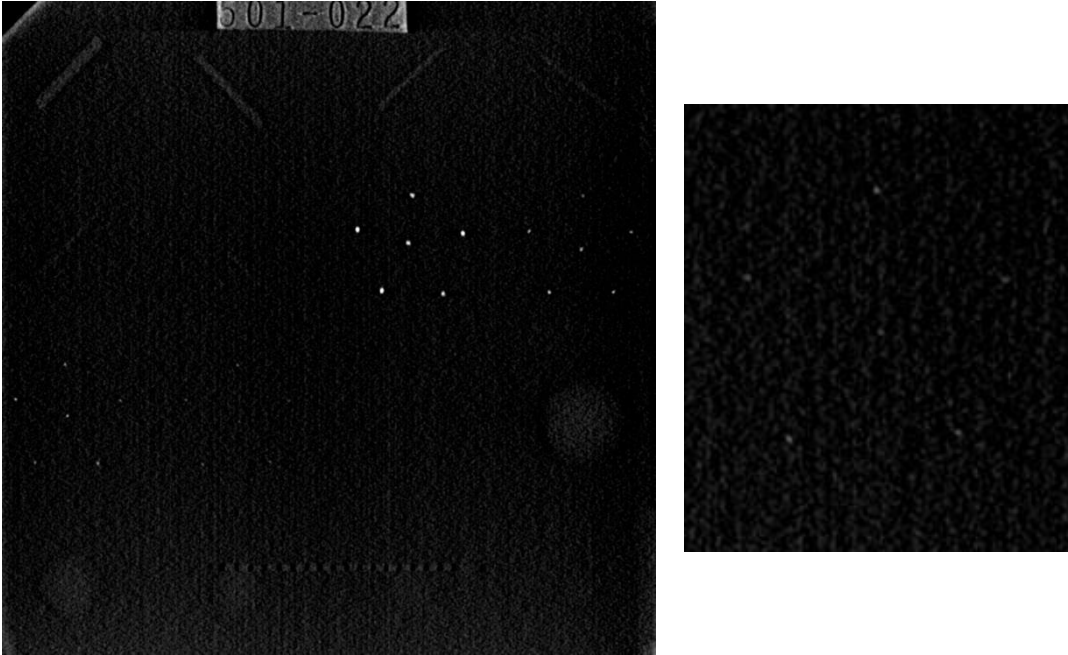


Figure 6.51. (Left) ACR phantom imaged using the 2nd generation DBT system. (Right) Magnified view of 4th group of Al₂O₃ specks, each of the 6 specks are visible

6.10.7 In-depth resolution as measured by artifact spread function

A reconstructed in-focus slice for the ACR phantom reconstructed using the AFVR method is shown in figure 6.14(a). Though difficult to view in the figure, on a suitable screen, 5 fibers, 4 speck groups, and 4 masses can be seen. A magnified image of the fourth speck group is shown in figure 6.14(b), where each of the six 0.24 mm AL₂O₃ specks are visible.

The artifact spread function was measured using the largest aluminum oxide specs group (0.54 mm) for both the 2G s-DBT and the GE DBT system. For the 2nd generation system, both reconstruction methods were investigated, and the Gaussian fitted ASF as a function of slice depth is displayed in figure 6.15(a) for both reconstruction methods. The FWHM of the fitted Gaussian ASF was used to quantify the in-depth resolution for the system, resulting in an average in-depth resolution of 2.35 ± 0.25 mm for AFVR and 2.84 ± 0.3 mm for FBP reconstruction. Previous measurements comparing the angular span to the ASF for the first

generation system yielded a FWHM ASF of 4.3 mm¹². The decrease in FWHM of the ASF is expected as depth resolution is dependent on total angular coverage. The difference in the ASF between the reconstruction methods for the 2nd generation system show that the ASF is also dependent on the reconstruction method. The AFVR reconstruction method produced the narrowest FWHM ASF, with a 17% decrease from the FBP method. Figure 6.16 is a visual comparison of a 0.54 mm Al₂O₃ speck in focus and at different slice depths for both reconstruction methods. Based on the images it can be discerned that the slices at 1 mm and 2mm for the AFVR method are slightly sharper than those from reconstructed using FBP.

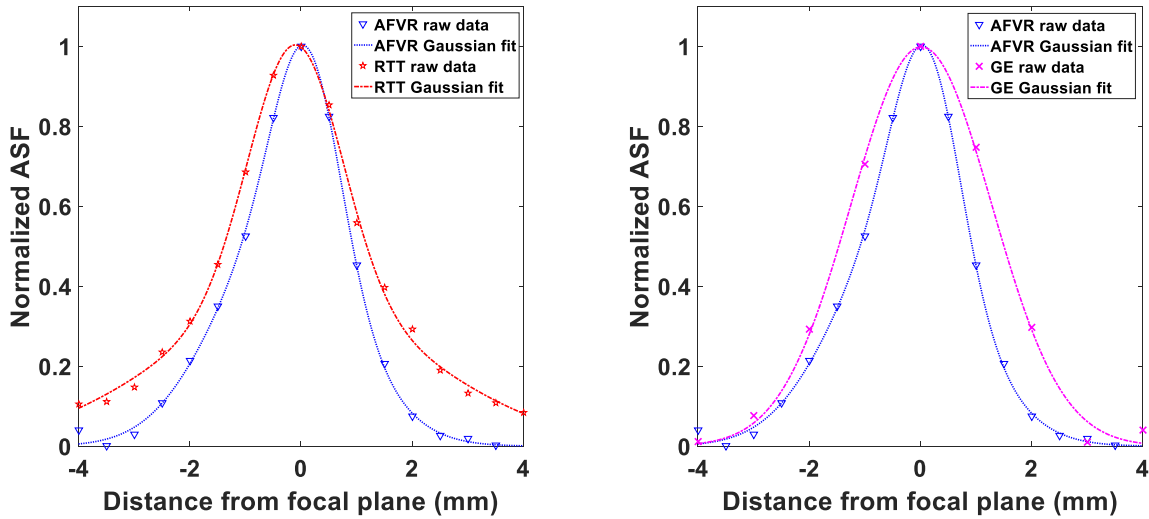


Figure 6.52. (Left) A magnified view of the 0.54 mm speck cluster in the ACR phantom used for ASF analysis. Plot of the ASF for a 35° angular span for AFVR and FBP reconstruction methods. Both the raw data and the fitted data are shown. The AFVR reconstruction method resulted in a marginal decrease of the ASF.

The GE system ASF was calculated and compared to the ASF for the AFVR reconstructed image from the 2nd generation system (figure 6.15(b)). As expected, a slightly narrower ASF is obtained for the 2G s-DBT system as it has a wider angular span. The FWHM of the ASF for the GE system was 2.89 ± 0.1 mm.

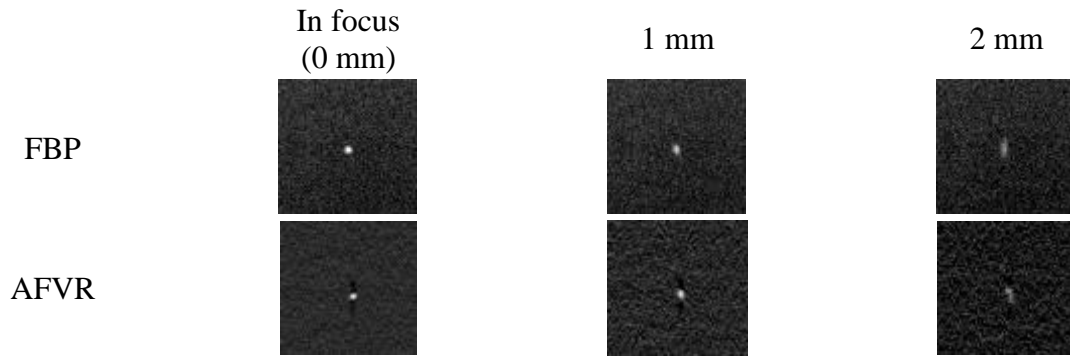


Figure 6.53 Shows a three slice comparison of one of the 0.54 mm specks in the ACR phantom for both AFVR and FBP reconstruction methods. At each slice depth, the FBP slices look a bit blurrier than the slices from AFVR method.

6.11 Discussion

The objective of this study was to construct a 2G s-DBT system with increased tube flux to include patients with thick and dense breast, decreased imaging time, and increased depth resolution. The system was constructed and characterized to investigate whether the system performance matched its design criteria. The design of this system was based on previous studies that showed improved resolution of an s-DBT system over a CM DBT system¹². System resolution and performance were compared to the 1st generation system as well as FDA approved commercial systems.

6.11.1 X-ray tube characterization

The reduction of the Al window from 1 mm to 0.5 mm from the 1st generation system to the 2nd was responsible for the increase in measured entrance dose rate. Compared to the 1st system, the 2nd generation is capable of delivering more than adequate x-ray dosage as used in FDA approved DBT systems. The more than two fold increase in the entrance dose rate significantly reduced the scan time for the 2G s-DBT system, offering faster or equivalent scanning times for some patient compression thicknesses compared with FDA approved systems.

For example, the for the average compression thickness of 45 mm, the Selenia Dimension, and GE systems take ≈ 4 and ≈ 7 seconds respectively, whereas for the 2G s-DBT system, the scan time is ≈ 3 seconds. This reduction in image acquisition time is favorable as it minimizes the effect on patient motion, improving image quality^{30,31}. A further reduction in the detector readout out time or higher tube output power further reduces scan times. In addition, it overcomes the limitations of the 1st generation, namely imaging patients with very thick, and dense breast in a clinically acceptable time. The reduced x-ray window thickness provides sufficient beam filtration as measured by the HVL for the designed operating kVp.

6.11.2 DBT projection MTF and system MTF

The in-plane resolution as quantified by the system MTF depends primarily on the effective focal spot size of the x-ray source, the detector pixel size, and reconstruction method^{31,32}. In conventional DBT systems, there is a reduction in system MTF in the direction of motion due to tube movement. This was apparent in measuring the projection MTFs in the scanning directions for both commercial DBT systems. The stationary x-ray focal spots for the s-DBT systems resulted in higher MTFs, as there is no degradation due to motion. The higher projection MTF for the 2nd generation system is indicative of a smaller effective focal spot size, and this may be attributed to the increase in the SID over the 1st generation. The step and shoot modality employed by the GE systems resulted in a higher projection MTF than Hologic's system as there is no translation of the tube during image acquisition. This reduces blurring in the scan direction. The x-ray focal spot in the Hologic system travels a larger path than the x-ray focal spot for the GE system during image acquisition, which accounts for the greater resolution reduction.

The projection MTF against the height above the detector was investigated as a means to demonstrate that no one direction suffers significantly more resolution degradation as observed in conventional systems. Rodriguez-Ruiz et al.³³ demonstrated the greater reduction in resolution of the scanning direction compared to the chest wall direction for the Hologic system. A 60% reduction in resolution in the direction of tube travel and 40% in the chest wall direction was measured from the reference MTF at 45 mm. This non-uniform degradation is indicative of the anisotropy of the effective focal spot³³. However, for the 2G s-DBT system, equivalent resolution degradation was observed in both directions. The burring in the scanning direction is not compounded by motion blur, synonymous to the chest wall direction, yielding in similar degradation.

As expected, a higher system in-plane resolution was observed with higher projection MTFs, and as a consequence the 2nd generation system had the highest system in-plane resolution. Reconstruction methods also influence in-plane resolution as observed in the 2nd generation system. Compared with FBP, the AFVR method resulted in a notable increase in the system in-plane resolution compared to the FBP method as suggested by the 2nd generation system MTF. This result is in accordance with previous studies that have indicated iterative reconstruction processes result in sharper images with better contrast than those reconstructed with a FBP method³⁵. This improvement of system in-plane resolution in conjunction with the AFVR reconstruction method could be beneficial in the clinical setting, as increased spatial resolution increases the visibility of some microcalcifications. It is important to note that though our AFVR reconstruction method is much faster than current iterative methods, the computation time is still significantly longer than FBP methods, rendering it impractical for clinical applications^{22,35}. However, together with a fully optimized computer, the 2nd generation system

utilizing the AFVR reconstruction method may result in overall better image resolution making it a viable option for clinical application.

6.11.3 Artifact spread function (ASF)

Since no mechanical motion of the x-ray tube is required, image acquisition time is independent of angular coverage. This gives the s-DBT system a unique advantage, as it can capitalize on increased depth resolution without increasing imaging time. The image blur at different depths is as a result of partial sampling due to the system geometry. The 2nd generation system, having a larger angular span than the 1st generation, and the GE system, has a better depth resolution as expected, since more data is collected in the projection space³⁶. These results are synonymous to prior studies that investigated the effect of angular span on depth resolution^{35,36}. It was also observed that the reconstruction method has a marginal effect on the ASF, signifying that this method performs better in the suppression of out of plane artifacts. This increase, would serve to further decrease tissue overlap, making objects become more conspicuous.

The overall improvement of in-plane, and depth resolution of the 2nd generation system coupled with the faster image acquisition time should improve breast tomosynthesis imaging quality. This 2nd generation system incorporates the advantages of both CM and SSM DBT systems, in that it is capable of fast imaging similar to CM without focal spot blur do to tube motion as in SSM. The faster imaging, improved in-plane resolution, and depth resolution may be valuable in the reduction of false positives, and false negatives, as improved resolution should translate into better patient diagnosis.

6.12 Conclusion

The 2nd generation stationary digital breast tomosynthesis system using a new distributed CNT x-ray source array was built and evaluated. The system characterization showed that it had a higher tube flux than the 1st generation, which decreased the image acquisition time. The system MTF showed a marginal increase in the system in-plane image resolution over the 1st generation system, which has already shown an increase in spatial resolution compared to a continuous motion DBT system. System ASF confirms that a wider angular span improves system depth resolution, without compromise to imaging acquisition time. The characterization of 2G s-DBT system implies improved overall system spatial resolution of the 2nd generation system compared to the 1st. With these improvements, the next logical step is to evaluate this 2nd generation S-DBT in a clinical trial.

6.13 REFERENCES

- ¹ N. Houssami, K. Lång, D. Bernardi, A. Tagliafico, S. Zackrisson, and P. Skaane, *The Breast* **26**, 119 (2016).
- ²*Digital Breast Tomosynthesis* (2010).
- ³ N. Houssami, P. Macaskill, D. Bernardi, F. Caumo, M. Pellegrini, S. Brunelli, P. Tuttobene, P. Bricolo, C. Fantò, M. Valentini, and S. Ciatto, *Eur. J. Cancer* **50**, 1799 (2014).
- ⁴ A. Tagliafico, G. Mariscotti, M. Durando, C. Stevanin, G. Tagliafico, L. Martino, B. Bignotti, M. Calabrese, and N. Houssami, *Eur. Radiol.* **25**, 9 (2015).
- ⁵ M.J. Michell, A. Iqbal, R.K. Wasan, D.R. Evans, C. Peacock, C.P. Lawinski, A. Douiri, R. Wilson, and P. Whelehan, *Clin. Radiol.* **67**, 976 (2012).
- ⁶ S. Destounis, R. Morgan, and A. Arieno, *Curr. Radiol. Rep.* **4**, 15 (2016).
- ⁷ J.S. Nelson, J.R. Wells, J.A. Baker, and E. Samei, *Med. Phys.* **43**, 2538 (2016).
- ⁸ X. Qian, A. Tucker, E. Gidcumb, J. Shan, G. Yang, X. Calderon-Colon, S. Sultana, J. Lu, O. Zhou, D. Spronk, F. Sprenger, Y. Zhang, D. Kennedy, T. Farbizio, and Z. Jing, *Med. Phys.* **39**, 2090 (2012).
- ⁹ G. Yang, X. Qian, T. Phan, F. Sprenger, S. Sultana, X. Calderon-Colon, B. Kearse, D. Spronk, J. Lu, and O. Zhou, *Nucl. Instrum. Methods Phys. Res. A.* **648**, S220 (2011).
- ¹⁰ A.W. Tucker, J. Calliste, E.M. Gidcumb, J. Wu, C.M. Kuzmiak, N. Hyun, D. Zeng, J. Lu, O. Zhou, and Y.Z. Lee, *Acad. Radiol.* **21**, 1547 (2014).

- ¹¹ J. Calliste, A.W. Tucker, E. Gidcumb, C.M. Kuzmiak, J. Lu, O.Z. Zhou, and Y.Z. Lee, in *SPIE Med. Imaging Phys. Med. Imaging* (2015), p. 941228.
- ¹² A.W. Tucker, J. Lu, and O. Zhou, *Med. Phys.* **40**, 031917 (2013).
- ¹³ A.W. Tucker, Y.Z. Lee, C.M. Kuzmiak, J. Calliste, J. Lu, and O. Zhou, in *SPIE Med. Imaging*, edited by B.R. Whiting and C. Hoeschen (International Society for Optics and Photonics, 2014), p. 903316.
- ¹⁴ H.-S. Park, Y.-S. Kim, H.-J. Kim, J.-G. Choi, and Y.-W. Choi, *Clin. Imaging* **37**, 993.
- ¹⁵ I. Sechopoulos and C. Ghetti, *Med. Phys.* **36**, 1199 (2009).
- ¹⁶ H.-S. Park, Y.-S. Kim, H.-J. Kim, Y.-W. Choi, and J.-G. Choi, *J. Radiat. Res.* **55**, 589 (2014).
- ¹⁷ X. Wang, J.G. Mainprize, M.P. Kempston, G.E. Mawdsley, and M.J. Yaffe, *SPIE Med. Imaging Phys. Med. Imaging* **6510**, 65103B (2007).
- ¹⁸ X. Li, Z. Da, and B. Liu, *Med. Phys.* **37**, 3844 (2010).
- ¹⁹ J. Shan, P. Chtcheprov, A.W. Tucker, Y.Z. Lee, X. Wang, D. Foos, M.D. Heath, J. Lu, and O. Zhou, *Station. Chest Tomosynthesis Using a CNT X-Ray Source Array* **81**, 86680E (2013).
- ²⁰ J. Shan, (2015).
- ²¹ J. Kuo, P.A. Ringer, S.G. Fallows, P.R. Bakic, A.D.A. Maidment, and S. Ng, in *SPIE Med. Imaging*, edited by N.J. Pelc, E. Samei, and R.M. Nishikawa (International Society for Optics and Photonics, 2011), p. 796116.
- ²² G. Wu, C. Inscoe, J. Calliste, Y.Z. Lee, O. Zhou, and J. Lu, in *SPIE Med. Imaging*, edited by C.

Hoeschen, D. Kontos, and T.G. Flohr (International Society for Optics and Photonics, 2015), p. 94123J.

²³ A. Kuhls-Gilcrist, A. Jain, D.R. Bednarek, K.R. Hoffmann, and S. Rudin, *Med. Phys.* **37**, 724 (2010).

²⁴ A.L.C. Kwan, J.M. Boone, K. Yang, and S.-Y.Y. Huang, *Med Phys* **34**, 275 (2007).

²⁵ H. Fujita, D.-Y. Tsai, T. Itoh, K. Doi, J. Morishita, K. Ueda, and A. Ohtsuka, *IEEE Trans. Med. Imaging* **11**, 34 (1992).

²⁶ Y.-H. Hu, B. Zhao, and W. Zhao, *Med. Phys.* **35**, 5242 (2008).

²⁷ Y. Zhang, H.-P. Chan, B. Sahiner, J. Wei, M.M. Goodsitt, L.M. Hadjiiski, J. Ge, and C. Zhou, *Med. Phys.* **33**, 3781 (2006).

²⁸ T. Wu, R.H. Moore, E. a Rafferty, and D.B. Kopans, *Med. Phys.* **31**, 2636 (2004).

²⁹ B. Zhao, J. Zhou, Y.-H. Hu, T. Mertelmeier, J. Ludwig, and W. Zhao, *Med. Phys.* **36**, 240 (2009).

³⁰ B. Ren, C. Ruth, T. Wu, Y. Zhang, A. Smith, L. Niklason, C. Williams, E. Ingal, B. Polischuk, and Z. Jing, in *SPIE Med. Imaging*, edited by E. Samei and N.J. Pelc (International Society for Optics and Photonics, 2010), p. 76220B.

³¹ B. Ren, C. Ruth, J. Stein, A. Smith, I. Shaw, and Z. Jing, in *Med. Imaging*, edited by M.J. Flynn (International Society for Optics and Photonics, 2005), pp. 550–561.

³² M.A. Helvie, *Radiol. Clin. North Am.* **48**, 917 (2010).

³³ A. Rodríguez-Ruiz, M. Castillo, J. Garayoa, and M. Chevalier, *Phys. Medica* **1** (2016).

³⁴ S. Xu, J. Lu, O. Zhou, and Y. Chen, Med. Phys. **42**, 5377 (2015).

³⁵ I. Sechopoulos, Med. Phys. **40**, 014302 (2013).

³⁶ A.S. Chawla, J.Y. Lo, J.A. Baker, and E. Samei, Med. Phys. **36**, 4859 (2009).

CHAPTER 7: Feasibility of Contrast Enhanced Imaging with s-DBT

7.1 Motivation for s-DBT Contrast Enhanced Imaging

As previously mentioned in chapter 3, contrast enhanced digital mammography has been shown to provide a promising alternative modality for the early detection of suspicious lesions, especially in patients with high percentages of fibroglandular tissue, or dense breast¹. It is based on the principal that rapidly growing tumors have an increased blood (neovascularity) supply to support its growth (tumor angiogenesis), which causes the accumulation of contrast agent in such areas. Through effective uptake of the contrast agent in the lesion, active tissue growth may be highlighted showing the presence of malignant tissue. This technique effectively removes the background tissue by the exploitation of the differential attenuation characteristics of breast tissue and the contrast agent². Though this technique has shown to improve mammographic lesion conspicuity, due to the superimposition of tissue, there may still be unfavorable impact on lesion conspicuity, reducing sensitivity of this modality³. Since DBT increases lesion conspicuity, and provides localization information, coupling the use of a contrast agent with DBT into a single modality would potentially integrate the benefits of both techniques. Initial studies have shown the improved lesion morphology, and vascular information obtained by contrast enhanced DBT^{3,4}. Of particular interest is the potential to obtain contrast agent kinetics, which provides further information for lesion characterization comparable to dynamic contrast enhanced breast magnetic resonance imaging (CE-MRI)⁵. Though CE-MRI continues to be the most sensitive diagnostic imaging technique for breast lesions, CE-DBT is an ideal candidate for

diagnosis as this would provide a cheaper alternative to MRI procedures, providing similar kinetic information^{3,5}.

In CE-DBT, two methods are employed: temporal subtraction (TS), and dual energy (DE) subtraction. TS CE-DBT involves the acquisition of projection images pre-, and one or more acquisitions post-contrast administration using a spectrum with energies above the iodine k-edge (33.16 keV). Pre- and post- contrast DBT projection images are then logarithmically subtracted, yielding iodine enhanced images prior to reconstruction. For DE CE-DBT, projection images are acquired post-contrast using a LE and HE energy pair that closely brackets the iodine k-edge. The iodine enhanced images are then produced by a weighted logarithmic subtraction of the respective LE and HE projection images before reconstruction. Each CE-DBT method has its advantages and disadvantages. TS has shown to be highest in sensitivity as complete anatomical cancellation can be achieved. However, significant motion, resulting in registration artifacts arising out of the long imaging times. With DE-DBT, complete cancellation of the anatomical background is not possible, leading to a decrease in its sensitivity. Specifically with the HE acquisition, the diminished visibility and quantification of iodine due to the effect of scatter has been previously reported⁶. Conversely, registration artifacts are minimized as image pairs can be taken within rapid succession, resulting in improved registration⁷. Iodine detectability, and registration artifacts are specifically important in the estimation of iodine quantification.

Though CE-DBT shows promise to improve lesion conspicuity, it is still bounded by the inherent limitations of DBT. The added advantages of s-DBT such as, no motion blur, and rapid imaging times, can be further exploited in improving CE-DBT. Coupling s-DBT with contrast enhancement will further enhance spatial resolution of CE-DBT images by negating motion blur,

and reducing imaging times for both TS and DE CE s-DBT, resulting in less patient motion, and registration artifacts. Also, there is the prospect of enhancing interleaved acquisition as there is no motion between HE and LE image pairs, which may lead to better registration than current interleaved CE-DBT methods⁸.

The purpose of this study is to investigate the feasibility of both TS and DE CE s-DBT considering the system parameters. The specific work includes: (i) spectra simulations for determining suitable spectra for TS and DE imaging and (ii) phantom experiments to evaluate the detectability and quantification of iodine for both TS and DE CE s-DBT coupled with a specialized scatter correction technique. The technique involves obtaining an angle, and object specific scatter map using a specially design primary sampling device (PSD)⁹.

7.2 Materials and Methods

7.2.1 Temporal Subtraction

In temporal subtraction, the image acquisition process involves an image taken prior to the contrast agent administration and after. After image acquisition, the logarithmic subtraction of the pre contrast image from the post contrast image is performed resulting in mostly the iodinated region of image. Figure 7.1 is a schematic representation of x-ray transmission for pre- and post-contrast agent administration.

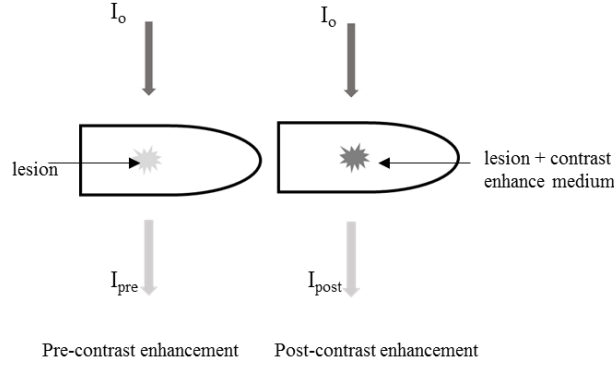


Figure 7.54 Schematic diagram of contrast enhanced imaging.

The dynamics behind the logarithmic subtraction can be understood by modelling the x-ray beam as a monenergetic beam. For simplification, we assume that the detector is ideal, and there is no scatter, giving the intensity before and after the iodine contrast agent as, I_{pre} , and I_{post} respectively by:

$$I_{pre}(x, y) = I_o(x, y)e^{\mu_{bt}} \quad (7.23)$$

And

$$I_{post}(x, y) = I_o(x, y)e^{\mu_{bt}(T-t) - \mu_i t} \quad (7.24)$$

Where $I_o(x, y)$ is the incident x-ray intensity on the detector at position (x, y) , μ_i and μ_{bt} linear attenuation coefficient of iodine and breast tissue respectively, T compression thickness of breast, and t thickness of iodinated lesion. Taking the logarithm of the two equations and subtracting yields the subtracted signal:

$$S_i = \ln I_{post}(x, y) - \ln I_{pre}(x, y) = -(\mu_i - \mu_{bt})t \quad (7.25)$$

The resulting signal, S_i , has a linear relationship with iodine concentration, and lesion thickness. However for a polyenergetic spectrum the relationship is more complicated. The absorbed intensity takes place over a range of energies, and have to be accounted for by

integrating over the entire x-ray spectrum. In order to achieve a linear signal with respect to iodine concentration and thickness of lesion for a polyenergetic x-ray source, a narrow x-ray beam spectrum is required.

7.2.2 Dual Energy Subtraction

Similar to temporal subtraction, a simplified mathematical model of contrast enhanced dual energy subtraction is considered for explanation. Referring to Figure 7.1, only the post-contrast agent administration diagram is considered since two post-contrast images are acquired at a low and a high energy. The respective low and high energy intensity upon transmission through the breast with the iodinated region is given by:

$$I_{LE}(x, y) = I_0^L(x, y)e^{\mu_{bt}^L(T-t) - \mu_i^L t} \quad (7.26)$$

and

$$I_{HE}(x, y) = I_0^H(x, y)e^{\mu_{bt}^H(T-t) - \mu_i^H t} \quad (7.27)$$

Where the superscripts L and H denote the image energy. A weighted subtraction, w_i , is then taken to remove the background breast tissue, resulting in an equation of the form,

$$S_{DE} = \ln(I^H(x, y)) - w_i \ln(I^L(x, y)) = c - t(\mu_i^H - w_i \mu_i^L) \quad (7.28)$$

Where the constant $c = \ln(I_0^H) - w_i \ln(I_0^L)$. High and low energy spectra should be chosen such that $\mu_i^H > \mu_i^L$ and $w_i < 1$. For a polyenergetic source, the relationship with the subtracted signal and iodine is nonlinear since there is overlap of the low and high energy spectra. In addition, the presence of scattered radiation affects the resultant iodinated signal.

7.2.3 Effective Mass Attenuation Coefficient & Effective Absorption Energy Calculations

As seen in equations 7.3 and 7.6, the larger the separation of attenuation coefficients of iodine and breast tissue the larger the signal. Likewise, for dual energy subtraction, the larger the

difference in attenuation coefficients of iodine at low energy and high energy pairs, the larger the signal of the iodinated region. As a result, in choosing energy spectra for temporal or dual energy subtraction, usually *mean energies* of the spectra are used to determine what peak voltage and filter combinations are optimal for increased difference of attenuation coefficients. The *mean energy* is used as it is indicative of the energies at which majority of the x-rays are produced. Although it is worth while using the *mean energies* as an approximation to determining whether the spectra are optimal for iodine contrast enhancement imaging, it does not represent the true effect of the absorption on the spectra since it is modelled as a monoenergetic spectrum. In medical x-ray imaging systems, the photon flux and the absorption is continuous over the range of energies, and not at one discrete value. Therefore, in determining the optimum high energy spectrum for temporal subtraction, and low and high energy spectra pairs for dual energy in the use of iodinated contrast enhanced subtraction, it is worth using the concepts of the *effective absorption coefficient*, and *effective absorption energy*. The *effective absorption coefficient* is described as the weighted mean of the absorption coefficient taking the polyenergetic spectrum into consideration, in essence describing the average absorption due to the range of energies. The *effective absorption energy* is the energy weighted mean energy of attenuation, essentially describing the energy where the majority of photons are attenuated due energy dependency of the linear attenuation. The concept of these two parameters are further discussed in this section.

Derivation

The *fluence rate* for a monoenergetic beam is simply the number of photons per unit area time,

$$\Phi = \frac{N}{A\Delta t}, \quad (7.29)$$

Each photon has energy, $E = h\nu$, since it is monoenergetic, and therefore its total energy is simply EN . Therefore, the energy fluence rate, or intensity of a monoenergetic beam is given by

$$I_0 = E \cdot \phi \quad (7.30)$$

In polyenergetic spectra, each x-ray photon carries its discrete energy, resulting in a line spectrum of the number of photons plotted as a function of energy. The number of photons per unit energy as a function of energy remain constant for a given x-ray source, therefore the x-ray spectrum, $S(E)$, is the line density per unit area time. An integral of the x-ray spectrum yields the fluence rate for a polyenergetic source, given by,

$$\phi = \int_0^\infty S(E) dE \quad (7.31)$$

thus the intensity of the polyenergetic source is given as

$$I_0 = \int_0^\infty E \cdot S(E) dE \quad (7.32)$$

The consequent intensity of a polyenergetic x-ray beam after traversing through an object, with an energy dependent attenuation coefficient, $\mu(E)$, is

$$I(x) = \int_0^\infty E \cdot S_0(E) \cdot e^{-\mu(E)\Delta x} dE \quad (7.33)$$

By recalling the equation for a monoenergetic beam, and substituting equations 7.11 and 7.10 into it, the effective attenuation is given by.

$$e^{-\mu_{eff}\Delta x} = \frac{\int_0^\infty E \cdot S_0(E) \cdot e^{-\mu(E)\Delta x} dE}{\int_0^\infty E \cdot S_0(E) dE} \quad (7.34)$$

For simplification, we take Δx as being infinitesimally small, thus a good approximation of this equation is,

$$(1 - \mu_{eff}\Delta x) = \frac{\int_0^\infty E \cdot S_0(E) \cdot (1 - \mu(E)\Delta x) dE}{\int_0^\infty E \cdot S_0(E) dE} \quad (7.35)$$

Where simple manipulations of the yields

$$\mu_{eff} = \frac{\int ES_0(E)\mu(E) dE}{\int ES_0 dE} \quad (7.36)$$

The equation is synonymous to the weighted mean equation, $\bar{x} = \frac{\sum_{i=1}^n x_i \cdot w_i}{\sum_{i=1}^n w_i}$, where x_i represents some value, and w_i are the weights. On the other hand, the numerator is representative of the mean of the continuous random variable, $\mu(E)$, given the intensity function, $E.S(E)$, is its probability density function, and the denominator normalizes the intensity function so that the mean is calculated.

The terms in the integral of the numerator in equation 7.14 are characteristic of the distribution of photons absorbed as a function of energy. Using the same premise of the weighted mean equation, mean energy of the photon absorption density function, referred to as the effective energy of absorption can be calculated by,

$$E_{eff} = \frac{\int E^2 S_0(E)\mu(E) dE}{\int ES_0\mu(E)dE} \quad (7.37)$$

7.2.4 Simulations for x-ray spectral optimization

X-ray source

The simulated x-ray source spectra were generated using SpekCalc. SpekCalc is software designed to simulate energy spectra emitted from thick-target tungsten anode x-ray tubes used in medical imaging applications^{10–12}. Spectra were obtained for x-rays generated with the parameters listed in Table 1. Mean spectrum energies were calculated, and the bremsstrahlung dose output from the spectra were also recorded from the simulations adjusted to our system's SID. The spectra, mean energies, and bremsstrahlung dose output were used in further analysis and computations in the investigation of spectra for both temporal subtraction and dual energy imaging.

Table 7. 14 Parameters used for spectra simulation

	LE Spectrum	HE Spectrum
Tube Energy	28 – 33 kVp	49 kVp
Filtration		0 – 0.35 mm Cu

Numerical Simulations

A model in MATLAB was generated based on equations 7.14 and 7.15, and was used to predict the effect of spectrum energy and filtration on the attenuation of x-rays in iodine, which is indicative of its resultant signal. The MATLAB model started with the simulated spectra from SpekCalc, $S_0(E)$, and mass attenuation coefficient data for iodine was taken from the table developed by Hubbell *et al*¹³. The simulated Bremsstrahlung output dosage was used to calculate entrance dosage with different peak voltages, and filter thicknesses.

Analysis was done for both temporal subtraction and dual energy contrast enhanced imaging spectra. The model calculated the effective energy, and effective mass attenuation coefficient in terms of the absorbed x-ray energy spectra. For further analysis, graphs of the absorbed dose distribution for iodine were generated.

In temporal subtraction, the desired high energy spectra is one that will maximize the sensitivity of detection for low concentrations of iodine¹⁴. According to Figure 7.2, this would mean that the x-ray spectrum should be shaped such that there are energies above the k-edge of iodine, since there is a sharp increase in the difference of attenuation values between the iodine and breast tissue. In particular, for maximum separation, the challenge is to use an x-ray spectrum where the highest possible portion of x-rays are above the k-edge of iodine¹⁴.

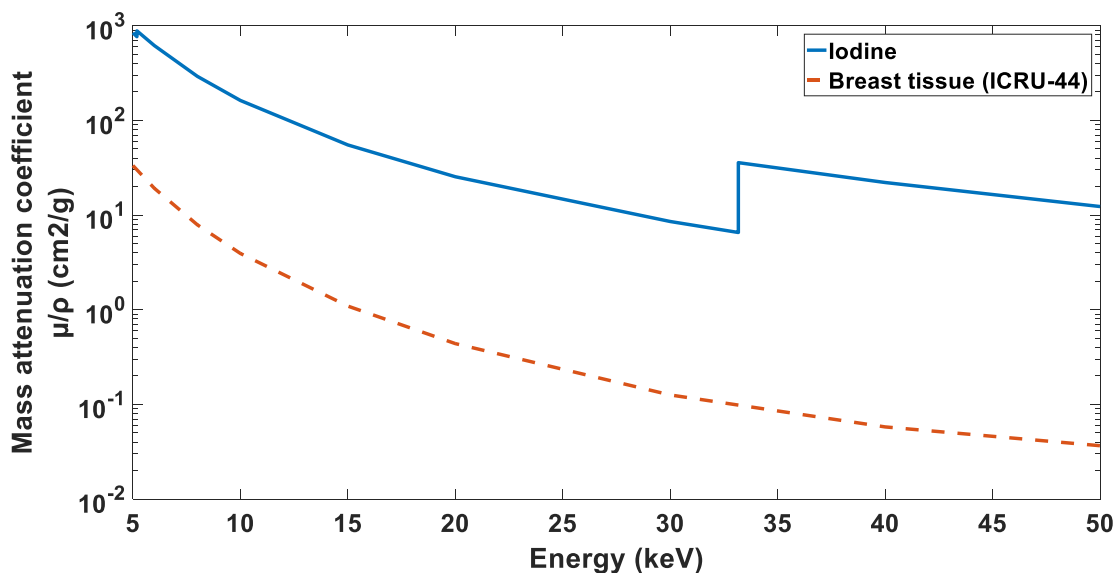


Figure 7.55 Mass attenuation coefficient as a function of photon energy for iodine and breast tissue

Effective absorption energy, and the effective mass attenuation coefficient computations were carried out for iodine and breast tissue using the HE spectra generated from SpekCalc with parameters listed in Table 7.1.

For dual energy spectra analysis, low and high energy spectral pairs listed in Table 7.1 were evaluated to determine the effect on the attenuation values of iodine before and after the k-edge. HE spectra analysis already conducted for TS was used in the analysis combined with the evaluation of the LE spectra listed in Table 1. Graphs of the effective absorption energies against energy and filter thicknesses were generated.

7.2.5 Phantom Experiments

Contrast Agent

The contrast agent used in this study was Omipaque 350 (350 mg/ml I, GE Healthcare Inc., Princeton, NJ). The contrast agent was diluted with water to attain three concentrations of 5

mg/ml, 10 mg/ml, and 15 mg/ml. Area densities of the diluted iodine contrast agent were determined by the product of the density by the depth of the wells in the CE phantom.

Phantom Design

For both temporal subtraction and dual energy contrast enhancement studies, a custom made phantom was created to use in conjunction with a CIRS BR3D (model 020) phantom. The BR3D phantom consist of six individual 1 cm thick semicircular slabs, with a heterogeneous mixture of breast equivalent material simulating approximately 50% adipose and 50% glandular tissue in a swirl pattern. To match the customized phantom attenuating properties as closely as possible to the BR3D phantom, polymethyl methacrylate (PMMA) was chosen as the material for construction as it has similar mass attenuation coefficients of the simulated breast tissue phantom material. The phantom was designed to have the same dimensions as the BR3D phantom, having a radius of 90 mm, and a slice thickness of 1 cm. Four circular wells with covers of depth 2.5 mm, and with individual diameters of 5, 10, 15, and 20 mm were excavated to facilitate the iodinated contrast agent. All wells were on the same plane, with an edge to edge spaced of 12 mm. An image of the customized contrast enhanced phantom together with the CIRS phantom is shown in Figure 7.3.



Figure 7.56 Pictures of the CIRS BR3D phantom together with the custom made phantom used for contrast enhanced imaging experiments.

Temporal subtraction

All temporal subtraction image acquisition sets were done at 49 kVp and a 0.25 mm Cu filter, using 21 projections over a 35° angular span. The detector was operated in 2 x 2 binning mode having a pixels size of 140 μm per pixel. Pre- and post-contrast administration x-ray exposures were equal for all image sets, and set to half the entrance dose for a specified thicknesses' regular screening tomosynthesis as defined by Hologic's recommended dose chart. Considering image registration is very important, the CE phantom was place on top the BR3D phantom for all image acquisitions. All pre-contrast images utilized water as the medium in the wells of the CE phantom. For contrast enhancement administration, the CE phantom was carefully removed without shifting the BR3D plates below, the water replaced with the desired concentration of iodinated contrast agent, and replaced cautiously.

Three phantom thicknesses, 3, 4 and 5cm, were evaluated against three areal concentrations, 1.25, 2.5, and 3.75 mg/cm^2 , of iodine contrast medium. Each pre- and post-contrast image acquisitions were repeated using the PSD placed on the compression paddle. Additional entrance dose using the PSD is <1%, and was considered negligible. Upon image acquisition, images were then gain and offset corrected, prior to logarithmic subtraction as defined in equation 7.3. For the scatter corrected data set, the scatter correction algorithm based on the scatter sampling from the PSD plate were applied to the corrected projection images prior to subtraction. Two sets of reconstructions were conducted; (i) the non-scatter corrected (No SC), and (ii) scatter corrected (SC) reconstructed data

Dual Energy Contrast Enhanced Imaging

For the DE s-DBT experiment, all HE tomosynthesis acquisitions were done at 49 kVp using a 0.25 mm thick Cu filter, and LE acquisitions were acquired at 30 kVp. All 21 sources

were utilized for both energy acquisitions. Regular screening tomosynthesis entrance dose for a specified thickness was used for the LE acquisition, and half of the LE entrance dose was used for the HE acquisitions totaling 1.5 times the dose of a regular screening tomosynthesis. The same phantom thicknesses, and iodine concentrations from the TS experiment were used. For this experiment, the CE phantom was sandwiched between the BR3D plates as pictured in Figure 7.3. Similar to the TS study, each LE and HE image acquisition was repeated with the PSD. HE and LE projection images were offset, gain and scatter corrected before logarithmic subtraction and reconstruction.

Reconstruction

Reconstruction is done using Adaptive Fan Volume Reconstruction (AFVR), an in-house developed tomosynthesis reconstruction software optimized for linear source arrays. The software utilizes adaptive fan volume sampling together with simultaneous algebraic reconstruction technique (SART) for fast iterative reconstruction. The reconstruction slices were computed with a 0.5 mm distance between slices¹⁵.

7.3 Results

7.3.1 Simulations

Mean Energies and Dose Rate Simulations

Initial simulations and calculations involved investigating the HE spectra, mean energies, and dose rate for determining the optimal HE spectrum and filter pair for both TS and DE s-DBT imaging are discussed in this section. Figure 7.4, is a graphical representation of the mean energies calculated from the respective photon fluence spectra, against increasing Cu filter thickness. Based on the mean energies, the 48 kVp spectrum together with 0.1 mm Cu is the first spectrum-filter combination that achieves a mean energy above the k-edge of iodine. At a filter

thickness of 0.15 mm Cu, all spectra (45 – 49 kVp) attain mean energies above the iodine k-edge, which continue to increase with increasing filter thickness. Since the mean energies are representative of equivalent penetration power of a monenergetic beam at the same energy, the graph indicates that a 48 kVp HE spectrum with a 0.1 mm Cu filter would be optimal as it is just above the k-edge of iodine.

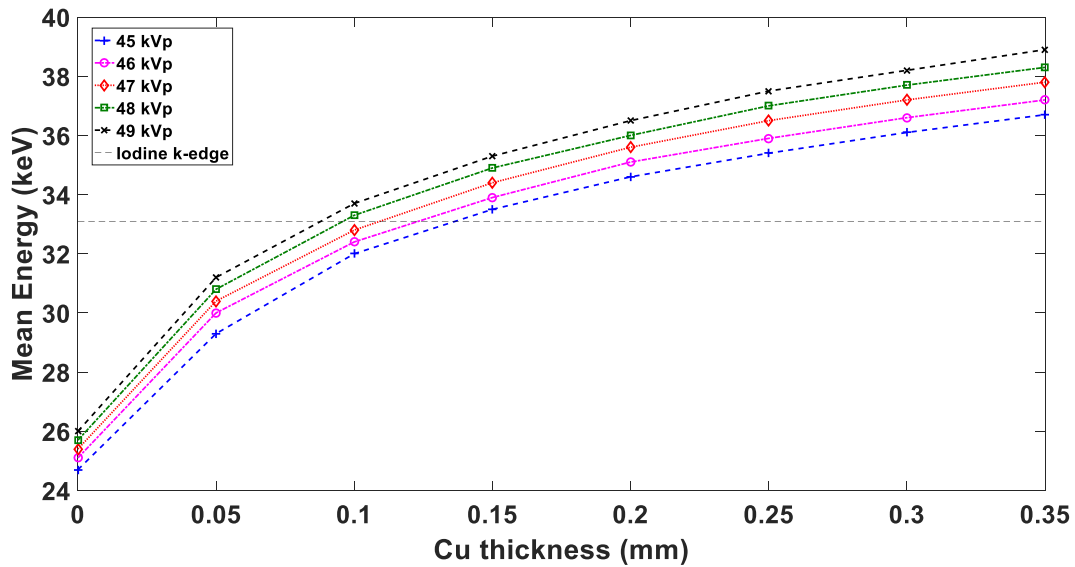


Figure 7.57 Graph of mean energy against increasing Cu filter thickness for simulated x-ray tube spectra with increasing peak voltages ranging from 45 – 49 kVp.

Contrary to increasing mean energy, the entrance dose rate is reduced with increasing filter thickness (Figure 7.5). This is particularly important when choosing a HE spectra and filter combination as sufficient dose needs to be delivered in a timely fashion to prevent further patient motion in both TS and DECE tomosynthesis. Using the optimal spectrum as specified by the mean energy, a calculated entrance dose rate of 3, and 3.16 mR/mAs for the respective peak voltages of 48 kVp, and 49 kVp, with a 0.1 mm Cu combination were obtained. In comparing these reduced dose rates, to the dose rate of the s-DBT tube at a common mammographic peak voltage of 30 kVp (15 mR/mAs), there is an approximate reduction of about 80%. This will

result in a significant increases in imaging time for the pre-and post-contrast administration for TS s-DBT, and long HE acquisition times in DECE s-DBT.

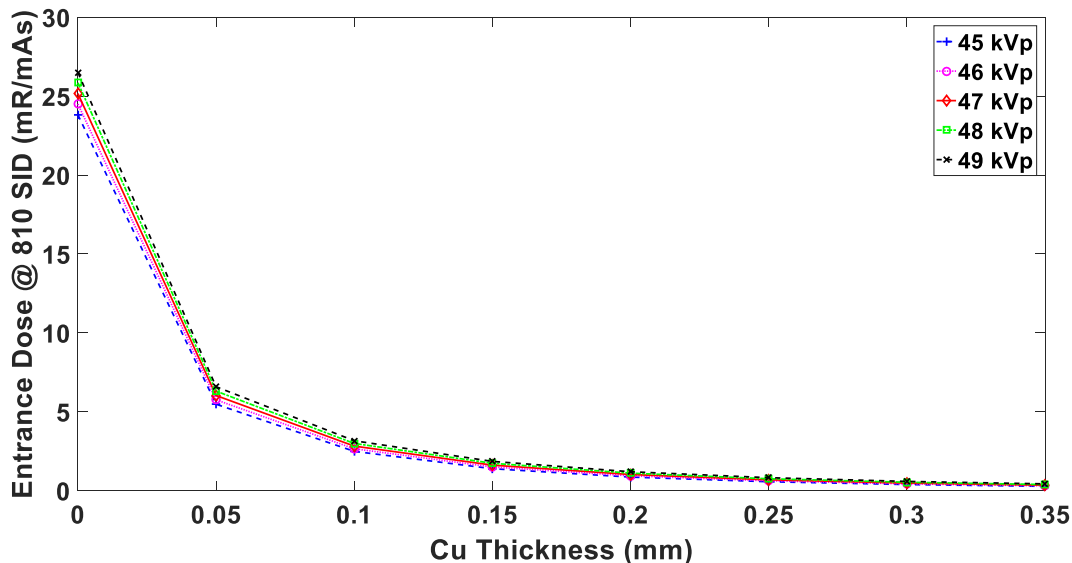


Figure 7.58. Simulated entrance dose rate for the corresponding tube energy spectra as in Figure 7.4. System geometry use to simulate dose rate were synonymous to the Gen 2 s-DBT system.

Effective Mass Attenuation Coefficient & Effective Absorption Energy Calculations

Though mean energies give a good indication on the combination of low and high energy spectra pairs to be used for optimal iodine images, it is based on the assumption of monoenergetic x-rays. In this section, the effective mass attenuation coefficient and absorption energies are investigated, accounting for the polyenergetic character of the spectra from the imaging system.

For both imaging modalities, a desirable HE spectra is one with the majority of photons are at an energy just above the iodine k-edge, while maintaining sufficient photon flux. In the case of TS, increasing the number of photons just above the iodine k-edge increases the sensitivity of iodine signals by increasing the difference in the mass attenuation coefficients of

breast tissue and iodine. For DECE, increasing the number of photons above the iodine k-edge further separates the HE and LE spectra pairs, reducing overlap and also increasing sensitivity.

Figure 7.6 illustrates the effect of increasing Cu thickness on the 49 kVp energy spectrum. Increasing Cu thickness increases the mean energy of the spectrum by absorbing lower energy photons. As a result, photon flux is reduced, and the shape of the spectra narrows to the right with an increasing mean energy as higher energy photons are transmitted through the filter. As the mean energy increases, the ratio of photons with energies above the iodine k-edge in the spectrum increases.

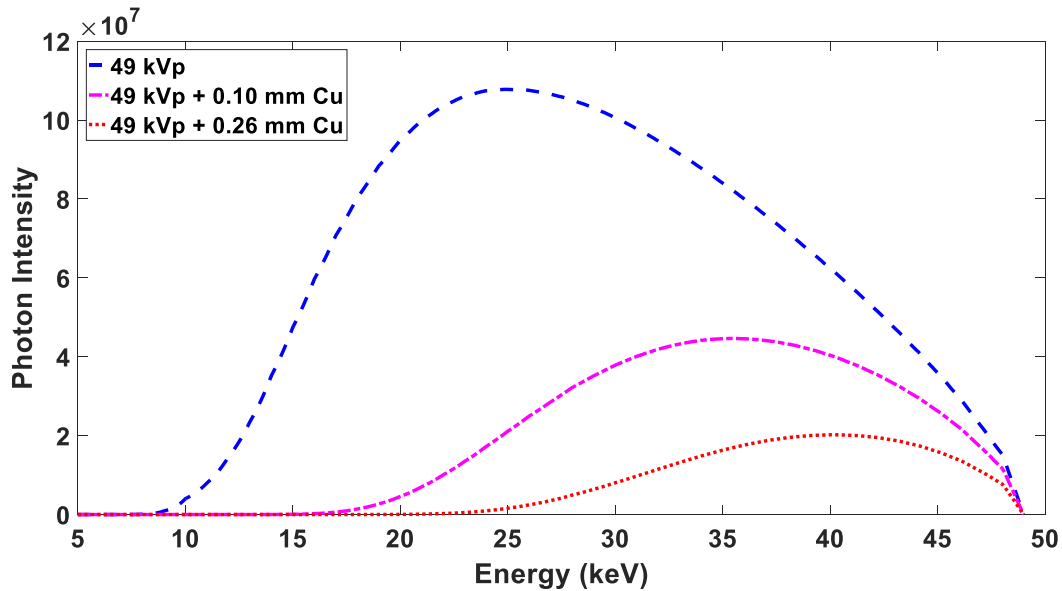


Figure 7.59. The simulated effect of increasing Cu filter thickness on a 49 kVp tube spectrum. As Cu filter thickness increases, the photon flux is reduced and the modal energy shifts to the right.

Figure 7.7 shows the normalized photon spectra after filtration to show the energy dependence distribution as it shows a clearer depiction on the ratio of photons with energies above the iodine k-edge.

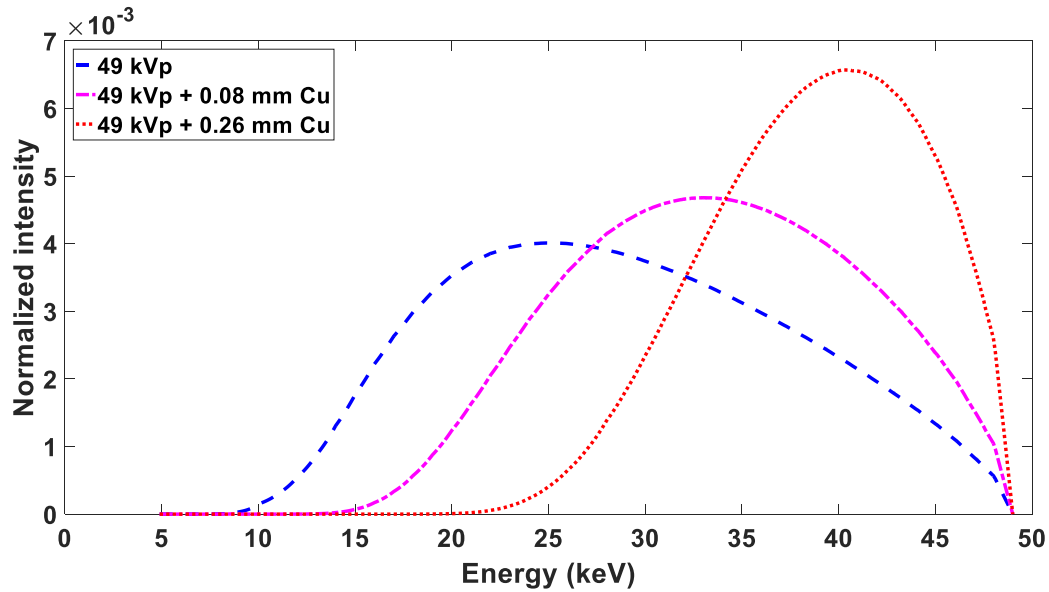


Figure 7.60 Simulated effect of increasing Cu thickness on a normalized 49 kVp spectrum. The normalized spectrum shows the reduction in the amount of lower energy photons, resulting in an increase of photons at higher energies, increasing the mean energy value.

The effect of the continuous energy dependent mass attenuation coefficient on the polyenergetic spectra was then studied. Figure 7.8 show the corresponding normalized photon absorption distribution (dose) in iodine for the spectra show in Figure 7.7. At 49 kVp without additional filtration, a sharp increase of the photon absorption occurs at the iodine k-edge, however the majority of photon absorption occurs before, with a local maxima occurring around 17 keV. This suggest that significant absorption will occur at energies below the iodine k-edge, limiting sensitivity in TS, and causing significant overlap in the HE and LE attenuation values for DE CE. As Cu thickness increases, and the distribution of photon transmitted from the source becomes negatively skewed, an increase in the ratio of absorption above the k-edge occurs while there is a simultaneous decrease in the range of energies, and amount of photons absorbed below the k-edge.

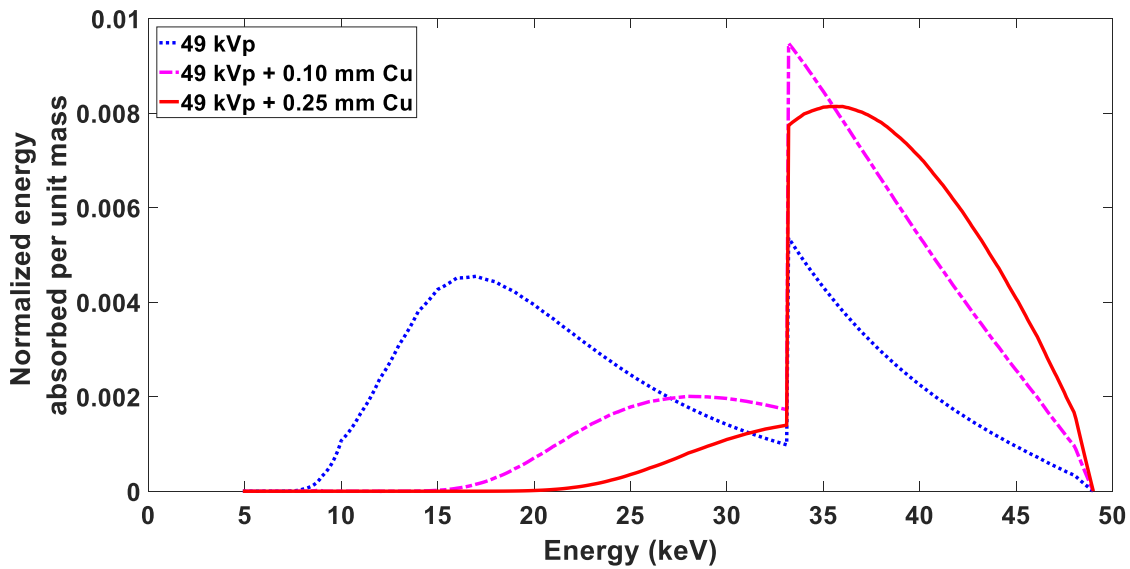


Figure 7.61 Simulated calculations of the normalized absorbed dose spectra in iodine for a 49 kVp tube voltage with increasing Cu filter thickness.

The effective mass attenuation coefficient, and energy absorption calculations for the 49 kVp spectrum with increasing Cu thickness were calculated using equation 7.14 and 7.15, and plotted in Figure 7.9. The highest effective mass attenuation coefficient calculated for the range of Cu thicknesses was at 49 kVp without additional filtration, having a value of $22.74 \text{ cm}^2/\text{g}$. This is expected as the mode and mean of the photon absorption distribution before the iodine k-edge are at energies where the mass attenuation coefficients are higher than the values above the k-edge. This is further validated by considering the effective absorption energy values. At 49 kVp without additional filtration, the effective absorption energy is 26.19 keV. This is indicative of the majority of absorption occurring before the k-edge, as this value is close to the mean value of the photon absorption distribution before the k-edge. At these low energies, high contrast between breast tissues also exist, limiting the difference in attenuation between the iodine and breast tissue. As Cu filtration is added, there is a sharp decrease in the effective mass attenuation coefficient until a minimum of $18.63 \text{ cm}^2/\text{g}$ is reached and values begin to increase. The sharp

decrease can be explained by the decrease in the amount of photons being absorbed at lower energies, as they are removed via filtration. This increases the effective absorption energy, lowering the effective attenuation coefficient to a minimum around the iodine k-edge at 0.06 mm Cu thickness. At Cu thicknesses beyond 0.06 mm, the effective attenuation coefficient gradually increases and then begins to plateau. The absorption energies above the iodine k-edge indicate that most photons are being absorbed above the k-edge explaining the increase in the effective attenuation coefficient. Though most photon absorption occurs at energies above the k-edge, absorption at energies lower than the k-edge still influence the overall attenuation, as lower energy photons are not completely removed. This results in the decreasing rate of increase of the effective attenuation seen in the Figure 7.9 for the range of Cu thickness evaluated.

The HE polyenergetic spectra calculations suggest that choosing an energy spectrum with a mean energy just above the iodine k-edge is not sufficient as significant absorption still occurs at lower energies. Consequently, using higher energies, with filter combinations that allow for optimal negative skewing of the photon distribution while maintain sufficient photon flux is preferred.

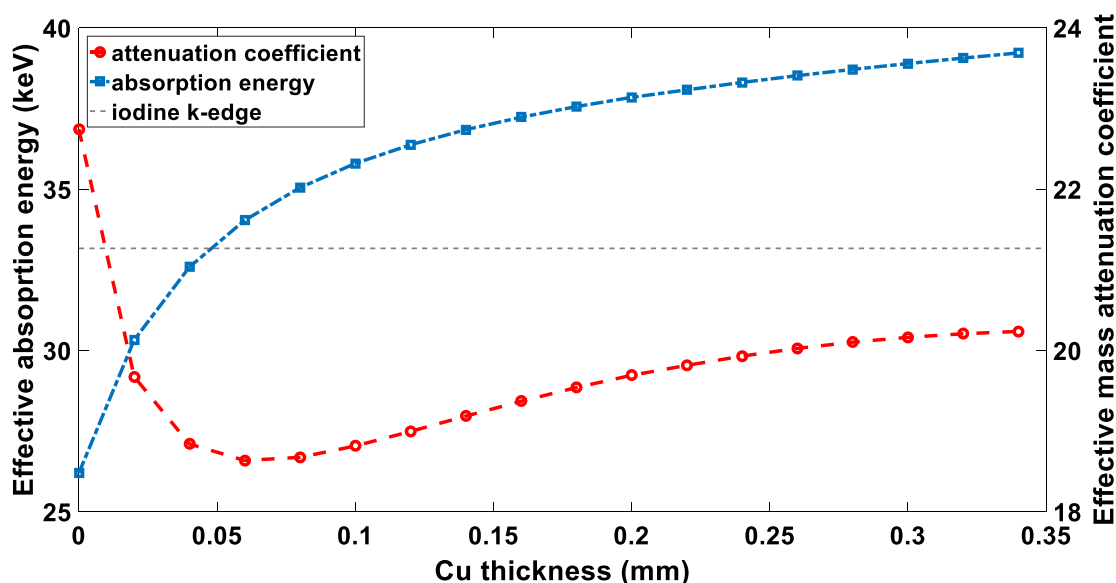


Figure 7.62. This graph displays the simulated calculations of the effective absorption energy of iodine, and the effective mass attenuation coefficient of iodine with increasing Cu filter thickness.

In DE imaging, since optimizing image quality at the lowest possible radiation dose is of primary importance, the LE spectrum choice is usual in the regular mammographic energy ranges, as it can serve as a regular screening image⁴. Figure 7.10 shows the normalized photon fluence of LE spectra for 28, 30, and 33 kVp. As the energy is increased, the shift of the spectra maxima is apparent, and the mean energies of the spectra increase. Similarly, there is an increase in the effective absorption energy, as more photons at increasing energies are absorbed. A simulated result of the LE effective attenuation coefficient and absorption energy is shown in Figure 7.11. The values of the effective attenuation are higher than those above the iodine k-edge, due to the significantly higher mass attenuation coefficient of iodine at low energies (10 – 15 keV). As the LE spectrum peak energy increases toward the iodine k-edge, the effective attenuation coefficient decreases gradually because absorption of lower energy photons continue to occur. This low energy absorption will continue to affect the overall attenuation, preventing effective attenuation values from approaching the value preceding the iodine k-edge.

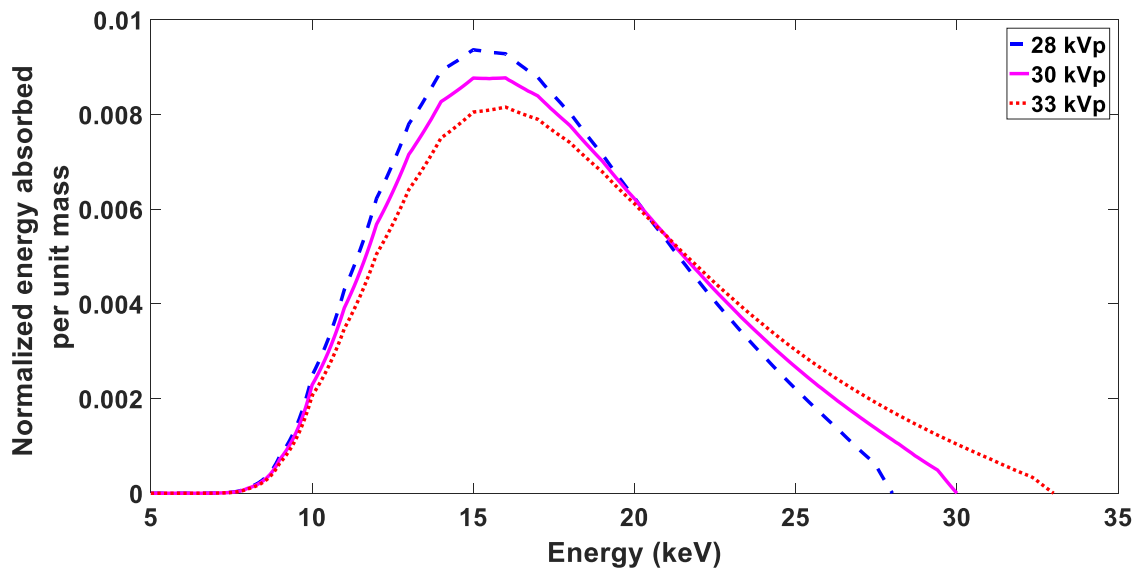


Figure 7.63. Normalized photon fluence for low energy spectra in DE imaging simulations the simulated calculations of the effective absorption energy of iodine, and the effective mass attenuation coefficient of iodine with increasing Cu filter thickness.

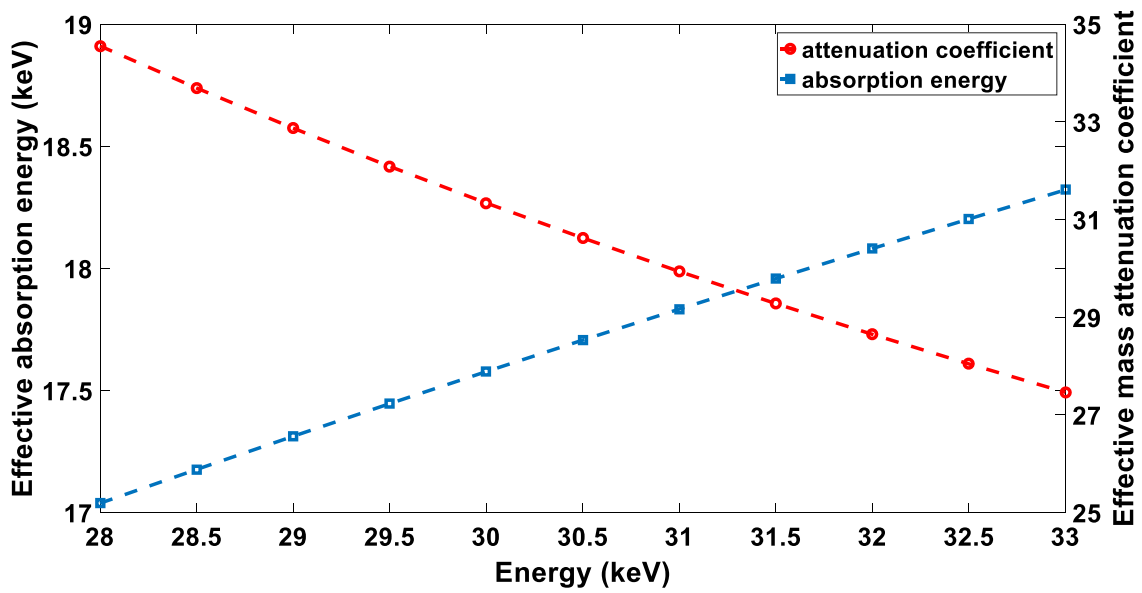


Figure 7.64. Simulated calculations of the effective absorption energy of iodine, and the effective mass attenuation coefficient of iodine for the low energy, dual energy spectrum range.

Figure 7.12 illustrates the normalized dose profile of iodine for a 30 kVp LE, and 49 kVp + 0.25 mm Cu spectra pair. As seen, there is insignificant overlap of absorption of photons for the energy pair. However, for the LE spectrum, a significant amount of absorption occurs at low energies, where the attenuation coefficients are similar to those above the k-edge or greater.

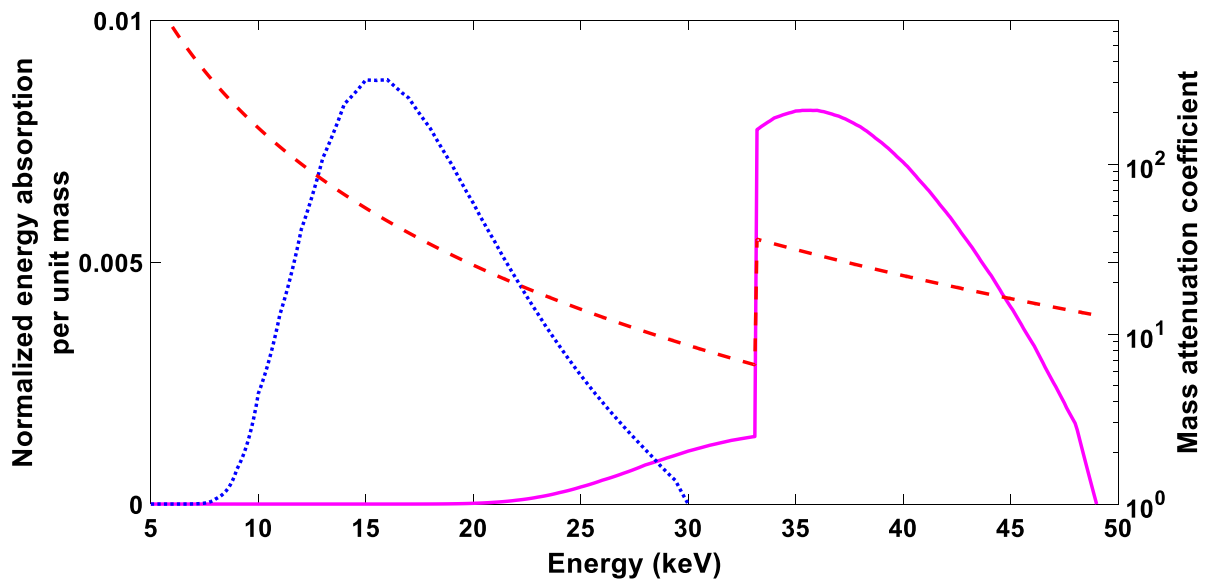


Figure 7.65. Simulated calculations of the normalized absorbed dose spectra in iodine for LE, 30 kVp, and HE 49 kVp with 0.25 mm Cu filter. This dual energy spectra pair was used in the phantom experiments.

These results demonstrate the dilemma with optimizing energy spectra pairs for DECE imaging. The distribution of photons in the polyenergetic spectra reduce iodine sensitivity as similar absorption coefficients are present in both energy spectra. To achieve optimum sensitivity, low energy photons in the LE spectrum should be filtered to increase the ratio of photons with energies near the iodine k-edge.

7.3.2 Phantom Experiments

Temporal Subtraction

The effect of areal iodine concentration and phantom thicknesses were investigated by measuring the iodine signal in the form of the reconstructed pixel value (PV) of the iodinated regions of interest for the in-focus slice. The results for the three varying thicknesses investigated are shown in Figure 7.13. The iodine signal was found to increase linearly with increasing areal concentration, regardless of phantom thickness. However, as seen in the figure, the iodine signal shows dependence on phantom thickness, as the slope of the linear relationship between iodine signal and areal concentration decreases with increasing phantom thickness.

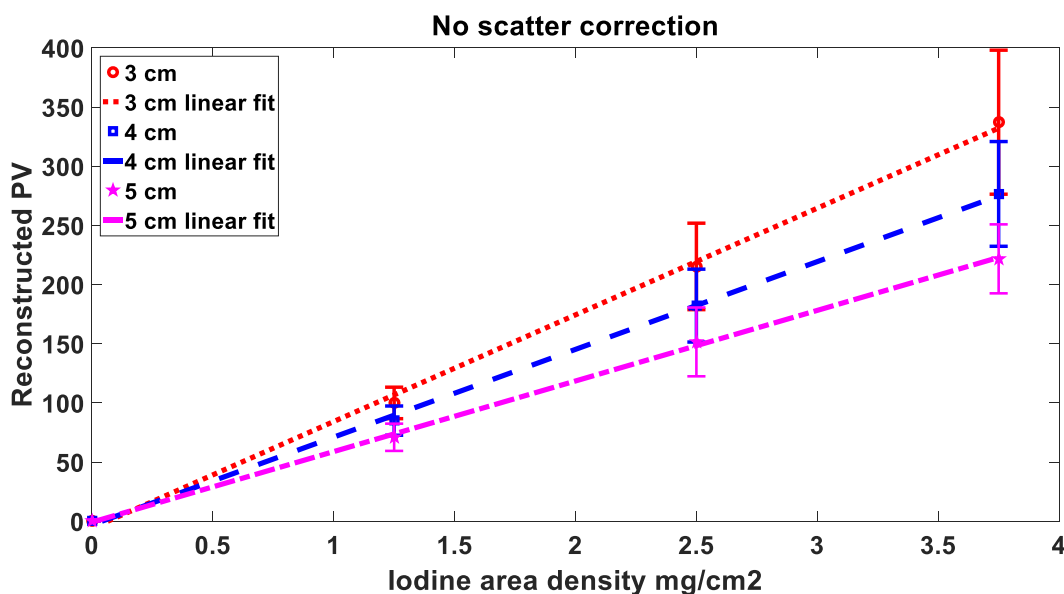


Figure 7.66 Reconstructed iodine signal values against iodine areal density without scatter correction. A linear relationship is observed for all phantom thickness in the plot. The sensitivity of iodine quantification reduces with increasing phantom thickness.

The effect of scatter on the quantification of iodine was investigated by measuring the iodinated ROI signal subsequent to scatter correction. Figure 7.14 shows the central projection images of the phantom pre- and post-iodine contrast agent administration, and the resulting

subtracted image prior to reconstruction. The severe cupping artifact observed for both of these HE pre- and post-iodine acquisitions is not evident in the subtracted image, indicative that the scatter profiles are similar for both acquisitions. The resulting subtracted image shows the enhanced iodinated regions, as the background simulated tissue is suppressed by its logarithmic subtraction.

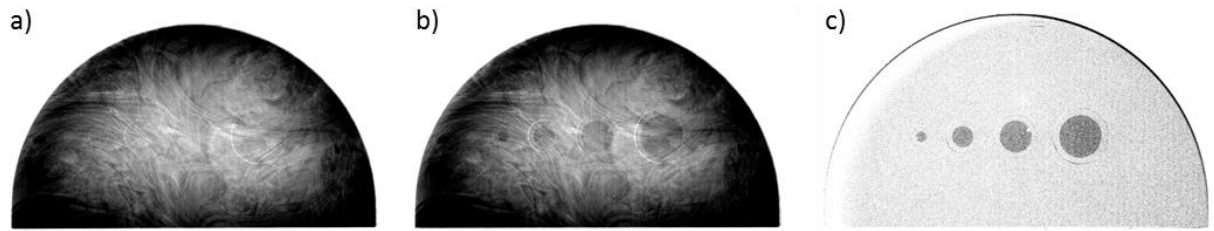


Figure 7.67 (a-c) Non-scatter corrected pre-contrast, post-contrast, and the logarithmic subtraction for the 5 cm CE phantom with areal concentration 2.5 mg/cm^2 .

The respective scatter corrected projection images are displayed in Figure 7.15. A drastic reduction in the cupping artifact for both the pre- and post-contrast projection images is observed, resulting in an increase in the iodine signal for the post-contrast administration projection image. This results in a subtracted image with an increased iodinated signal compared to projection images processed without scatter correction.

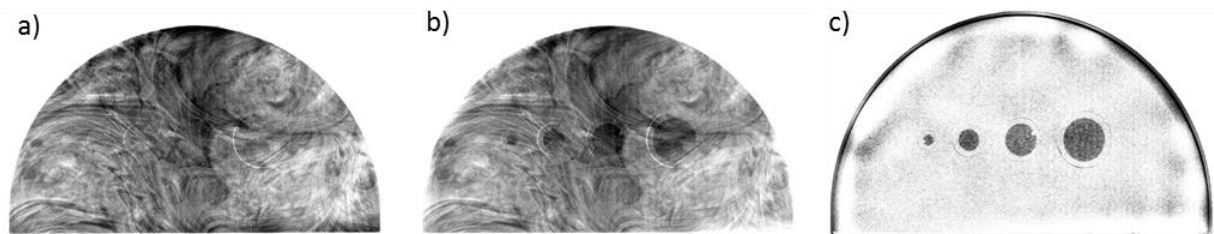


Figure 7.68 (a-c) PSD corrected pre-contrast, post-contrast, and the logarithmic subtraction for the 5 cm CE phantom with areal concentration 2.5 mg/cm^2 .

A plot comparing the line profile across the iodinated regions for the subtracted projections images for both the scatter corrected and non-scatter corrected is shown in Figure 7.16. The increased iodine signal is attributed to the reduction in scatter.

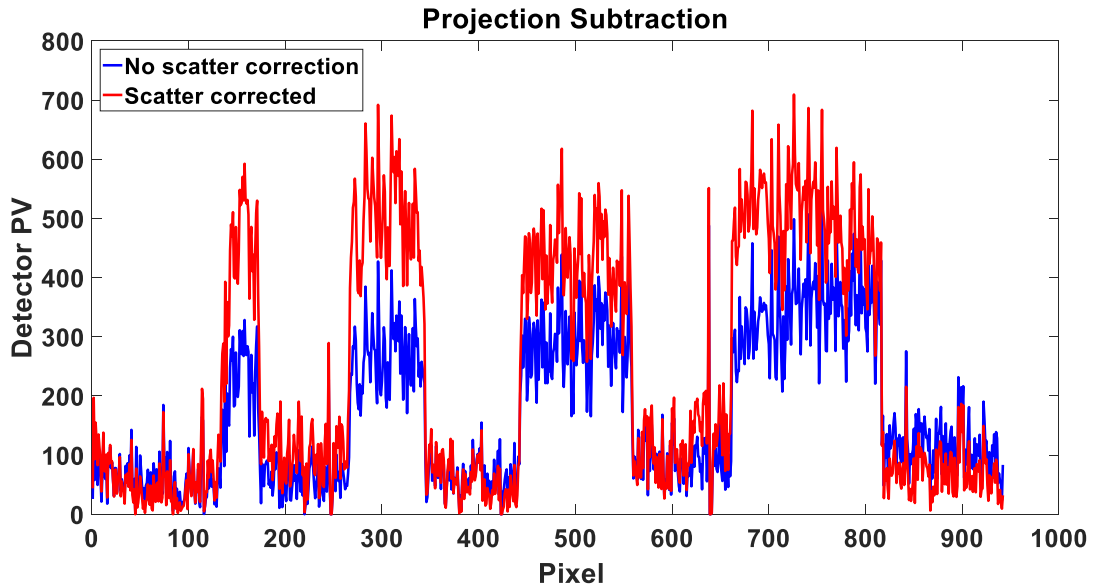


Figure 7.69 Line profiles across the iodinated regions for the non-scattered corrected and PSD scatter corrected subtracted projection image for the central source.

The same trend is observed in the reconstructed subtracted images, with the scatter corrected in-focus slice having higher signal values. Reconstructed in-focus slices are displayed in Figure 7.17, and accompanying line profiles in Figure 7.18.

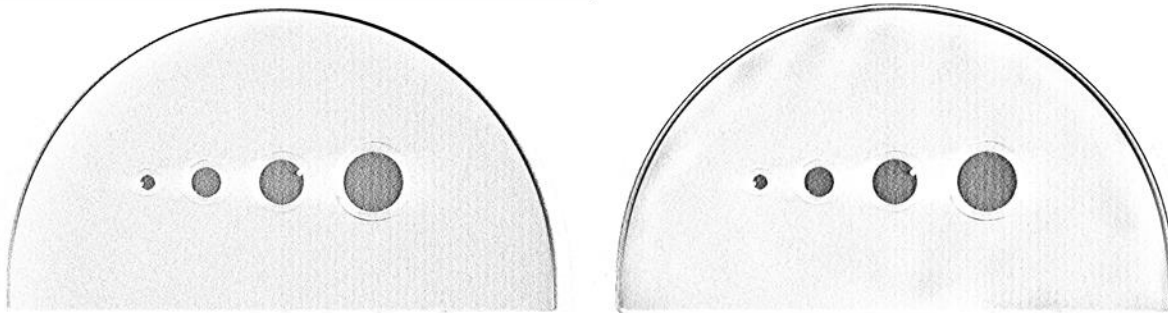


Figure 7.70 (a) In-focus reconstructed slice for the (a) non-scatter corrected subtracted image acquisition set, and (b) PSD scatter corrected subtracted image acquisition set. The scatter corrected reconstructed image shows increased contrast compared to the non-scatter corrected.

Comparing the plots of the line profiles of the projection images and reconstructed in-focus slices, less background and signal noise is observed in the reconstructed in-focus slice plot for both scatter and non-scatter corrected images. The edges of the profiles for each iodinated ROI is more sharply delineated in the plots for the reconstructed in-focus slice indicative of increased conspicuity moving from subtracted projection images, to the subtracted reconstructed images. In the reconstructed in-focus slices, the signals on the edge of the ROI are higher than those measured in the center, and can be attributed to the edge effect in tomosynthesis reconstructions. Resultantly, PVs were measured using 70% of the inner area of the iodinated region. .

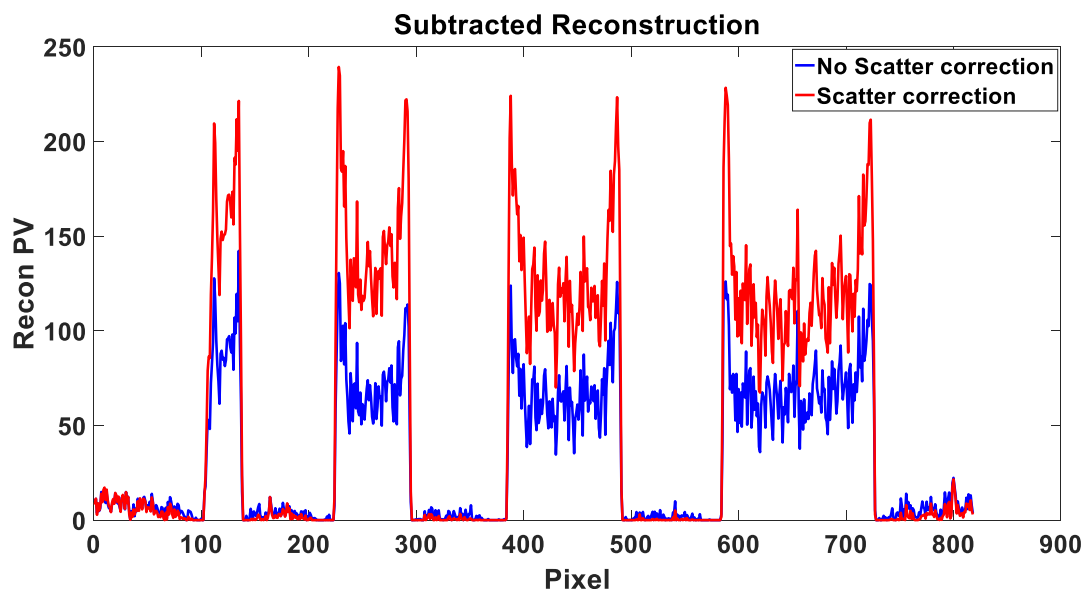


Figure 7.71 Line profiles across the iodinated regions for the reconstructed in-focus slices of the non-scatter corrected and scatter corrected tomosynthesis acquisitions. Edge effects due to tomosynthesis reconstruction are apparent in the line profiles.

In comparing the scatter corrected iodine signals with increasing areal iodine concentration for different compression thicknesses, a smaller reduction in the slopes of the linear relationships between signal and areal concentration is observed as seen in Figure 7.19. The reduction in the difference in the slopes indicate that the scatter correction increases the sensitivity in the quantification of iodinated regions.

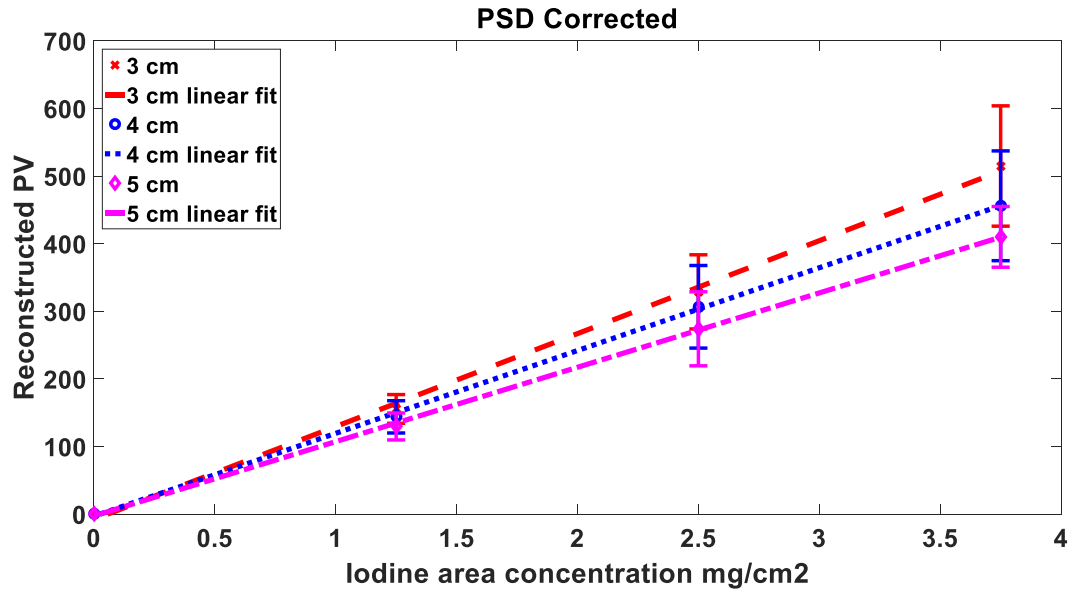


Figure 7.72 Reconstructed iodine signal values against iodine areal density with PSD scatter correction. A linear relationship is observed for all phantom thickness in the plot. Though sensitivity is reduced with increasing phantom thickness, there is increased sensitivity compared to the non-scatter corrected reconstructions

Dual Energy

In the DE experiments, the HE image pairs for the DE acquisition exhibited the cupping effect as expected. The effect of scatter reduces the visibility of the iodine signal in the weighted subtraction, which is propagated to the reconstruction. Figure 7.20 (a-c) illustrates the effect of the cupping effect on the HE projection image, and resultant weighted logarithmic subtraction for the CE phantom. Though the iodinated discs are of the same areal concentration, they are viewed with different intensities, which results in inaccurate reconstruction values of the iodinated regions. Figure 7.20 (c-e), illustrates the scatter corrected projection images for the CE phantom, and the subsequent weighted subtracted projections. The HE scatter corrected projection image clearly shows a reduction in the cupping artifact. The LE projection image shows increased contrast. The resultant logarithmic subtracted image shows iodinated signals of the same intensity for each disk, with the suppression of the simulated anatomical background. Figure 7.21 compares line profiles through the iodinated regions for both non-scatter and scatter

corrected subtractions. Similar PVs are observed for each iodine ROI for the scatter corrected weighted subtractions compared to the varying intensities observed in the non-scatter corrected subtraction. These results show that using the PSD, significant reduction in the cupping artifact is observed, leading to more accurate quantification of iodine in the subtracted projection images.

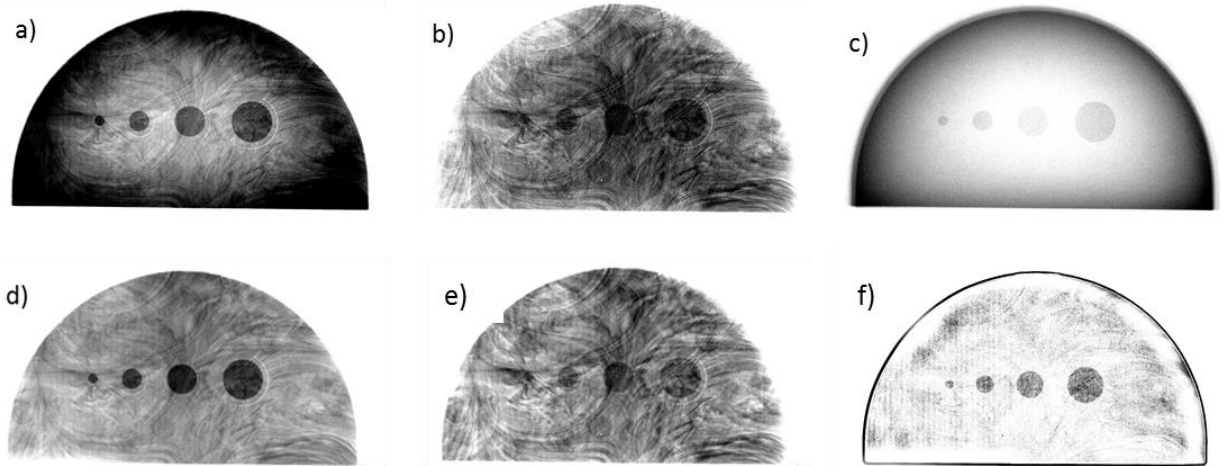


Figure 7.73 (a-c) Non-scatter corrected HE, LE, and the weighted logarithmic subtraction for the 5 cm CE phantom with areal concentration 3.75 mg/cm^2 . (d-f) Corresponding PSD scatter corrected images in the same order

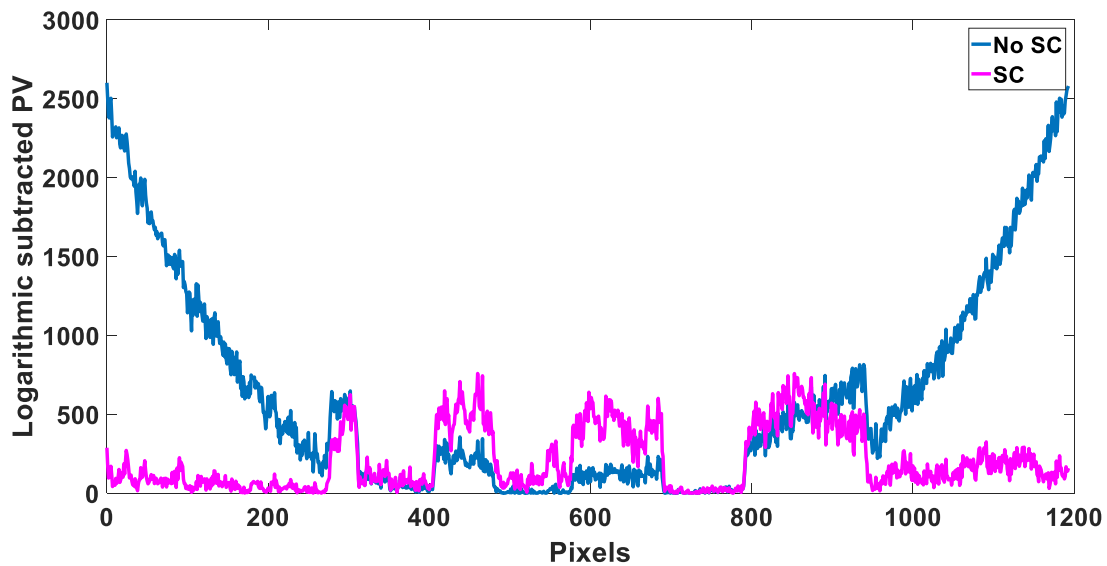


Figure 7.74 Line profile across iodine regions for DE weighted subtracted projection images shown in Figures 7.22(c) and 7.22(f).

With the improved visibility of the iodine signal in the weighted subtraction reconstruction due to scatter correction, the quantification of iodine in the reconstructed image was investigated. Figure 7.22 shows the in-focus reconstructed slice of the weighted subtractions of the CE phantom at 3, 4, and 5 cm thickness, with an areal iodine concentration of 3.75 mg/cm^2 . Though the weighed subtraction is applied, each slice shows the remanence of the swirl pattern in the phantom as complete suppression is unattainable with polychromatic spectra. Artifacts on the periphery of the phantom observed in the reconstruction are as a result of incomplete removal of the cupping artifact in the projection images. Though indiscernible in the figure, the iodine signal values experience a marginal decrease with an increase in phantom thickness. The decrease in the signal with increasing phantom thickness is made more obvious when comparing the line profile across the iodinated regions as displayed in Figure 7.23.

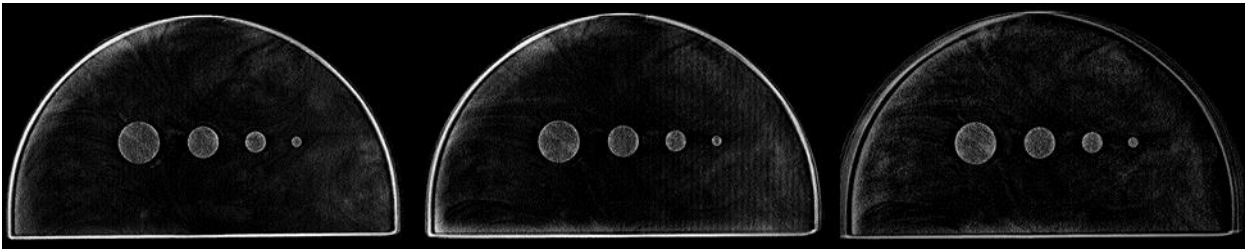


Figure 7.75 (a-c) Scatter corrected reconstructed slices containing iodine regions of 3.75 mg/cm^2 areal concentration for the 3, 4 and 5cm thick CE phantom

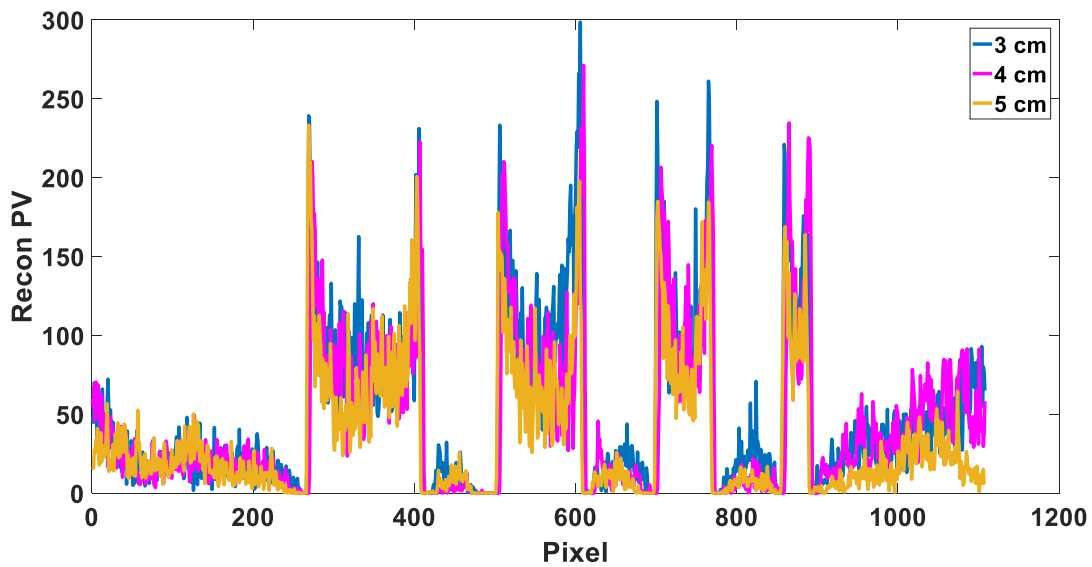


Figure 7.76 Line profiles across the iodine regions for the DE subtracted reconstructions for phantom thicknesses of 3, 4 and 5 cm. The line profile shows the slight decrease in signal with increasing phantom thickness.

The decreasing iodine signal with increasing phantom thickness is suggestive of the increasing amounts of scatter produced with increasing phantom thickness. The line profiles also show the rise in intensity values near the edge of the phantom, as traces of the cupping artifact are proliferated through to the reconstruction.

Further analysis of the iodine signal intensities for the reconstructed slices containing the iodine against areal concentration for phantom thicknesses of 3, 4 and 5 cm are illustrated in Figure 7.24. Synonymous to measurements made for signal intensities in TS, the average pixel value was measured using 70% of the inner area of the iodinated region as the figure of merit to avoid the edge effects.

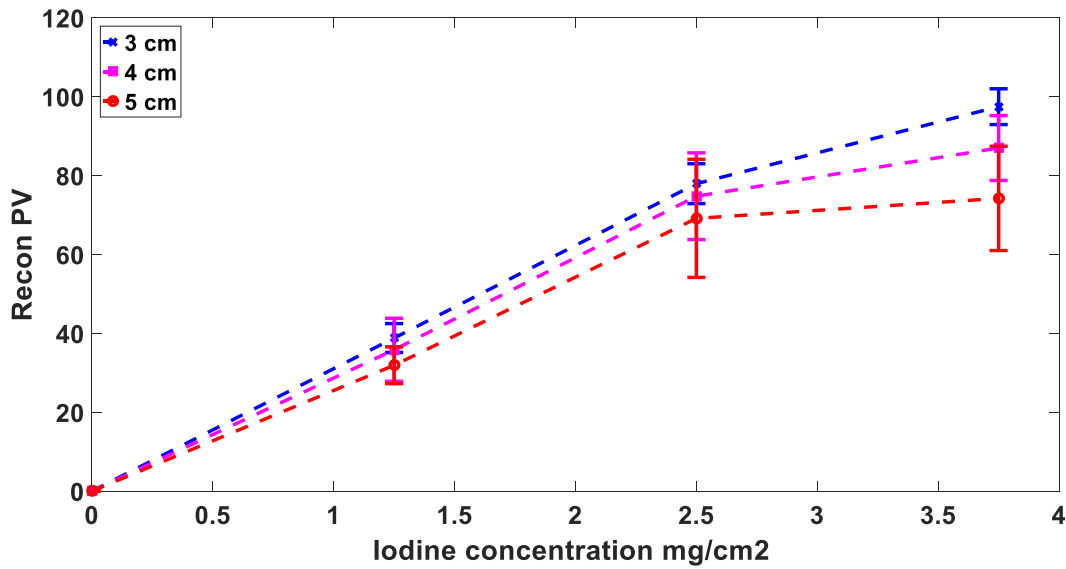


Figure 7.77 Reconstructed iodine signals for the scatter corrected DE subtractions against iodine concentration.

The same trend is observed for the other concentrations of iodine and phantom thicknesses. With increasing phantom thickness, the iodine signal is slightly reduced. Also, the iodine signals deviates from its expected linear relationship with increasing concentration, and becomes more pronounced with increasing phantom thickness. The deviation from linearity is a result of poor separation in mass attenuation values of iodine between the HE and LE spectra. The increase in this deviation with increasing phantom thickness is attributed to the increased scatter with increasing thickness.

Figure 7.25 shows a comparison of the iodine signals detected for both TS and DE s-DBT. As anticipated, TS is more sensitive than DE s-DBT, also showing evidence of iodine quantification.

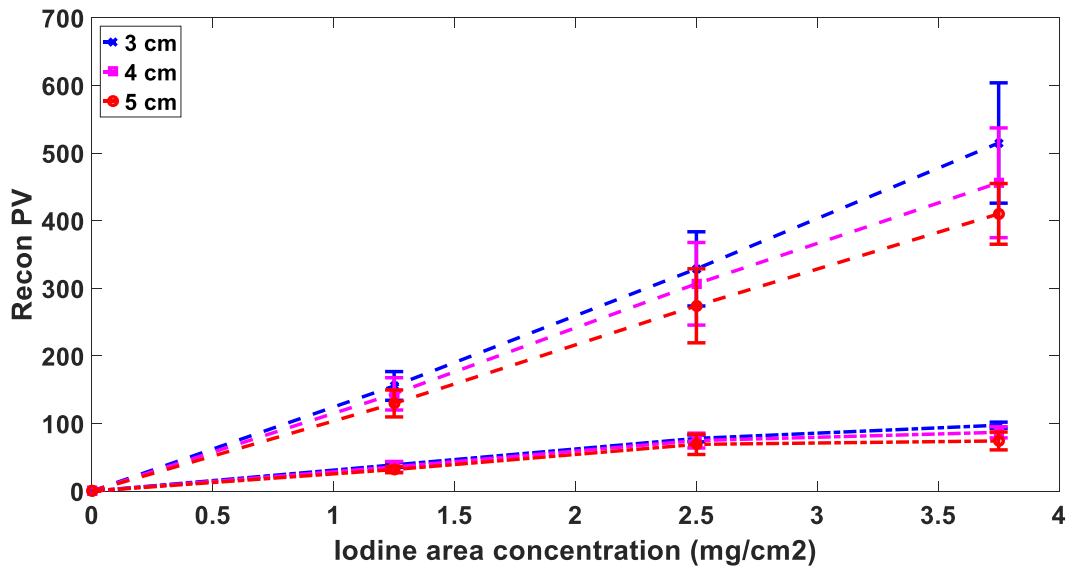


Figure 7.78. Comparison of the reconstructed iodine signals for both TS and DE imaging for different phantom thicknesses against increasing areal concentration. The TS subtraction is significantly more sensitive than DE imaging.

7.3.3 Discussion and Conclusion

Goals of this study included (i) determining the feasibility of contrast enhanced imaging with the 2G s-DBT system, and (ii) determining its sensitivity in the quantification of iodine in CE breast phantoms. Numerical simulation studies of tube energy spectra, followed by phantom evaluations were conducted to determine whether the system parameters were capable of producing CE iodinated ROIs, with sufficient anatomical suppression, and offering an accurate localization of iodine ROI. Both methods, TS and DE, contrast enhancement modalities were investigated.

Results of the HE spectra simulation studies showed that peak tube voltages with Cu filter combinations that have mean energies just above the iodine k-edge are not optimal for polyenergetic spectra. Therefore, the maximum limit of the s-DBT x-ray tube (49 kVp) with a maximum Cu thickness allowing for sufficient photon flux is desirable. Results indicate that the

rate at which the dose rate decreases is larger than the rate at which the effective mass attenuation coefficient increases. Therefore in choosing a Cu filter thickness for the 2G s-DBT system, a compromise on the maximum achievable effective mass attenuation coefficient for entrance dose was made. Simulation results were used to help choose a 0.25 mm Cu filter for phantom experiments. Though this study did not investigate the effect of dose on image quality, previous studies have had similar results recommending utilizing higher beam energies, and have had acceptable results with Cu filters greater than 0.2 mm in thicknesses^{4,16,17}. For the LE spectrum in DECE s-DBT, simulation results suggest employing typical mammographic tube energies (28 – 33 kVp) would result in poor sensitivity, and low iodine signals. Increasing absorption of photons closer to the iodine k-edge while simultaneously reducing the amount of photons available for absorption at low energies by filtration would improve sensitivity and detection of iodine in DE imaging. However, this would impact imaging times, or require higher powered x-ray tubes.

The phantom experiments suggest that the 2G s-DBT system is capable of both TS and DE imaging. The TS method showed a linear relationship with the reconstructed signal and iodine concentration, with further improvement in iodine signal with scatter correction. Though with our scatter correction absolute iodine quantification is not achieved, this shows evidence that with further technique optimization, accurate quantification of iodine may be possible. In the DE experiments, significantly less sensitivity, and relatively low iodine signals compared to those acquired from TS were measured. Though scatter correction improved the signal of iodine by reducing signal dependence on phantom thickness, this technique does not show any evidence of absolute iodine quantification. Further improvement of this technique is inherently difficult with limitation imposed by the polyenergetic spectra, tube power, and filters.

Both techniques offer advantages, which may be exploited by s-DBT. Fast image acquisition times, and the capability of alternating source sequences for TS may allow for rapid dynamic contrast imaging. In DE s-DBT, though iodine quantification is not optimal, the rapid image acquisition times coupled with fast interleaved acquisition options make it a promising method of detecting inconspicuous lesions within a 3D framework.

The PSD shows effectiveness by improved TS results, and acceptable DE results. It stresses the importance of angular and object specific scatter correction in tomosynthesis. However, the PSD method for our s-DBT system requires an additional set of tomosynthesis images with the PSD plate in place, significantly increasing imaging time. This is counterproductive to patient imaging as long imaging times lead to registration artifacts. In summary, investigation of CE imaging with the 2G s-DBT system shows potential. However, for implementation into a clinical setting, a tube capable of achieving higher power can make DECE s-DBT a viable modality for breast cancer imaging.

7.4 REFERENCES

- ¹ M.L. Nock, M.P. Kempston, J.G. Mainprize, and M.J. Yaffe, Proc. SPIE **6510**, 65102W (2007).
- ² J.T. Bushberg, J.A. Seibert, E.M. Leidholdt, J.M. Boone, and M. Mahesh, Med. Phys. **40**, 077301 (2013).
- ³ S.C. Chen, A.-K. Carton, M. Albert, E.F. Conant, M.D. Schnall, and A.D. Maidment, Acad. Radiol. **14**, 229 (2007).
- ⁴ E. Samei and R.S. Saunders, Phys. Med. Biol. **56**, 6359 (2011).
- ⁵ V. Froeling, F. Diekmann, D.M. Renz, E.M. Fallenberg, I.G. Steffen, S. Diekmann, R. Lawaczek, and F.F. Schmitzberger, Eur. Radiol. **23**, 1528 (2013).
- ⁶ Y. Lu, B. Peng, B.A. Lau, Y.-H. Hu, D.A. Scaduto, W. Zhao, and G. Gindi, Phys. Med. Biol. **60**, 6323 (2015).
- ⁷ A.K. Carton, J.A. Currivan, E. Conant, and A. Maidment, Lect. Notes Comput. Sci. (Including Subser. Lect. Notes Artif. Intell. Lect. Notes Bioinformatics) **5116 LNCS**, 166 (2008).
- ⁸ L. Chen, Y. Lu, Y.-H. Hu, W. Zhao, and G. Gindi, SPIE Med. Imaging **8668**, 86685O (2013).
- ⁹ C.R. Inscoe, A.W. Tucker, O.Z. Zhou, and J. Lu, in edited by R.M. Nishikawa and B.R. Whiting (International Society for Optics and Photonics, 2013), p. 86680H.
- ¹⁰ G. Poludniowski, G. Landry, F. DeBlois, P.M. Evans, and F. Verhaegen, Phys. Med. Biol. **54**, N433 (2009).
- ¹¹ G.G. Poludniowski, Med. Phys. **34**, 2175 (2007).

- ¹² G.G. Poludniowski and P.M. Evans, Med. Phys. **34**, 2164 (2007).
- ¹³ J.H. Hubbell and S.M. Seltzer, (1995).
- ¹⁴ M. Skarpathiotakis, M.J. Yaffe, A.K. Bloomquist, D. Rico, S. Muller, A. Rick, and F. Jeunehomme, Med. Phys. **29**, 2419 (2002).
- ¹⁵ G. Wu, C. Inscoe, J. Calliste, Y.Z. Lee, O. Zhou, and J. Lu, in edited by C. Hoeschen, D. Kontos, and T.G. Flohr (International Society for Optics and Photonics, 2015), p. 94123J.
- ¹⁶ A.-K. Carton, K. Lindman, C. Ullberg, T. Francke, and A.D.A. Maidment, in edited by J. Hsieh and M.J. Flynn (International Society for Optics and Photonics, 2007), p. 651007.
- ¹⁷ S.J. Glick and C. Didier, in edited by J. Hsieh and M.J. Flynn (International Society for Optics and Photonics, 2007), p. 65102V.

CHAPTER 8: Summary and Future Direction

A second generation stationary digital breast tomosynthesis system was designed, constructed and characterized. The system was made by replacing the conventional thermionic source from the Hologic system with a new linear CNT source array constructed by Xinray Systems. The work completed in this thesis shows the new system has a higher entrance dose rate than the first generation system, which resulted in faster image acquisition times. In addition, the second generation s-DBT system has higher in-plane resolution, and depth resolution than the first generation system, and two commercially available DBT systems. Theoretically, these improvements should improve DBT patient imaging, by providing sharper, higher resolution images. Preliminary studies have also indicated the system is capable of contrast enhanced imaging. However, the clinical effect of this improvement still needs to be determined. Clinical trials need to be conducted to see whether the s-DBT system improvement translates to the clinical setting in breast cancer diagnosis.

This study marks the second step in our efforts towards the development of a stationary digital breast tomosynthesis system. Though there is significant improvement over the first generation, there is still work to be done on bringing this system to market and future development. Although the system has higher resolution and faster image acquisition times than the first generation, further improvement on the CNT x-ray source design will be beneficial to the system. Implementation of a rotating anode would allow for higher powered tubes, resulting in higher tube flux, and potential for reducing focal spot size. Having higher tube flux, and a smaller focal spot size will allow s-DBT systems to further reduce image acquisition times, and

further improve spatial resolution. Improvement in breast cancer screening is always welcomed, as early detection increases the chance of survival.